Experimental Flow Characterization of Anguilliform Swimming Motion

by

Anna Pauline Miranda Michel

B.S. Chemical Engineering
B.S. Biology
Massachusetts Institute of Technology (1998)

Submitted to the Department of Ocean Engineering
in partial fulfillment of the requirements for the degree of

Master of Science

at the

MASSACHUSETTS INSTITUTE OF TECHNOLOGY

June 2002

Author .....
Department of Ocean Engineering
May 30, 2002

Certified by.....
Michael S. Triantafyllou
Professor
Thesis Supervisor

Accepted by .....
Henrik Schmit
Chairman, Department Committee on Graduate Students

Experimental Flow Characterization of Anguilliform Swimming Motion

by

Anna Pauline Miranda Michel

Submitted to the Department of Ocean Engineering
on May 30, 2002, in partial fulfillment of the
requirements for the degree of
Master of Science

Abstract

This thesis aims to elucidate the hydrodynamic mechanisms of flow about anguilliform swimming bodies. This work examines the near boundary flow and the pressure and velocity characteristics of the wake of a model sea snake. Studies on undulatory swimming motion have shown several key results. It has been shown that fish exhibit vorticity control as the undulatory motion of the fish combined with the flapping tail motion creates a jet wake. In addition, previous work has shown that unsteady motions are effective for controlling flow. Two-dimensional waving plate studies have shown turbulence reduction when the phase speed (Cp) increased compared to the freestream speed (Uo).

A 3D flexible snake-like robot was designed and tested in the MIT Marine Hydrodynamics Water Tunnel. Laser Doppler Velocimetry (LDV) and kiel probe pressure sensors were used to study the near body turbulence levels and wake profiles. Near-body turbulence studies at two locations along the length of the snake showed turbulence reduction for $\frac{Cp}{Uo} = 1.2$ when the snake was in the trough position. In the crest position, the snake showed a turbulence maximum at $\frac{Cp}{Uo} = 1.2$. The trough data supports previous 2D studies of waving plates. The crest data however shows opposite results. Wake surveys of pressure and velocity suggest that the snake forces the fluid down at the center and then vortices are generated. The momentum theory was applied to the wake data to estimate thrust. The momentum equation applied to the wake showed different levels of wake development as $\frac{Cp}{Uo}$ increased.

Thesis Supervisor: Michael S. Triantafyllou
Title: Professor

Acknowledgments

There are many people who have helped me throughout this project, in the design stages, the testing, in the processing, and in the writing. First I would like to thank Professor Michael Triantafyllou for giving me the opportunity to become an Ocean Engineer and for providing me with an interesting research project that has challenged me in many ways and has taught me a lot about experimental fluids. I would like to thank him for all of his time, answers, and for all of his support when I found myself struggling. I would like to thank Dr. Franz Hover for the countless hours he spent with me during this project, especially over the summer of experimentation, in helping me with data processing, and most recently with the Lighthill derivation. In addition, many thanks to Dr. Alexandra Techet for helping me to survive the first two years of graduate school. Without Alex, this thesis would not exist and the snake would not have been able to swim. I would like to thank Alex for her help throughout the entire project, for answering all of my questions and emails, and being a great support both when she was at MIT trying to finish her own thesis and when she was away at Princeton. Without the help of Dr. Rich Kimball the snake would not have had any water to swim in and I would have flooded the tunnel more times than I did. I thank Rich for the countless hours he spent with me at the Water Tunnel helping me with everything from how to run the water tunnel to designing the kiel probe experiments to explaining fluid mechanics to me. Rich helped me to fix things when all I could measure was noise and everything seemed to be leaking.

Many UROP students have helped me at different stages of this project. Many thanks to Karl-Magnus McLetchie for being the molding master and for spending so many hours with me trying to mold the snake. Also, thanks go to Karl for co-hosting thesis writing parties with me in the Tow Tank. UROPs Dan Sura and Andrew Deschere were invaluable. I would like to thank them for helping me for so many hours last summer collecting data and designing and building new pieces as they were needed. Thanks to the many other urops who at some point worked on part of this project, Kai McDonald, John Dise III, and Malima Wolf.

Many thanks to Team Tow Tank for their assistance. Joshua Davis has helped me for the many hours especially with Matlab and LaTex, both while he was at the Tow Tank and even after he moved to California. In addition, the snake owes its tail to Joshua. Thanks go to Dave Beal for helping me every time I got confused or frustrated and for answering all of my questions while scootering around the Tank. Thanks to the other Tow Tankers, who have either arrived or left during the past two years, Craig, Muriel, Øyvind I and Øyvind II, Martin, Harald, Vic, Stephen, Lionel, and Justin for making the tank fun.

I would like to thank Dr. Randy Fairman in the water tunnel, who helped me many times when things broke and for climbing on top on the tunnel numerous times to try to fix it for me.

There are several people that were key to the making of the snake. Jose Rosado, Curatorial Associate, at the Harvard University Museum of Comparative Zoology showed me real sea snakes and allowed me to photograph them. Thanks to Mike Tarkanian, 3D printer boy, for 3D printing the snake at Z-Corp and for bringing me samples of the material when my molding failed. Fred Coté at the Edgerton Student Machine Shop, taught me how to machine and helped me every time I needed to make something. His great ideas saved me so much time.

In addition, I would like to thank Dominique Jeudy, the members of OE Headquarters, and Kathy de Zegotitia for all the administrative help.

I would also like to thank the girls of OE: Katy Croff, for being the evil princess and Katarzyna Niewiadomska, for letting me complain to her when I needed to. Also thanks to the SK girls for understanding when I had to hide in the basement.

Lastly, I would like to thank my family for supporting my decision to take the longer road to graduate school and for all of their support in my academic pursuits and Masaya for understanding why I wanted to go back to school and for trying to understand why I chose to go back to MIT instead of to a fun school.

I would like to acknowledge the National Defense Science and Engineering Graduate Fellowship and the Link Fellowship for Ocean Engineering and Instrumentation for providing me with the funds to be a graduate student.

Contents

List of Figures

List of Tables

Chapter 1

Introduction

This thesis examines the hydrodynamic characteristics of a biomimetically designed swimming sea snake in a recirculating water tunnel. A snake robot was developed to mimic anguilliform swimming motions. This work centers about two main goals: 1) to elucidate the underlying hydrodynamic mechanisms of flow about swimming bodies similar to sea-snakes, and 2) to gain a better understanding of the anguilliform mode of propulsion and how it can be used in biomimetic underwater vehicle design.

1.1 Biomimetic Design

The field of biomimetics applies ideas from nature to solve engineering problems with the belief that plants and animals have evolved optimal solutions for survival. In this study, biomimetics is used in the area of robotics to study the undulatory motion of a swimming sea snake. Specific characteristics of the sea snake's body shape and swimming motion have been replicated in the model snake. Natural selection has enabled fish and other aquatic swimmers to evolve to be highly efficient, though not necessarily optimal swimmers. Inspiration from fish can be applied to the field of robotics to improve underwater vehicle design. One example of an application is in the development of AUVs, autonomous underwater vehicles. As the use of AUVs increases, longer mission duration and efficiency will be required. Applying an efficient swimming motion that mimics fish swimming could produce improved

propulsion over that of a traditional thruster, propeller system. In addition, fish techniques could be used to improve the hovering and maneuvering capabilities of AUVs. Noiseless propulsion and a less prominent wake inspired by fish would have applications that would benefit military ocean vehicles [14].

Biomimetics has a rich history including inventors such as the Wright Brothers who mimicked the structure of a wing in their plane. Recently, robotic fish such as the MIT Robotuna and RoboPike have further explored the biology of aquatic creatures in order to better design underwater vehicles. An understanding of both the muscle structure and the swimming patterns of these creatures is needed to design such vehicles. This study focuses on the hydrodynamic mechanisms that result from the mode of swimming used by sea snakes and eels. This anguilliform motion varies from the motion of such fish as tuna and pike and therefore this study provides insight into a different swimming motion.

1.2 Characteristics of Sea Snakes

Sea snakes are air breathing reptiles unlike eels with gills and are found in the Indian and Pacific oceanic regions. Some species of sea snakes are great divers and are able to dive to depths of 100 m and some can remain underwater for up to 30 minutes. The snakes are able to accomplish this by using air in their lungs for buoyancy. Sea snakes are highly venomous; therefore, few studies have been done on sea snakes and especially on their swimming behaviors [9].

Sea snakes have adapted to marine conditions and their body has evolved a form to survive the ocean. The body of a sea snake is laterally compressed, starting out cylindrical and flattening towards the tail. Sea snakes possess a strong flattened paddle-like tail which is believed to enhance propulsive thrust. The tail is thought to be the primary source of thrust. The tail is flat and wide up to its tip while the tail of a land snake is rounded and tapered toward the tip making the propulsive force generated by the sea snake larger than that of a land snake. The same difference is seen between the tails of land and marine iguanas [3, 6, 8, 9].

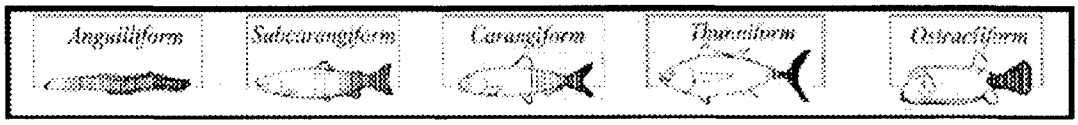

Figure 1-1: An illustration of the subdivision of BCF (body and caudal fin) type swimming motion. Snakes and eels use anguilliform swimming, the most undulatory type of motion. The amount of undulatory motion used in swimming decreases from right to left while the use of a propulsive structure pivoting at a point increases from left to right [14].

1.3 Fish Swimming

Fish swim with a variety of different swimming motions. One way to classify fish swimming divides them into fish that move their body and or caudal fin (BCF) and those that use appendages, median and/or a paired fin (MCF). The BCF fish can be further subdivided into anguiliform, subcarangiform, carangiform, thunniform, and ostraciform swimmers as shown in figure 1-1 [14]. These fish vary from highly undulatory (anguilliform) to highly oscillatory (ostraciform). Undulatory motion is defined as motion where a wave passes along the propulsive structure. In ostraciform swimming, the propulsive structure does not exhibit a wave formation and instead pivots at a point. Undulatory BCF swimming uses a propulsive wave that travels in the direction opposite to the direction of movement of the fish. The wave travels at a speed greater than the swimming speed [14].

When fish swim, there is an transfer of momentum between the fish and the water through drag, lift, and acceleration reactive forces. A fish propelling itself at constant speed demonstrates momentum conservation. The thrust of the fish on the water equals the resistance of the water on the fish. This is referred to as self-propulsion. Drag can be subdivided into friction drag, form drag, and induced drag. Friction drag is caused by the skin friction between the fish and the boundary layer of the water. This is due to the viscosity of water in areas of large velocity gradients. Form drag results from pressures that arise when water is pushed out of the way during swimming. This is shape dependent. Streamlined bodies function to reduce form drag. Induced drag results from energy lost in vortices formed by the caudal and

pectoral fins as they generate lift or thrust. The induced drag is dependent on the fin shape [14]. Through the study of fish shapes and swimming motions, ways to reduce these types of drag will emerge. As a result, lower drag underwater vehicles will be developed.

1.4 Anguilliform Swimming Motion

Anguilliform swimming has evolved separately in many vertebrate taxa and therefore it is widespread and found in ecologically and morphologically diverse fish, amphibians, and reptiles [7]. Sea snakes swim with this undulatory mode of propulsion. Anguilliform locomotion is also used by eels, lampreys, loaches, and gobies. This type of swimming, also referred to as snaking, is used by the young of many fish. Waves of shorter length than the body of the animal are propagated posteriorly along the length of the animal, causing the animal to move forward. The whole body participates in these large amplitude undulations. At least one complete wavelength is present along the body. The wave has an increasing amplitude as it passes from the head to the tail. This mode of swimming has been shown to be used over a range of velocities. Snakes are also capable of backwards swimming by altering the direction of wave propagation. Most previous work has focused on other types of fish swimming and not on anguilliform swimming; thus, little is known about this mode of propulsion [3, 14].

The main differences between anguilliform and carangiform swimming motions are the existence of a pivot point and the number of complete sine waves present on the body. A pivot point is not present on an anguilliform animal. In anguilliform swimmers, there is an increase in amplitude of the lateral movement from head to tail. Studies on eels have been completed to understand the kinematics of their swimming. Table 1.1 shows the results of such work [20]. This data shows that the eel swims with a $\frac{Cp}{U}$ ratio of 1.43. Kinematic data was also taken for a sea snake and is shown in table 1.2. The sea snake shows a $\frac{Cp}{Uo}$ value of 1.37.

The ratio of $\frac{Cp}{U}$ relates the overall fish swimming speed to the wave propaga-

Table 1.1: Results of a kinematic characteristic analysis of eel swimming [20]

Variable	Unit	Symbol	Value
Period	s	T	0.14
Speed	m/s	u	0.28
Relative Speed	L/s	U	2
Relative Wave Speed	L/s	Cp	2.86
$\frac{Cp}{U}$			1.43

Table 1.2: Results of a kinematic characteristic analysis of snake swimming [3]

Variable	Unit	Symbol	Value
Length	m	L	0.51
Wavelength	L	lambda	0.257
Number of wavelengths		L/lambda	1.7
Speed	m/s	U	0.32
Wavespeed	m/s	C	0.44
$\frac{Cp}{U}$			1.37

tion speed and is an indication of swimming efficiency [14]. A numerical study on sea snakes showed that mean thrust decreased as $\frac{Cp}{U}$ decreased and that the mean power first decreased as the speed ratio increased and then increased again at a high speed ratio. For anguilliform swimmers, the net velocity of the fish U is usually about 0.6*Cp which gives $\frac{Cp}{U}$ =1.67 [11]. The ratio of $\frac{Cp}{U}$ has been found to vary with swimming speed for some anguilliform swimmers. For sea snakes, the wave speed tends to increase along the length of the body and may be due to the muscle activation increasing along the body of the snake [7]. $\frac{Cp}{U}$ is a measure of the propulsive effectiveness of the propagating waves. Undulatory fish move through the water and affect the water that is at right angles to the direction of motion. This causes that water to move laterally which can form a vortex wake behind the trailing edge. Therefore, part of the fish's energy is wasted on the creation of a vortex wake. The rest of the fish's energy output is available for propulsion, producing movement at a velocity Uo, against the viscous resistance of the water [11]. For efficient swimming, the amount of energy spent on the vortex production should be small.

Lateral compression towards the trailing edge is often present in undulatory swimmers. The lateral compression improves propulsive efficiency as it decreases the mass of water next to the body that must be accelerated for propulsion. The forces needed for this water acceleration decrease and so hydromechanical efficiency increases. The inertial force and the drag force related to the body undulations can be used to generate propulsive forces. By increasing the height of the tail, the inertial force is increased by the added mass in proportion to the square of the height. In large elongate animals the Reynolds number is large enough to change the inertial effects of the fluid into hydrodynamic forces and moments [3].

1.5 Unsteady Motion of Fish Swimming

Fish swimming is a demonstration of unsteady flow control. Fish swim primarily by propagating a travelling wave along their backbone. This has been modelled in previous biomimetic work such as the RoboTuna. In the RoboTuna, the undulatory motion is predominant only in the aft half of the body which is characteristic of thunniform swimming. In addition, fish illustrate vorticity control. The undulatory motion of the fish combined with the flapping tail motion creates a jet wake which allows them to propel themselves [19]. This was demonstrated by Triantafyllou and Triantafyllou who showed with the RoboTuna that a caudal fin could create a jet wake as seen in figure 1-2.

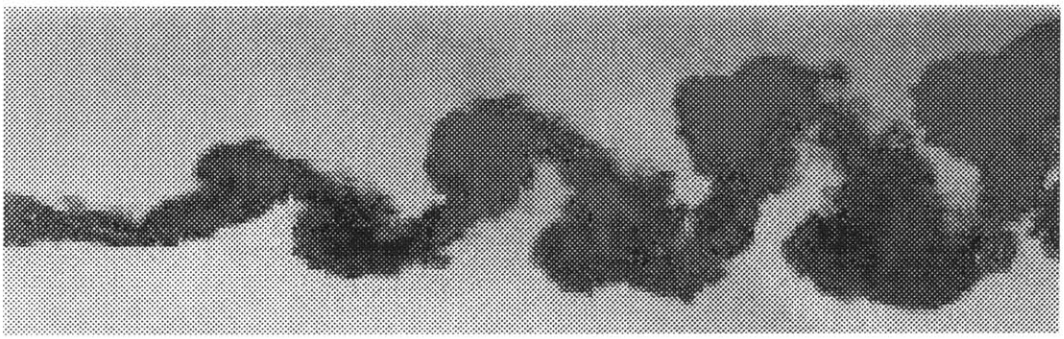

Figure 1-2: Dye visualization showing the jet wake of the RoboTuna. The jet wake produces a reverse Kármán street as seen in this photograph [19].

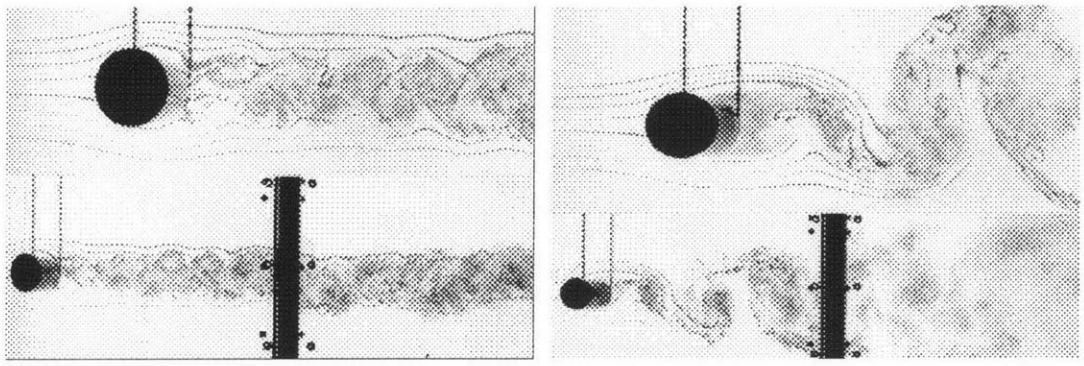

(a) (b)

Figure 1-3: Dye visualization of the flow past a stationary cylinder and an oscillating cylinder. (a) shows a stationary, non-oscillating cylinder (b) shows an oscillating cylinder at $S_f = 1$ and $\Omega = 3$. [18]

Unsteady motion of a body can be beneficial for efficient flow control. Vorticity in the wake of a self-propelled body demonstrates that a propulsive jet is needed to counter the drag of the body. Manipulation of the wake has been shown to increase propulsive efficiencies. High propulsive efficiency has been associated with a downstream wake of two to four vortices per period arranged in a reverse Kármán street [13]. Gray found that an eel produced a reverse Kármán street in the wake [3].

Tokumaru and Dimotakis investigated oscillation control by a rotating cylinder. These cylinders were forced to have rotary oscillations in steady flow. Dye visualization results of these studies are shown in figure 1-3 [18]. Figure 1-3(a) shows the unforced case where the dye disperses and mixes over a large area. Figure 1-3(b), the rotating case, shows a wake of about the same size as the dye field in front of the cylinder. This suggests that control over a cylinder wake can be achieved by controlling the rotating motion. The addition of circulation into the flow may allow control of the wake dynamics. In the case of the rotary cylinder, the forcing reduces pressure (wake) drag. Therefore, adding circulation into the flow may allow control of wake dynamics. Figure 1-3(a) shows a typical Kármán vortex street and figure 1-3(b) shows the reduced wave signature and drag on the body. Figure 1-3(b) illustrates

how forced oscillations, an example of unsteady flow control, can result in significant drag reduction [18].

1.6 Flow About two-dimensional Waving Plates

Fish swimming can be simplified to a traveling wave as shown in figure 1-4. The components of a wave include the amplitude (A), the wavelength (λ), the phase speed of the wave (Cp), and the velocity of the flow (Uo). The quantity $\frac{Cp}{Uo}$ is the wave phase speed nondimensionalized with the free speed and is an important parameter used in wave studies and will be used throughout this work.

Several experiments have shown the unique effects of a waving boundary. In 1974, Taneda, with a waving plate experiment, showed that when the wave phase speed was greater than the freestream speed, no separation off the crest of the wave occurred as shown in figure 1-5(a). Flow over waving boundaries was shown to separate if the traveling wave speed was slower than the freestream fluid velocity as shown in figure 1-5(b). This was seen for both the crest and the trough position of the wave. However, when the phase speed exceeded the freestream velocity, the flow remained attached and did not separate at the crest or trough regions [16]. When flow separates form drag (pressure drag) is increased, thus when the phase speed exceeds the freestream speed and no separation occurs, is ideal for decreasing drag on a swimming body.

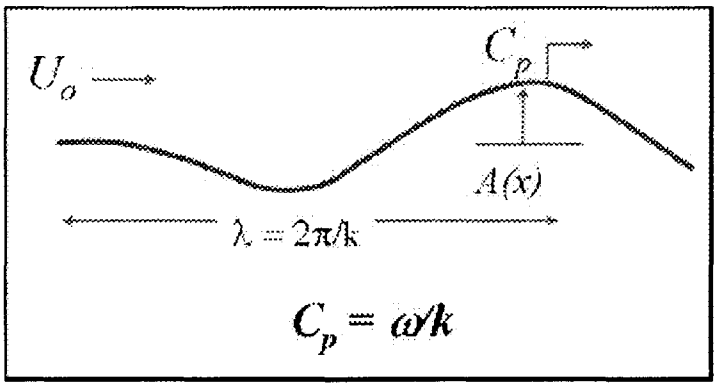

Figure 1-4: Drawing showing the components of a traveling wave. The freestream is Uo, the amplitude is A, and the phase speed is Cp.

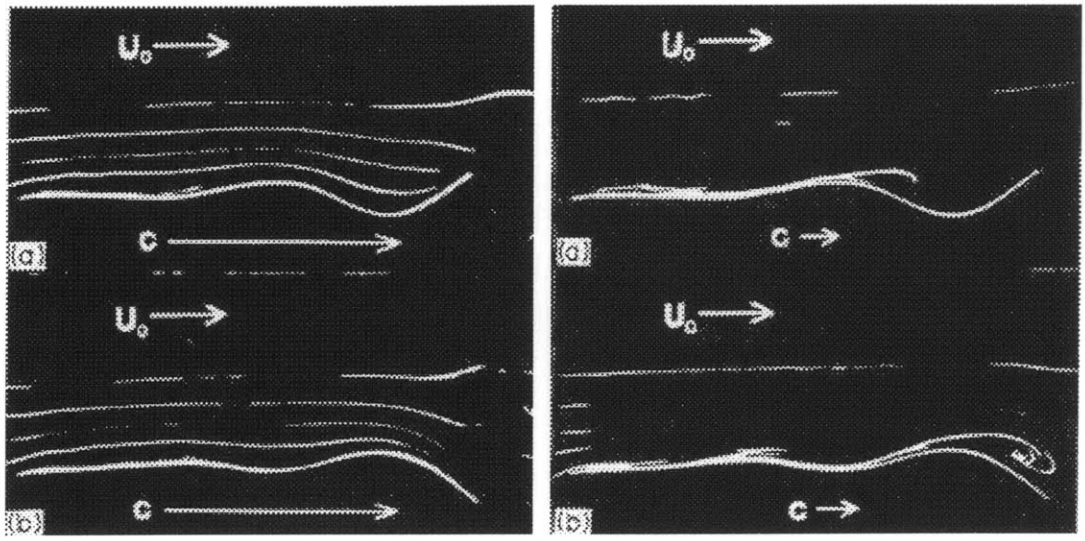

(a) (b)

Figure 1-5: Images of the streaklines from Taneda's flow over a waving plate experiment. (a) shows streaklines when Uo>Cp and (b) shows streaklines when Uo<Cp. [16]

Zhang completed numerical simulations of a waving boundary and showed a reduction in turbulence intensity when the phase speed exceeded the freestream speed illustrating another important benefit of a wavy swimming body [22]. Zhang found that when $\frac{Cp}{Uo}$ reached 1.2, turbulence energy was suppressed. Figure 1-6 shows the results of Zhang's work. The light areas close to the wave boundary are areas of low turbulence intensity. The darker areas represent higher turbulence intensity. The $\frac{Cp}{Uo}$ = 1.2 case shows a significantly greater area of low turbulence intensity. A decrease in turbulence intensity reduces frictional drag. As a result, identifying a phase speed with reduced turbulence intensity would be ideal for designing low drag vehicles.

Similar to Zhang, Techet studied near body turbulence intensity on a waving mat in the MIT Marine Hydrodynamics Water Tunnel. Techet's work was the precursor to the snake project described in this thesis. This work focused on a two-dimensional mat that spanned the entire tunnel test section, and thus it was impossible to obtain wake data. As seen in figure 1-7, this experimental work showed that turbulence

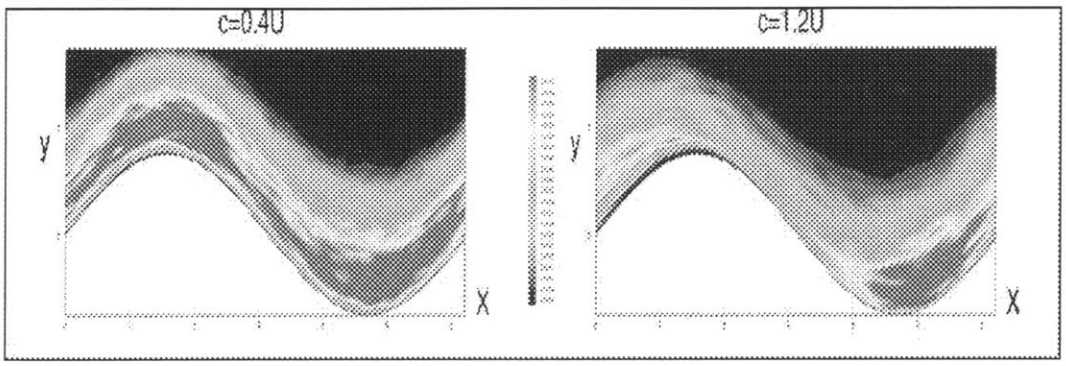

Figure 1-6: Numerical simulation of waving boundary turbulence intensity by Zhang. The figure on the left shows $\frac{Cp}{Uo} = 0.4$ and the figure on the right shows $\frac{Cp}{Uo} = 1.2$. The light areas above the wavy boundary represent lower turbulence intensity and the darker areas represent higher turbulence intensity. The $\frac{Cp}{Uo} = 1.2$ case shows lower turbulence intensity than the $\frac{Cp}{Uo} = 0.4$ case. [22]

intensity was reduced for phase speeds up to 1.2 times the freestream velocity up to a Reynolds number of one million [17]. The Techet data was taken at a distance of 4 mm from the boundary under piston rod five (diagram of location of pistons is shown later in figure 2-8). The data was taken at Uo=1.0 m/s with $\frac{Cp}{Uo}$ values ranging from 0.3-2.0 [17]. A minimum in turbulence intensity occurs for the trough (upper data points) and crest positions (lower data points) of the mat at a $\frac{Cp}{Uo} = 1.2$.

The above described projects all focus on 2D bodies. In this thesis, experiments were performed to determine whether turbulence intensity is decreased for a 3D revolved swimming body and to examine its wake profiles.

A three-dimensional waving plate study was carried out by Cheng et al which showed that undulatory motion can reduce three-dimensional effects. Cheng found through modeling that when the wave amplitude is constant or increases slightly and the wavelength is close to the body length, that the swimming performance was best and that the flow was quasi-two-dimensional. This means that the cross-sectional flow is about equal to a two-dimensional flow. Cheng found that forward thrust could be generated by the undulatory motion of a three-dimensional plate with constant or increasing amplitude. The propulsive efficiency was lower for waves progressing from tail to head than for those going head to tail. Thrust was only produced when the

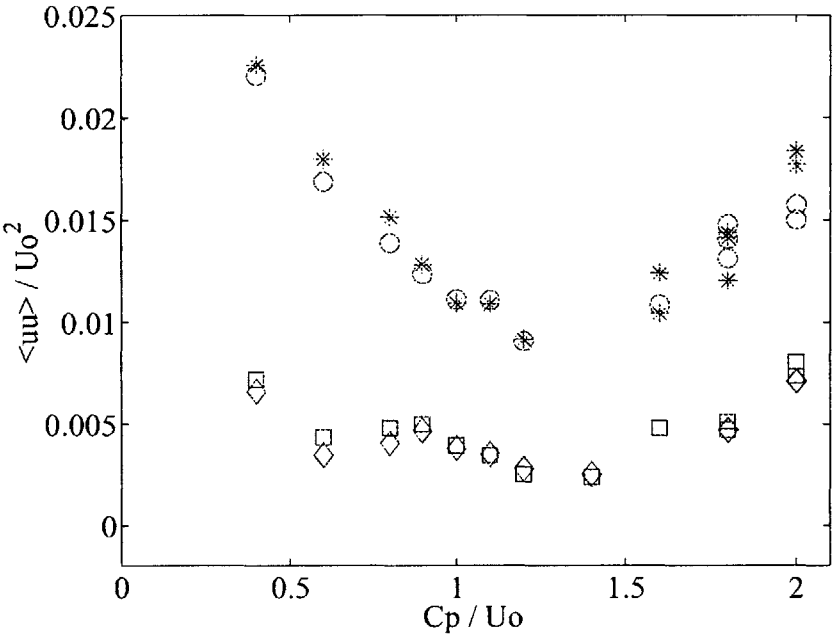

Figure 1-7: Turbulence intensity (u'u') results for a 2D waving plate experiment by Techet. (u'u') is denoted in this figure by $< uu >$. The upper data set is the data taken in the trough of the waving mat and the lower data set is the data taken in the crest. A turbulence intensity minimum occurs at $\frac{Cp}{Uo}$=1.2 for both the crest and trough positions. [17]

wave velocity was greater than the swimming velocity for swimming motion that had an increasing amplitude wave. The thrust and power was shown to increase as the wavenumber decreased [5].

1.7 Thesis Overview

This thesis extends the work of waving bodies through the study of a biomimetically designed sea snake. The design process, a main focus of the project, is discussed in detail as well as the experiments and results. Near body turbulence is examined. Velocity and pressure measurements are presented in the snake's wake and used to calculate the thrust produced by the snake through a momentum balance. Laser Doppler Velocimetry, (LDV), and kiel probes are two techniques discussed within their respective chapters. The culmination of these experiments is discussed in chapter 6.

Chapter 2

Design Process and Experimental Set-up

Biomimetic design was used in the development of the swimming snake robot. By first studying a real sea snake, the features of the snake that aid in propulsion were incorporated into the design of the model snake. The snake robot was designed and molded to use a crank-shaft mechanism that drives an external wave down the model. This mechanism was originally used for Techet's 2D waving plate experiments [17]. The snake was developed for tests in the MIT water tunnel. This chapter details the steps necessary to design and build the model snake.

2.1 Design Process

2.1.1 Overview

The building of the biomimetic model sea snake underwent a series of steps. First, a real sea snake was examined and photographed to understand its biological characteristics and adaptations for swimming. Next, an engineering design of a prototype snake was made with 3D CAD software. The CAD design was then 3D printed in sections and the rigid prototype snake was assembled from these parts. This was followed by a two part molding of the actual experimental snake. RTV silicone was

used to create a negative mold and then a flexible polyurethane material was used for the final snake.

2.1.2 Examination of a Real Sea Snake

The initial stage in the design of the sea snake was the observation of a real sea snake of the species, *Astrotia stokesii*, at the Harvard University Museum of Comparative Zoology (figure 2-1). These observations allowed for the visual understanding of key characteristics of sea snakes including lateral compression and a flattened tail. The tail is shown in figure 2-2. As described in section 1.2, the lateral compression occurs in many anguilliform swimming animals as it increases propulsive efficiency. The flattened tail aids in propulsion by providing a larger surface area. These important characteristics were incorporated into the design of the model. The lateral compression and flattened tail were exaggerated in the design to ensure that these prominent characteristics that are important for the snake's swimming were well tested.

2.1.3 Three-Dimensional Model Design Process

A 3D model was made of the snake using Solidworks CAD software as shown in figure 2-3. The model was composed of a head, a tail, and four body pieces. Figure 2-3 shows an assembly of these pieces that form the final snake mold. The six pieces fit together to form the final one meter long snake. The head begins with a very rounded nose and then tapers to a constant elliptical diameter. The two snake parts aft of the head continue to display a constant elliptical cross-section. The fourth and fifth pieces gradually taper down towards the tail where piece five joins the flat paddle-like tail. The snake maintains a cross-section of 12.5 cm x 5 cm along the area with a constant cross-section. The tail then increases slightly in width but decreases in thickness. The tail of a sea snake is rounded unlike that of a land snake, and this feature is present in the design. The tail is 23 cm long by 14 cm wide. The tail contains a central rib-like piece. Real snakes contain strong muscle in their tails to aid in the thrusting motion of the tail which is mimicked by this rib. In addition,

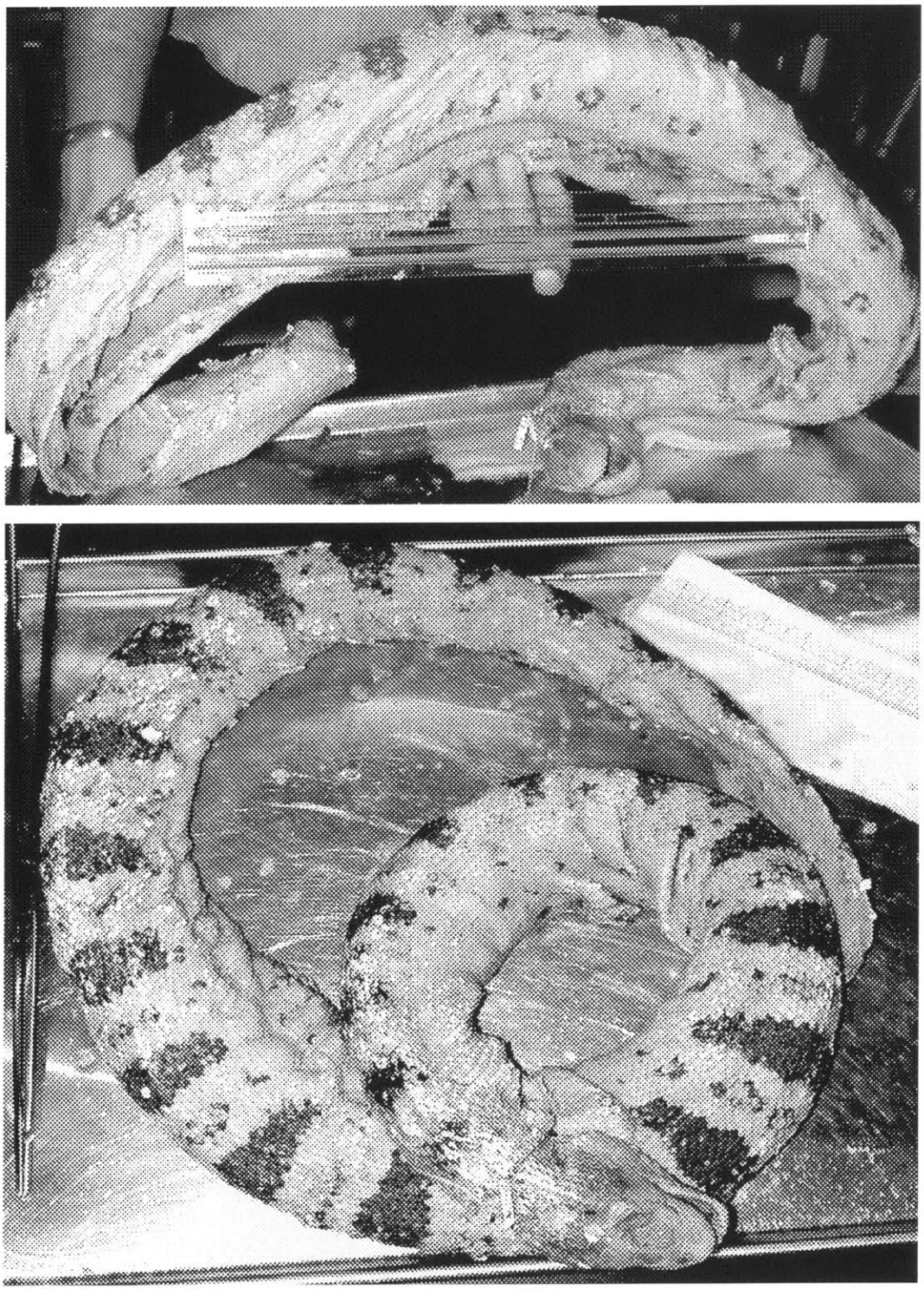

Figure 2-1: Photographs of the sea snake *Astrotia stokesii*. These photographs were taken at the Harvard University Museum of Comparative Zoology. The paddle tail can be seen in both images.

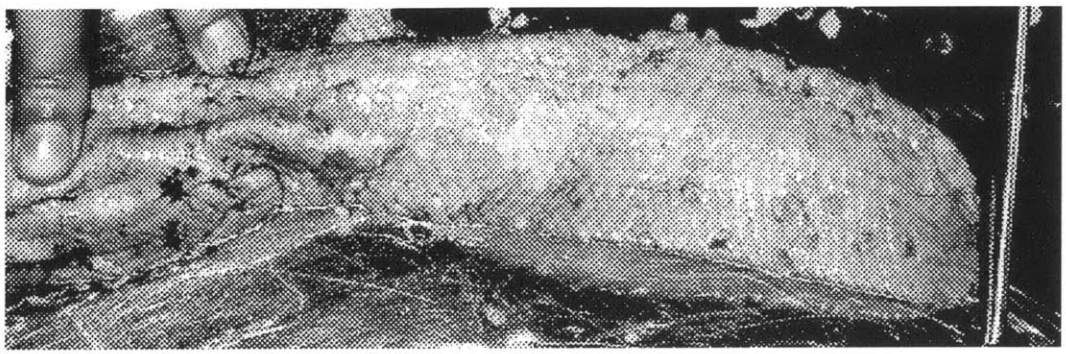

Figure 2-2: Photograph of the paddle-like tail of the sea snake *Astrotia stokesii*. This photograph was taken at the Harvard University Museum of Comparative Zoology.

since the tail is only 2.5 cm thick, the rib-like piece provides a point where a piston rod could be attached. This rib enables the snake tail to move in a constant thrusting motion without having the tail flop. The snake design described therefore contains many biomimetic characteristics.

The individual parts that comprise the snake model were 3D printed from the Solidworks drawings (figure 2-4). The 3D snake parts were printed with a starch/cellulose material, ZP14, and infiltrated with cyanoacrylate. The 3D printed parts were designed to fit together to form a single solid model. The snake model was printed with two holes on each cross-sectional, flattened side of the piece. Dowel pins fit in these holes allowing two parts to be connected. In addition, to secure the pieces together to create a solid snake, superglue was applied to the ends of the snake pieces that were connected. Once the snake pieces were permanently connected, holes were drilled on the top of the 3D pieces and pins were glued into the holes. These pins act as place holders for inserts to be molded into the negative mold. These inserts were later attached to the piston rods that drive the snake motion.

Three holes were drilled into the head for the front foil piece that attaches the snake head to the tunnel. Small pegs were glued into each of these holes.

It studying the near-body turbulence of the snake, it was important to provide a smooth snake body surface. This smooth surface will increase the accuracy of the turbulent studies. In order to reduce the effect of a non-smooth surface, Bondo car body filler was used to remove the unevenness at the joints of the 3D printed snake.

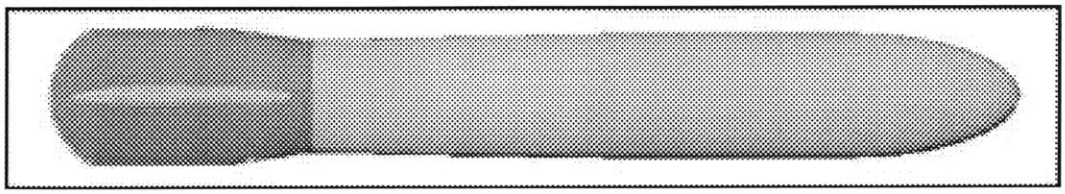

Figure 2-3: Solidworks CAD drawing of the assembled sea snake model. Six pieces fit together to form the final snake model used for casting the snake in a two step casting process.

Bondo was also used to smooth out any uneven sections. The entire snake was then sanded to create an even surface across the entire snake.

2.1.4 Molding Process for Casting the Snake

A delrin molding box was built for casting the 3D model. The box was built with holes on the top for pouring the molding material around the entire snake. The 3D printed model was cast with RTV Silicone (RTV 664 GE Plastics) to make a "negative" mold. Although the 3D printed snake had been infiltrated with cyanoacrylate, the material remained somewhat porous. In order to prevent the RTV silicone from being absorbed into the snake, it was recommended by the 3D printing company to coat the snake with paint primer and to wax the snake. The snake was primed with Brite Touch General Purpose Primer three times, sanded, and then re-primed. In addition, the snake was coated with Carnauba paste wax (West Marine) and Smooth-on Universal Mold Release was sprayed on the snake. The snake was then attached to the top of the casting box with the pegs described in section 2.1.3. This allowed the snake to be suspended in the box. Therefore, a mold could be made in two parts, one from the bottom of the box to the centerline of the side of the snake and one from the centerline to the top of the box.

The RTV mixture was made by mixing its two silicone components, stirring until the silicone was a consistent blue color, and then vacuuming until the majority of the bubbles were removed. The RTV was then poured into the box until it reached the centerline of the snake. The RTV mold was left overnight to cure. After 12 hours, it was found that the RTV had not cured against the snake and the snake had to be

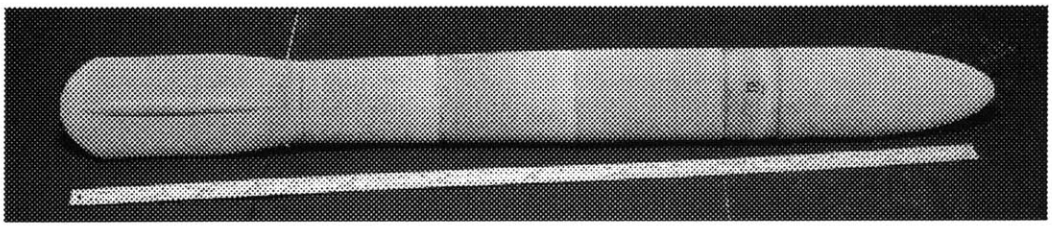

Figure 2-4: Photograph of the 3D printed assembled snake model. The six different sections that have been connected are evident.

removed from the molding box. As a result the wet RTV had to be cleaned from the snake.

In order to determine what was an acceptable coating material to use, a series of tests were completed with different materials and samples of the 3D printed material. Each of the 3D samples was coated in a material and then placed in a plastic beaker. RTV was poured around half of the sample and the samples were left overnight. The results are shown in table 2.1.

Table 2.1: Results of the RTV curing experiment

Material Tests	RTV Result
Wax	Uncured
Brite Touch General Purpose Primer	Uncured
Carnauba Paste Wax	Uncured
Brite Touch General Purpose Primer and Carnauba Paste Wax	Uncured
Smooth-on Universal Mold Release	Cured
Flex Primer and Wax	Uncured
Bondo Car Body Filler	Uncured
Rustoleum	Uncured
Flex Primer	Uncured
Epoxy	Cured

The epoxy showed positive results. Since the snake's joints had Bondo on them, an additional test was conducted to see if epoxy would cure over Bondo. A 3D printed piece was coated in Bondo and left to cure. This was followed by a coat of epoxy which was then left to cure. The result showed that the epoxy cured over the Bondo.

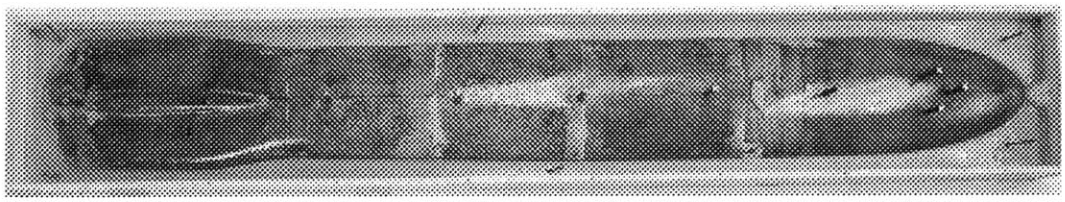

Figure 2-5: Photograph of the 3D printed snake during the molding process. This image was taken after the bottom half of the snake had been cast in RTV silicone. The RTV silicone is the material seen surrounding the snake. The snake is shown in the box made for the casting.

Therefore, an acceptable process was developed for the RTV molding and the snake underwent a series of steps to prepare it for molding:

- Sanded
- Coated in epoxy
- Sanded
- Coated in epoxy
- Wet sanded with 600 grit sandpaper

The snake was recast in RTV in the two step pouring process previously described. After the RTV mold was completed, the solid 3D printed snake was removed from the box. Figure 2-5 shows the snake in the box, after the top half of the mold has been removed.

The RTV negative mold was sprayed with Smooth-on Universal Mold Release. The negative mold was filled with Evergreen 10 Smooth-on liquid urethane rubber to form the final snake. Evergreen 10 is a very soft urethane material with durometer 10. The urethane is low in viscosity which allows it to cure with negligible shrinkage [2]. The characteristics of this material are shown in table 2.2.

At the locations where the piston rods attach to the snake, it was necessary to mold T-shaped connectors into the snake. These are later used to connect the snake to the crankshaft mechanism that drives the traveling wave down the snake. An initial test on their ability to hold in the Smooth-on was completed by casting them

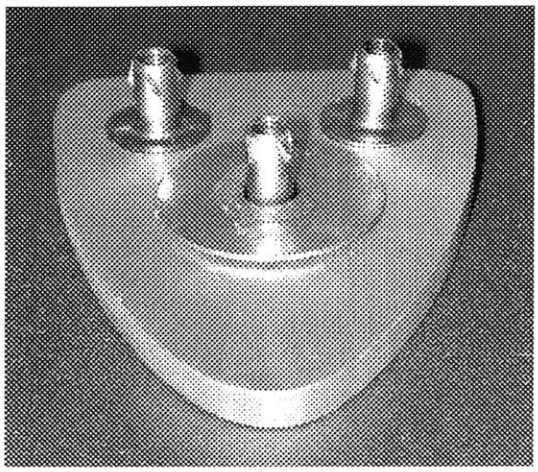

Figure 2-6: Photograph of the metal plate that was molded into the snake head. The T connectors are shown. One of the T connectors is shown modified with a washer to help the head piece to remain in the snake.

into the material. It was found that the Smooth-on material was too flexible to keep the T-connectors from pulling out when flexed. Therefore, large washers were glued onto the T-connectors to create a larger surface area for embedding in the Smooth-on. A test of the washer plus T-connector ensemble found that they were capable of resisting pulling out of the Smooth-on when flexed. The seven T-shaped connectors plus washer ensembles were molded into the snake for attachment to the driving piston rod apparatus. In addition, a metal plate was molded into the head to add both stiffness and to minimize the pitching of the head during the swimming motion (figure 2-6). The tail does not contain any internal stiffening.

To cast the snake, the Smooth-on Evergreen 10 liquid polyurethane was mixed with black dye. The polyurethane was poured into the casting box at the tip of the

Table 2.2: Material characteristics of Smooth-on Evergreen 10 urethane [2]

Shore A Hardness (durometer)	Color	Specific Volume	Specific Gravity	Mixed Viscosity (cps)	Tear Strength (pli)	Weight $\frac{in^3}{lb}$	Elongation at break
10	Off White	274	1.01	600	20	27.8	600%

nose position. It was slowly poured through a funnel into the snake mold to minimize bubbles and was allowed to overfill the mold by about 0.5". The snake was then left to cure overnight. The Smooth-on material cures in approximately 16 hours, though it cannot be poured after approximately 30 minutes.

2.2 Experimental Set-up

2.2.1 MIT Marine Hydrodynamics Water Tunnel

The snake was installed in the MIT Marine Hydrodynamics Water Tunnel as shown in figure 2-7 with the direction of the inflow represented by the arrow. The water tunnel is a 6,000 gallon recirculating water tank that spans two floors. An impeller is used to drive the flow. The flow speed is controlled on the upper floor where the test section is located. The water tunnel is capable of running at speeds of up to 10 m/s. In figure 2-7, the test section is located in the upper right. The test section is 1.5 m long and has a cross section of 0.5 m x 0.5 m. Each polycarbonate window of the test section is removable to allow for special test windows to be used. During these experiments, a laser quality window with minimal scratches and highly parallel faces was used for the Laser Doppler Velocimetry tests. A window was modified for the pressure measurements to hold the kiel probes as will be discussed in chapter 4. For the snake experimentation, the top window was replaced with the wave driving mechanism.

Figure 2-8 shows a photograph of the experimental set-up with the snake connected to the wave driving mechanism. The snake is located inside of the tunnel, connected to piston rods that drive the wave. The inflow velocity, U_o, is identified. The photograph identifies pistons five and six where the near-body turbulence studies were carried it. The two extrema of the snake, the trough and crest positions, are identified in figure 2-8. For the data taken at a piston, when the snake is at its top-dead center location the snake at this point is in a "trough" configuration as viewed from the laser used in the LDV experiments which is located below the snake.

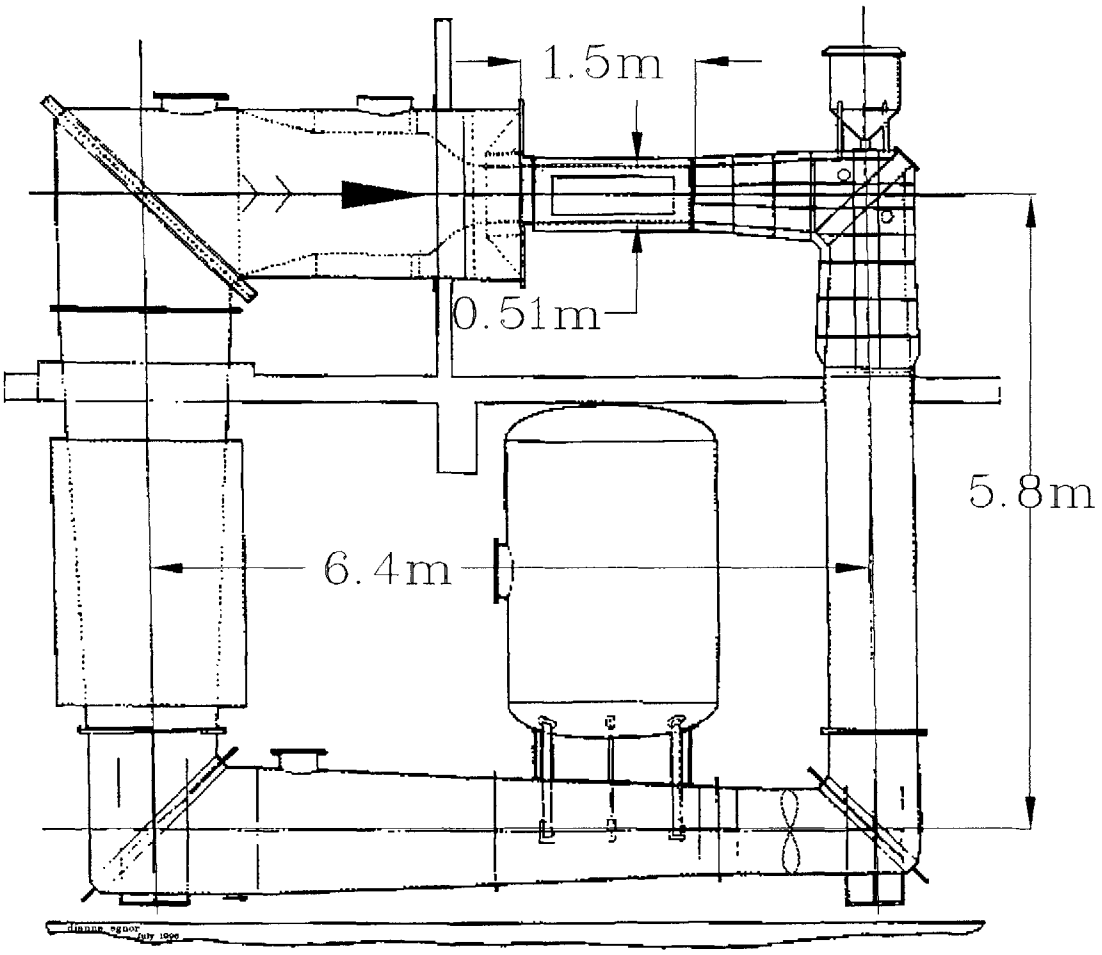

Figure 2-7: Schematic drawing of the MIT Marine Hydrodynamics Water Tunnel. The inflow direction is shown by the arrow. The test section is shown in the upper right and is indicated by its dimensions, 1.5 m long and 0.5 m x 0.5 m in cross-section. The water tunnel was the facility used for all testing.

When the piston is at bottom-dead center, the snake is considered to be in a "crest" configuration. The trough and crest positions are 180° out of phase of each other.

The coordinate system shown in figure 2-8 is used throughout the experimentation and this thesis. The X direction is the direction of the incoming flow. The Z direction is represented by the up and down coordinate in the test section. The Y direction is the coordinate in and out of the test section. The zero point (0,0,0) is at the tip of the tail when the snake's tail is at its mean position.

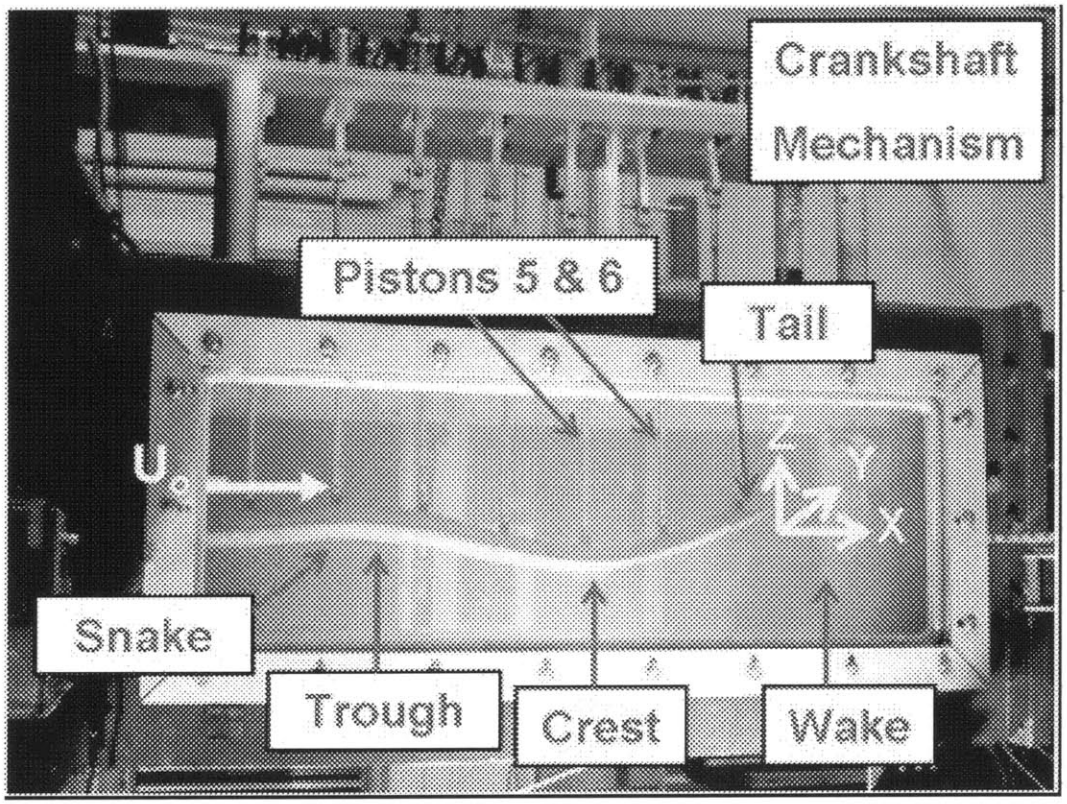

Figure 2-8: Photograph of the sea snake model installed in the MIT Water Tunnel. The inflow velocity is indicated. The snake is shown attached to the crank-shaft mechanism which drives the waves down the snake. Piston rods connect the snake and the crank-shaft mechanism. Pistons five and six are the locations where the near-body turbulence studies were completed. The tail and wake area are identified. The snake is shown in the two extrema positions, the trough and crest positions. The trough is when the snake is at its highest point and the crest is when the snake is at its lowest point.

2.2.2 Crank-Shaft Mechanism Used to Drive an External Wave

The snake was actuated by an external crank-shaft mechanism shown in figure 2-9 that was used successfully for Techet's 2D waving plate experiment. The design of the system is detailed by Techet [17]. Seven piston rods connect the snake to the crank shaft mechanism which drives an external wave along the snake. The pistons actuate the snake in the transverse direction and are located 13 cm apart from each other along the centerline of the snake body. The tail extends slightly aft of piston seven. Near sinusoidal motions of each piston location are created by cranks with varying phase angles which are mounted on a single drive shaft. Figure 2-10 shows a CAD drawing of the sea snake attached to the crank-shaft mechanism.

The crank-shaft mechanism was set up to allow the amplitude of the snake to increase linearly as the distance from the head of the snakes increased. The amplitude increased by the ratio x/16 where x is the distance in inches of the snake from the head. The nose of the snake was held fixed through a foil mounted to the top of the tunnel which attached to the internally molded metal plate.

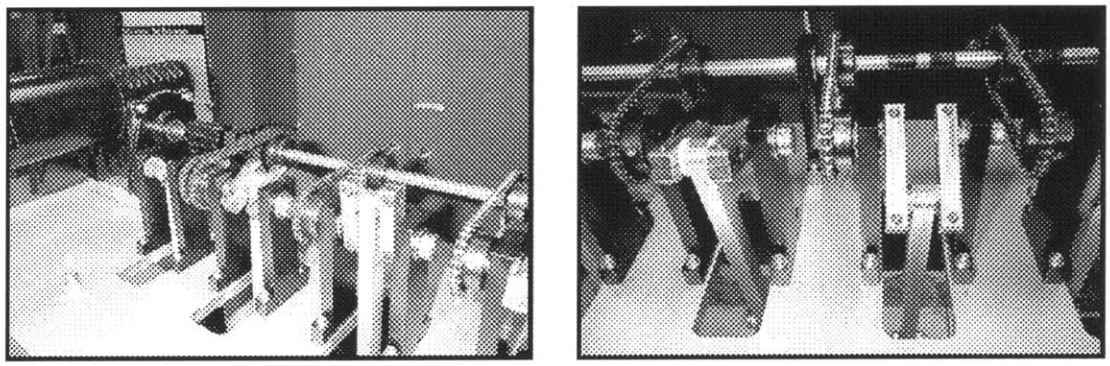

(a) (b)

Figure 2-9: Photographs of the crank-shaft mechanism. This mechanism drives the piston rods in an up and down motion which allows a traveling wave to be sent down the snake.

2.2.3 Snake Motion Parameters

The snake undergoes a traveling sinusoidal wave shape with a linearly-increasing amplitude which is characteristic of a real snake. The snake's motion is described by equation 2.1 with the parameters shown in table 2.3.

$$y(t,x) = A\frac{x}{L}sin(kx - \omega t) \tag{2.1}$$

Table 2.3: Snake motion parameters

y	lateral motion of the snake centerline
t	time
x	longitudinal coordinate of the snake, measured positive aft of the nose
A	amplitude of motion at the tail
L	length of the robot, 1m
ω	piston frequency (rad/s)
λ	wavelength of undulation
Cp	phase/wave speed

C_p is the phase speed and can be defined as:

$$C_p = \frac{\omega}{k} = f\lambda \tag{2.2}$$

and k is the wavenumber

$$k = \frac{2\pi}{\lambda} \tag{2.3}$$

The cranks were set to achieve an amplitude of 6.25 cm and to allow a wavelength, λ = 1.0L = 1.0 m. The amplitude of the snake increases linearly towards the tail with the amplitude equal to L/16. The tunnel water speed for all tests was 1.0 m/s; therefore, the Reynolds number based on length (Re_L) was approximately 1x10^6. The fixed crank arrangement leaves only one free parameter, the motor speed ω, which allows the value of Cp to be varied. This leads directly to $\frac{Cp}{Uo}$, which is the fundamental nondimensional parameter in undulating bodies: the ratio of wave speed to free-stream speed. During experimental runs, the Cp values were varied from 0.4-2.4.

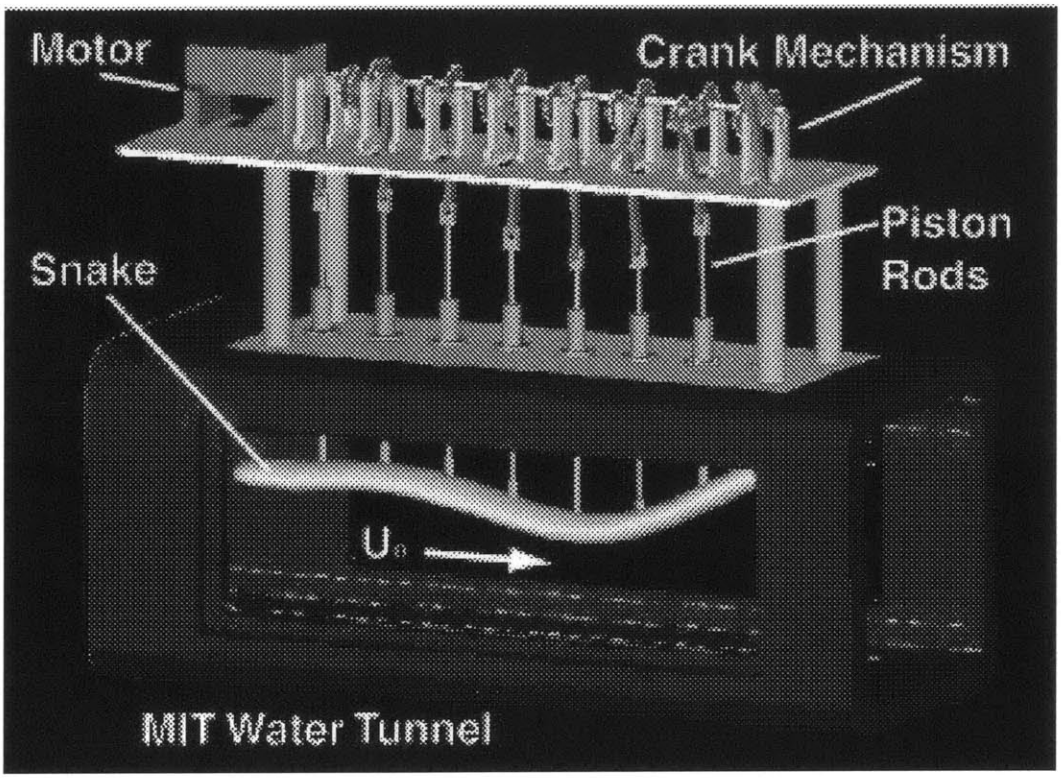

Figure 2-10: CAD drawing of the snake attached to the crank-shaft mechanism. This image identifies the important elements of the experimental set-up. The snake is shown in the test section of the water tunnel. The piston rods extend into the tunnel where they attach to the snake. The piston rods are driven by the crank shaft mechanism which is driven by a motor. The crank shaft mechanism is located on the top face of the tunnel.

Chapter 3

Near-Body Turbulence Study and Wake Velocity Characterization Using Laser Doppler Velocimetry

This chapter details the Laser Doppler Velocimetry (LDV) experiments. LDV was used to study the near body turbulence levels of the snake at two piston positions and to study the mean wake profiles of the snake. Near-body turbulence data is presented. Wake profiles of the velocity measurements are shown.

3.1 Overview of the Laser Doppler Velocimetry Technique

Laser Doppler Velocimetry (LDV) is a nonintrusive method that utilizes a laser and optic system to measure particle velocities. An LDV system consists of a continuous wave laser, transmitting optics (a beam splitter and a focusing lens), receiving optics (a focusing lens and a photodetector), a signal conditioner, and a signal processor. This technique is used for measuring mean velocities and turbulence by measuring a doppler frequency shift. The fluid is seeded with small tracer particles that follow the flow. Light waves produced by the laser beams reflect when a particle passes through

the intersection volume formed by the two coherent laser beams. A detector receives this scattered light that has components from both beams. The two intersecting beams form a fringe pattern of high and low intensity. The intensity is dependent on the difference between the optical path lengths of the two components. The fringes in space move across the detector at the Doppler difference frequency. When the particle traverses this fringe pattern, the scattered light fluctuates in intensity with a frequency equal to the velocity of the particle divided by the fringe spacing [15].

3.2 Experimental Set-up of the LDV System

A backscattering LDV system was used in combination with a traverse positioning system to make velocity measurements. A 6-Watt argon ion laser (continuous) was used in conjunction with TSI, Inc. optics. The laser is backscattering and reflects back off the particles to the receiving optics. The traverse system allows the laser to be positioned to a 0.01 mm accuracy. A Dantec data acquisition system allows u and v velocities to be measured and then the data is averaged into angle bins based on the 360° of motion. Mean data was taken in the wake to determine the wake profiles.

In this experiment, the LDV measurements were synched with the body motion through an inductance encoder on the drive shaft. This allowed the data to be related directly to the swimming phase of the snake. The snake is run through many cycles allowing the data to be phase averaged over many cycles. The LDV gives the mean velocity components ($\overline{u}$ and $\overline{v}$), and allows for the calculation of the velocity fluctuations (u' and v'). Each near body turbulence data point represents $\sim$ 36,000 measurements. For the wake, data from at least 30 cycles of the swimming motion was used.

3.3 Near Body Turbulence Measurements of the Snake

Near body turbulence levels were studied at two positions along the snake, at piston five and six (see figure 2-8). Piston five is a distance of 0.72L and piston six is a distance of 0.80L, where L is the length of the snake. Measurements were made at very small distances from the snake in order to assess turbulence production and control near the undulating body. Then data was taken at incremental steps away from the snake body all of the way into the freestream.

Data was taken for both the crest and trough positions at pistons five and six for $\frac{Cp}{Uo}$ values of 0.4, 0.8, 1.2, and 2.0. Data was bin-averaged into 360 bins of one degree each, with approximately 100 points per bin. Data points that were more than three standard deviations away were removed during data processing in Matlab. Five of the bins were then combined to analyze the data.

The local phase locked velocity component (u) can be statistically split into two parts, the average velocity component $\bar{u}$ and its fluctuations u':

$$u = \bar{u} + u' \tag{3.1}$$

The standard deviation or rms of the velocity fluctuations can be used as a measurement of turbulence intensity. The standard deviation is calculated by equation 3.2:

$$\bar{u}'^2 = \frac{\sum \frac{(u-\bar{u})^2}{n}}{U_o^2} \tag{3.2}$$

where n is the number of samples and U_o is the inflow velocity. The base level of turbulence intensity for the Water Tunnel is approximately 0.0009, equivalent to about three percent turbulence.

Turbulence intensity is shown for data taken at pistons five and six as a function of $\frac{Cp}{Uo}$ for various distances. The axes on these graphs show turbulence intensity normalized by inflow velocity vs. $\frac{Cp}{Uo}$. The turbulence intensity $\overline{u'^2}$ is represented in

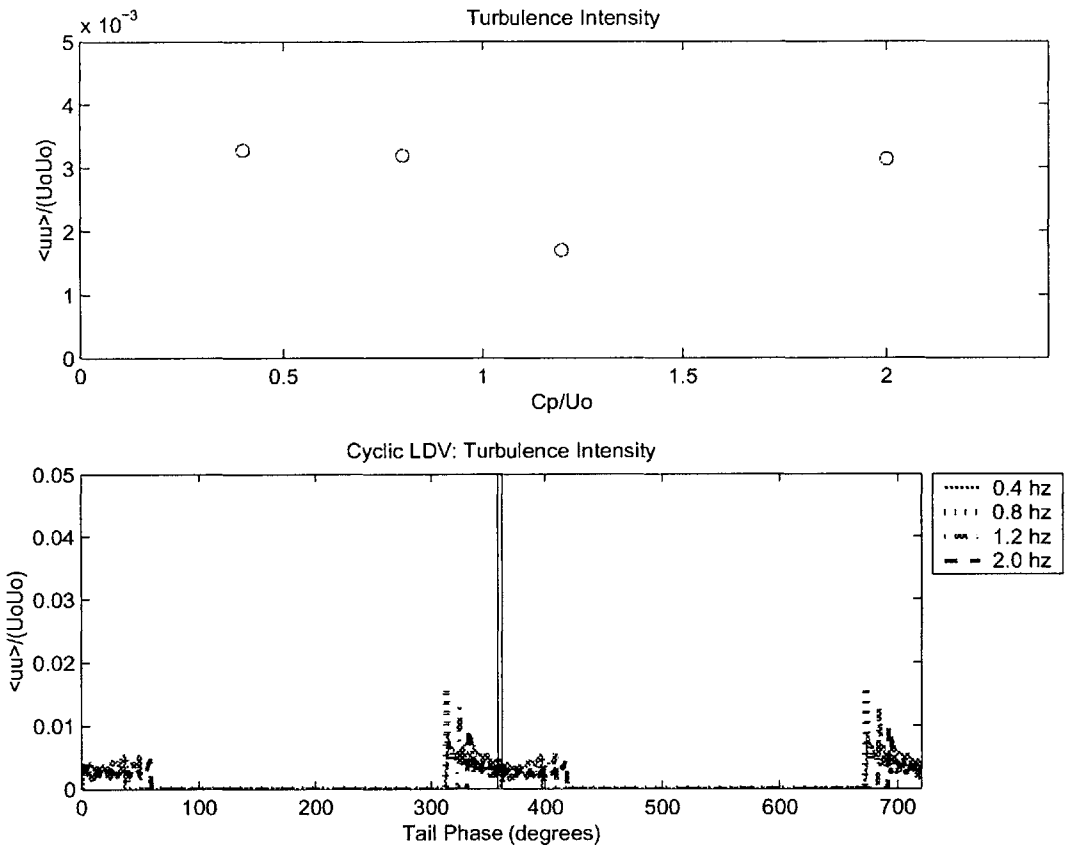

Figure 3-1: Turbulence intensity for piston five trough position at a distance of 8 mm away from the snake body. The top plot shows the average turbulence intensity at four values of $\frac{Cp}{Uo}$. The lower plot shows the turbulence intensity measured over 360 degrees, with two cycles being shown. Plots for each distance for the piston five and six data are shown in appendices A and B respectively.

these plots by the symbol $< uu >$. The distances shown are the distances from the snake body.

3.3.1 Near Body Turbulence Results at Piston Five

Appendix A shows the turbulence intensity results for each distance away from the snake. Each plot in appendix A contains the data for the four different values of $\frac{Cp}{Uo}$ (0.4, 1.2, 2.0, 2.4) that were run. In addition, the cyclic data over all 360° is shown. An example of a run at a distance of 8 mm below the snake is shown in figure 3-1. The area in the cyclic data plot where there is no data represents the area where the

snake body crosses in front of the laser beam. The two vertical lines marked on the plot indicate the region in which the data for the turbulence intensity calculation was made. Several distances are plotted for the trough position in figure 3-2 and for the crest position in figure 3-3.

The trough data (figure 3-2) shows the highest intensity at positions closest to the snake body which is expected. Data taken too close to the snake body can result in the laser beam being clipped by the body; therefore, data closer than 4 mm to the body is not shown. This means that the laser is focused on the body and not on particles in the water and therefore, data is not recorded. As distance from the snake increases, the turbulence levels decrease. When 8 mm away from the snake is reached, a minimum for $\frac{Cp}{Uo} = 1.2$ develops. The low that develops for $\frac{Cp}{Uo} = 1.2$ remains visible until a distance of 18 mm. After this distance, the fluid turbulence level appears to stabilize. This fluid no longer feels the effect, or feels a minimum effect of the snake body. The fluid appears to reach the turbulence level of the freestream at a distance of 30 mm. The minimum at $\frac{Cp}{Uo} = 1.2$ is consistent with the results obtained by Techet shown in figure 1-7.

The data taken when the snake was in the crest position is shown in figure 3-3. The distances closest to the snake again show the highest turbulence. However, no minimum for $\frac{Cp}{Uo} = 1.2$ occurs. High points exist at $\frac{Cp}{Uo} = 0.4$ and 1.2 and low points at $\frac{Cp}{Uo} = 0.8$ and 2.0. The shape of this plot is unlike the results shown by Techet. The three-dimensional shape of the snake allows flow to go over the sides of the snake. This does not occur for Techet's mat as it spanned the entire width of the tunnel. The flow over the sides of the snake may affect the near body turbulence levels. Also, since the snake does not span the tunnel, there is an increased effect of the pistons in creating turbulence.

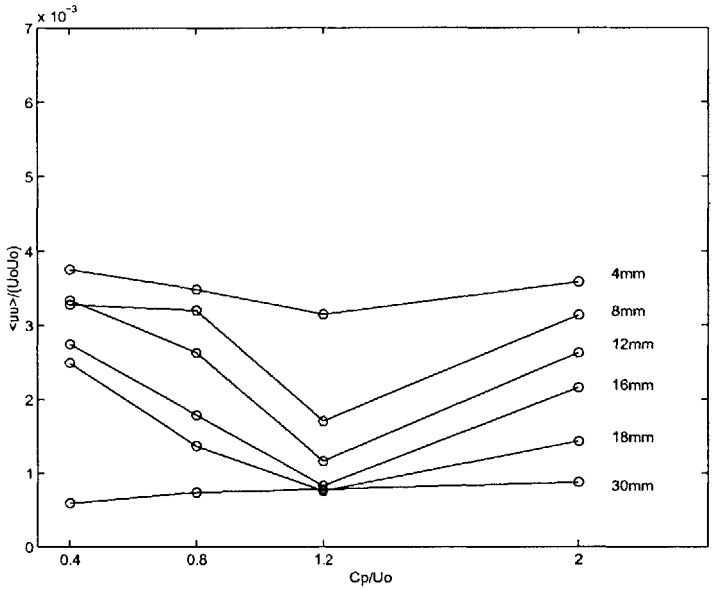

Figure 3-2: Summary of turbulence intensity at the piston five trough position. The turbulence reduction at $\frac{Cp}{Uo} = 1.2$ can be seen. This agrees with previous two-dimensional waving plate studies. At a distance of 30 mm away from the body, the turbulence level has reached the level of the freestream in the tunnel.

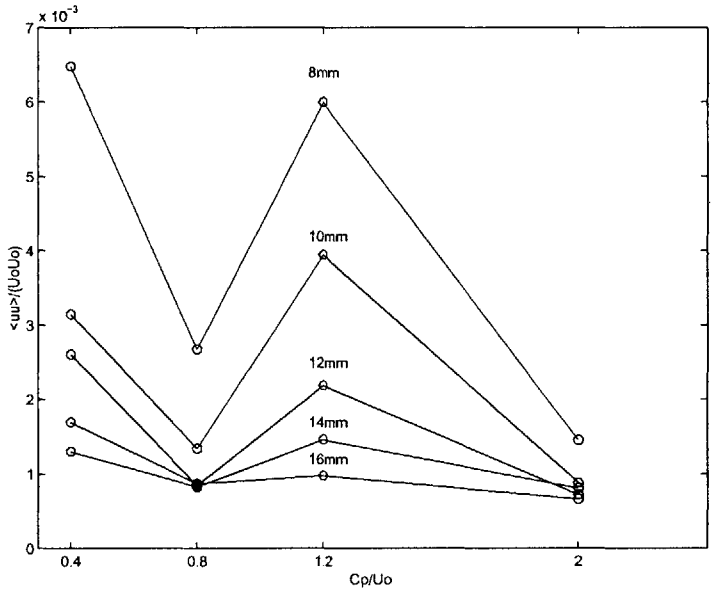

Figure 3-3: Summary of turbulence intensity at the piston five crest position. The turbulence maxima at $\frac{Cp}{Uo} = 1.2$ can be seen. This is unlike the two-dimensional case which shows a turbulence minimum. At a distance of 16 mm away from the body, the turbulence level has reached the level of the freestream in the tunnel.

3.3.2 Near Body Turbulence Results at Piston Six

Appendix B shows the turbulence intensity results for each distance away from the snake. Turbulence intensity data taken at the crest and trough positions for piston six is shown in figures 3-4 and 3-5. For both the trough and crest positions, the highest turbulence is located close to the snake body. Within the trough, as distance from the snake increases, turbulence levels decrease for all $\frac{Cp}{Uo}$. As the distance from the snake further increases, a minimum for $\frac{Cp}{Uo} = 1.2$ appears. Turbulence intensity reaches tunnel levels of three percent for all $\frac{Cp}{Uo}$ at a distance of 55mm from the snake body. At the crest position, a decrease in turbulence is again seen as the distance from the snake increases. However, now a maximum is seen in turbulence intensity for $\frac{Cp}{Uo}$= 1.2 for 12 mm - 16 mm. This is opposite the case for the trough where $\frac{Cp}{Uo} =$ 1.2 shows the lowest turbulence in the crest. Tunnel turbulence levels are reached at 23 mm.

Turbulence reduction is demonstrated for this 3D case for the trough position which supports previous data for 2D waving plates. However, in the 2D case, the crest position shows a minimum at $\frac{Cp}{Uo} = 1.2$ unlike the 3D where a maximum occurs. Again, the differences could be a result of three-dimensional effects of flow around the snake body which is unlike Techet's flat plate that spanned the entire section of the tunnel, preventing flow around the edges. In addition, this snake data was taken further downstream at piston six where the amplitude is larger.

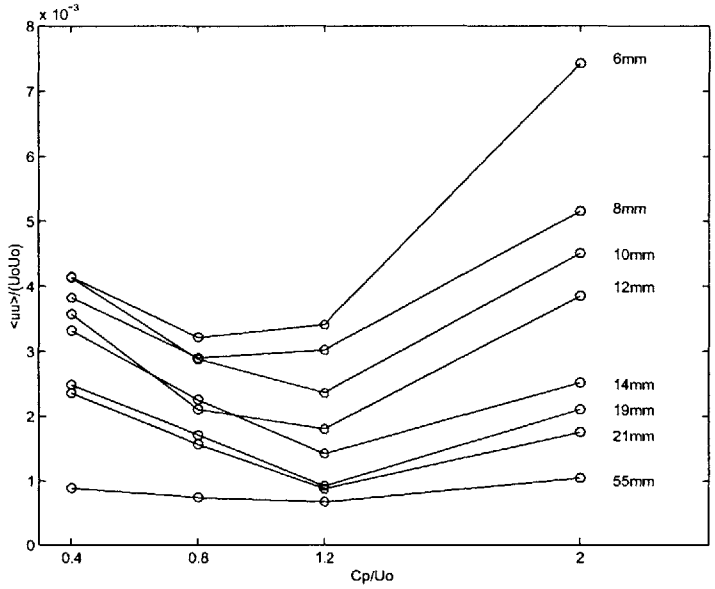

Figure 3-4: Summary of turbulence intensity at the piston six trough position. A turbulence minimum appears for $\frac{Cp}{Uo} = 1.2$ starting at 12 mm away from the body. The minimum for $\frac{Cp}{Uo} = 1.2$ agrees with the two-dimensional studies. At a distance of 55 mm away from the body, the turbulence level reaches the level of the freestream.

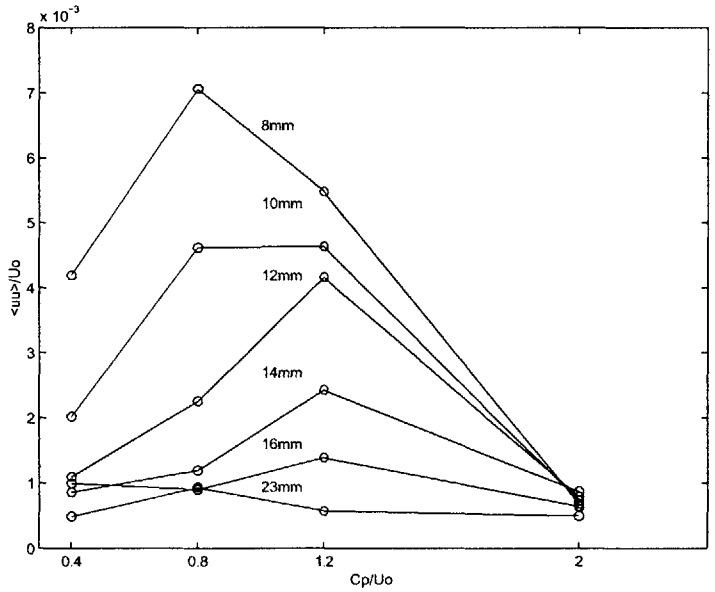

Figure 3-5: Summary of turbulence intensity at the piston six crest position. A turbulence maximum appears for $\frac{Cp}{Uo} = 1.2$. This is an opposite effect than is seen for the crest position in two-dimensional studies. At a distance of 23 mm away from the body, the turbulence level has reached the level of the freestream.

3.4 Wake Velocity Results

Data was taken at a fixed position 108 mm aft of the snake tail (~0.1L). The laser was positioned at Y = 0 and Z = 0. The $\frac{Cp}{Uo}$ values of 0.4, 0.6, 0.8, 1.0, 1.2, 1.4, 1.6, 1.8, and 2.0 were run. The velocity plot, figure 3-6, shows that as $\frac{Cp}{Uo}$ increases, the velocity increases towards the inflow velocity value. Since this position is influenced by the pistons, a velocity deficit below the level of the incoming velocity appears. Figure 3-7 shows that as $\frac{Cp}{Uo}$ increases, the turbulence intensity increases in the wake. However, a sudden drop is seen for $\frac{Cp}{Uo} = 1.0$ and 1.2 indicating a reduction of turbulence intensity.

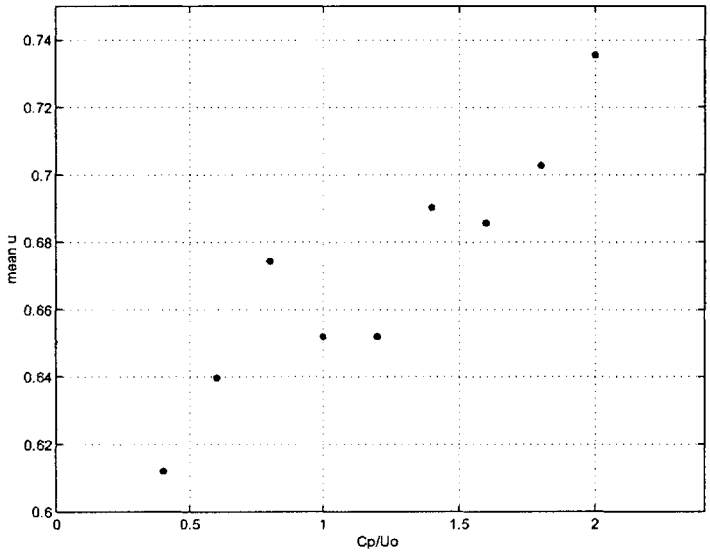

Figure 3-6: $\overline{u}$ velocity component in the wake of the snake at a fixed position. This data was taken 108 mm after of the tail at Y and Z = 0. As $\frac{Cp}{Uo}$ increases, the velocity component increases towards the level of the freestream. However, all of the velocities shown are significantly lower than the inflow velocity.

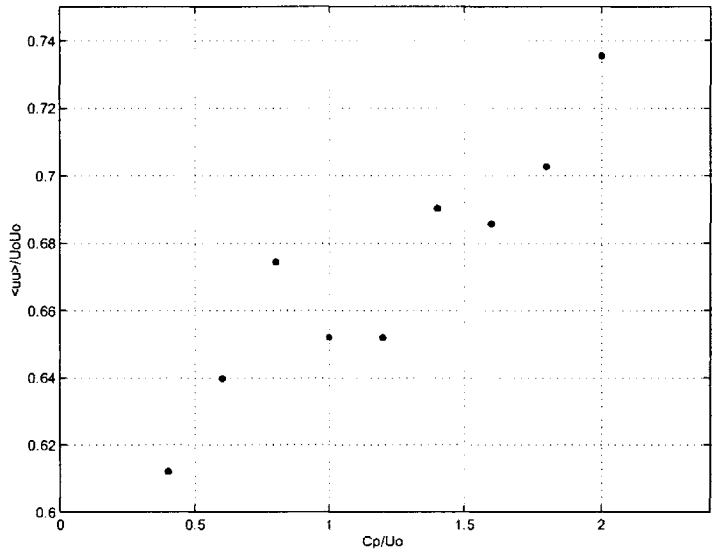

Figure 3-7: Turbulence intensity, (u'u'),in the wake of the snake at a fixed position. This data was taken 108 mm after of the tail at Y and Z = 0. The turbulence intensity tends to increase with an increase of $\frac{Cp}{Uo}$. A sudden drop though is seen for $\frac{Cp}{Uo}$ = 1.0 and 1.2.

3.5 Wake Survey Profiles

LDV was used to perform a wake survey, of mean velocity only, in a plane normal to the snake's axis at a distance of 108 mm, ~ 0.1*L, aft of the snake tail. The data was taken in the Y-Z plane. The goal of the survey was to bound the extent of the robot's wake, and to assess the impact of the pistons on the wake flow. Furthermore, by characterizing the velocity an understanding of the wake of the snake can be found. Measurements of $\overline{u}$, $\overline{v}$, u', and v' were made.

The wake survey was conducted over a Y range of 160 mm and a Z range of 180 mm. Data was taken at 20 mm increments; thus, making for a 9 x 10 grid. The coordinates used were based off a (X,Y,Z) = (0,0,0), position set at the center point of the tip of the tail when the snake is set at its mean position. The snake's mean position occurs when the tip of the tail is at its mean position. Data was taken for $\frac{Cp}{Uo}$ = 0.4, 0.8, 1.2, 1.6, 2.0, and 2.4. Because of the limitations of obtaining data in the tunnel with LDV, an area identified through the pressure measurements described in the next section as representing a quarter of the wake was selected and LDV data

was taken in a slightly extended area of this quadrant.

3.5.1 Wake Velocity $\overline{u}$ Component

Figures 3-8 to 3-13 show the wake velocity profiles of $\overline{u}$ for $\frac{Cp}{Uo}$ = [0.4, 0.8, 1.2, 1.6, 2.0, and 2.4]. These are cuts in the Y-Z plane. The outline of the mean position of the tail is marked by the semi-oval. The dashed line marks regions of symmetry of an area that will be used in chapter 5 to calculate thrust. The tip of the tail has an amplitude of 62.5 mm, therefore, in the figures shown the tail's motion is present during some part of its cycle in the region from -62.5 mm to 40mm. It should be noted that when the snake is at its lower range, the piston rods enters the area shown in the figures and therefore they affect parts of the quadrant shown.

In all of these plots a lower velocity region exists close to the tail with the lowest velocity being above the mean position of the tail. At further distances from the tail, the freestream velocity of 1.0 m/s should be obtained. For many of the plots, this velocity is not obtained which may indicate that there are fluctuations in the tunnel inflow velocity. For the lower values of $\frac{Cp}{Uo}$ the velocity reaches lower values close to the tail than for the higher $\frac{Cp}{Uo}$ values.

For $\frac{Cp}{Uo} = 0.4$ (figure 3-8) and $\frac{Cp}{Uo} = 0.8$ (figure 3-9), the profiles are very similar. A steady increase in velocity occurs as distance from the tail increases. The contour lines are quite symmetric around the body. There are no significant structures formed it either wake profile.

$\frac{Cp}{Uo} = 1.2$ (figure 3-10) shows the same steady increase in velocity as the distance from the snake increases. However, several interesting structures appear. Below the snake two areas of closely spaced contours are present. In addition, the contours surrounding the tail are no longer uniform. Instead the lines include some curved areas. Below the tail, a slight central downwards peak is present.

For $\frac{Cp}{Uo} = 1.6$ (figure 3-11) the velocity increases away from the tail much faster than the previous plots. The contours contain many curved areas. The contours beneath the snake are no longer straight. Instead, the contours show dips. A significant central peak area below the snake is present. On the right side of this peak

is an upwards indentation. The contours below the snake suggest that the snake is pushing the fluid down significantly in its center.

The $\frac{Cp}{Uo} = 2.0$ plot (figure 3-12) shows the development of a large central peak below the snake that extends to the bottom of the tunnel. The 0.98 m/s contour line curves in and then comes out towards the side. When the snake moves up and down, flow travels around the edges. As a result, not all of the fluid is pushed down by the snake. The edge flow may account for the shape of the contours. The snake is thickest in its center at Y=0 where the central rib exists. The edges of the snake tail are the thinnest regions. The combination of the thick rib and the thin edge may further explain these shapes. To the right of the snake tip, a circular area exists that may be a result of the flow around the side or a vortex shed off the trailing edge of the snake.

The plot of $\frac{Cp}{Uo} = 2.4$ (figure 3-13) again shows the peak structure. However, this peak contains a central circular region. To the right of the peak there is a prominent oval shaped structure of higher than freestream velocities.

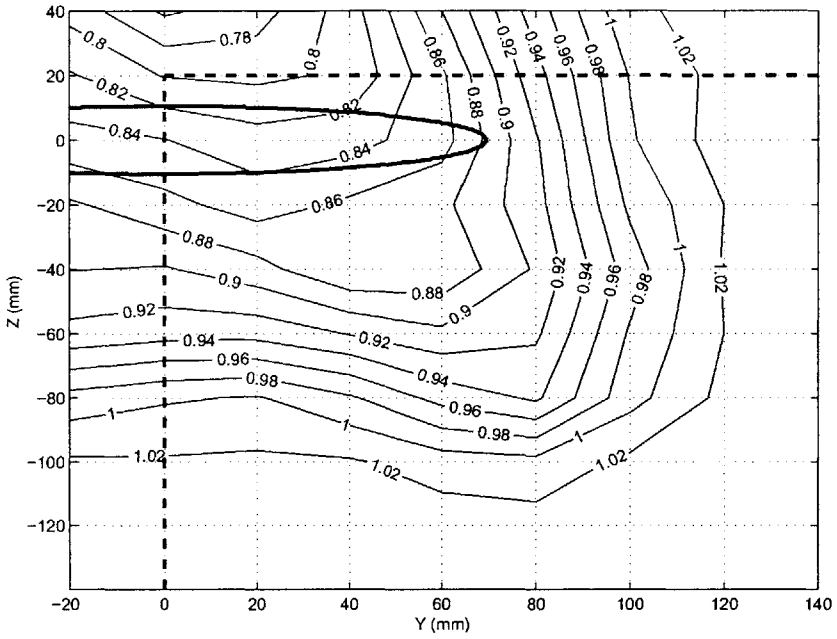

Figure 3-8: $\overline{u}$ velocity component for $\frac{Cp}{Uo}$=0.4

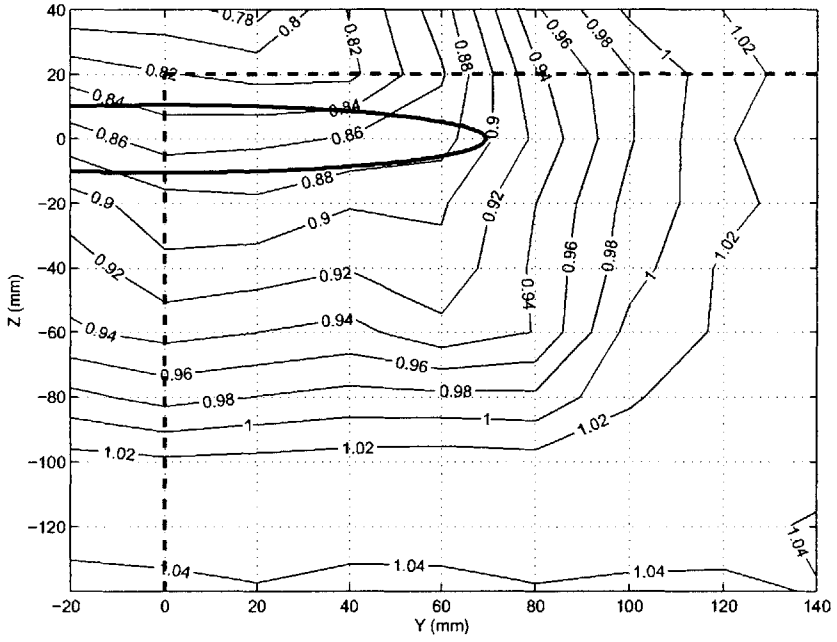

Figure 3-9: $\overline{u}$ velocity component for $\frac{Cp}{Uo}$=0.8

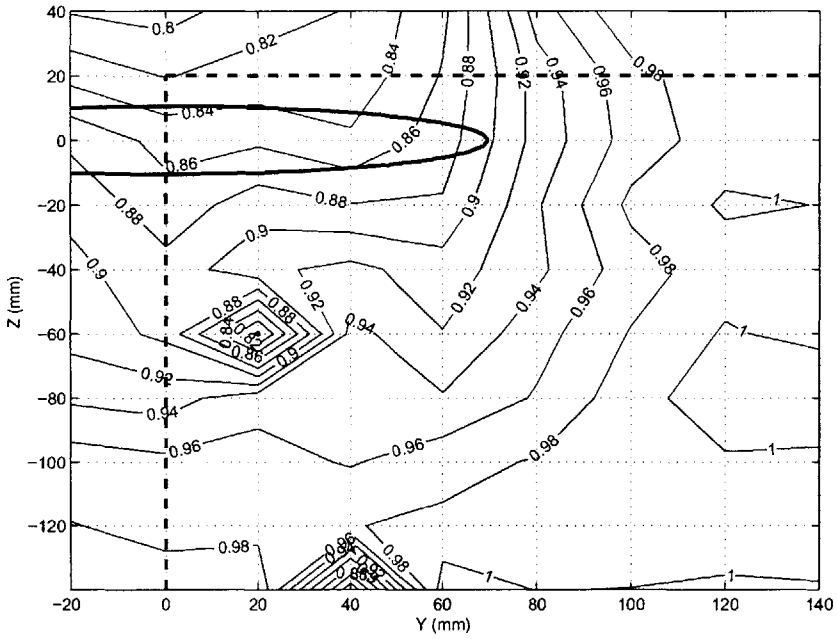

Figure 3-10: $\overline{u}$ velocity component for $\frac{Cp}{Uo}$=1.2

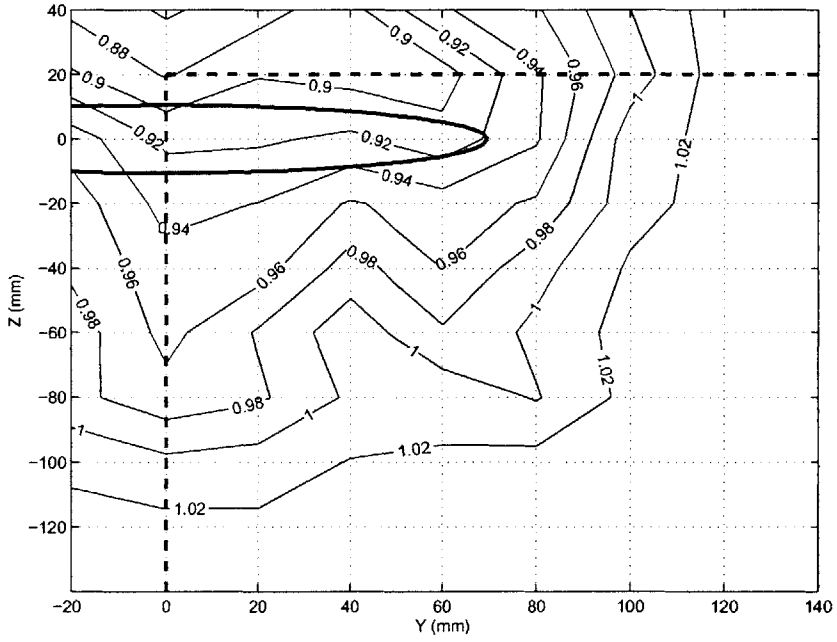

Figure 3-11: $\overline{u}$ velocity component for $\frac{Cp}{Uo}$=1.6

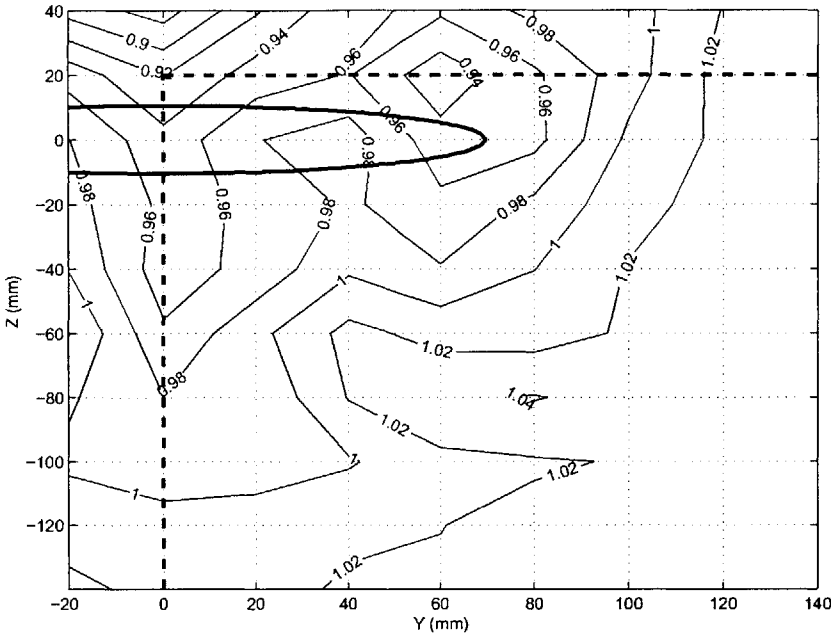

Figure 3-12: $\overline{u}$ velocity component for $\frac{Cp}{Uo}$=2.0

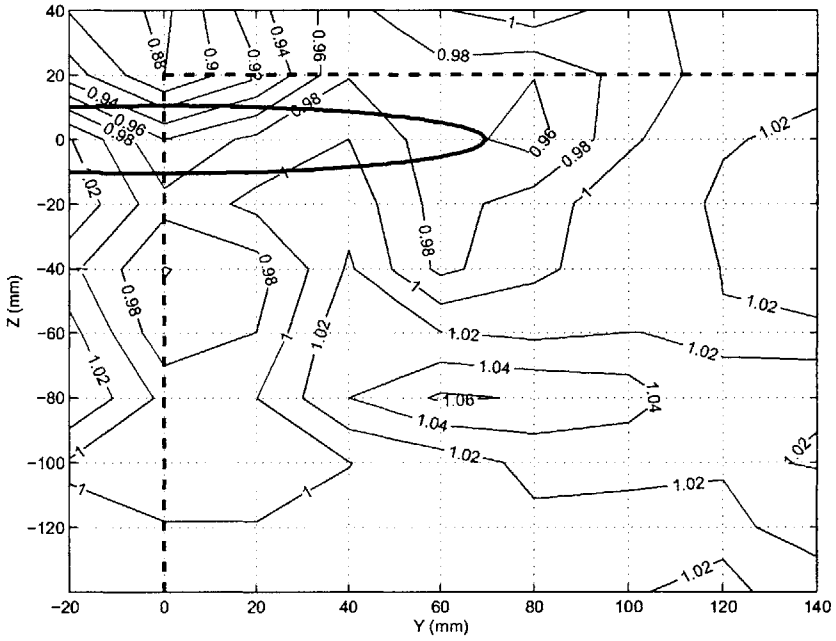

Figure 3-13: $\overline{u}$ velocity component for $\frac{Cp}{Uo}$=2.4

3.5.2 RMS of the u Velocity Component: u'

Figures 3-14 through 3-19 show the rms of the velocity component which is defined as:

$$u' = \sqrt{\overline{u'^2}} \tag{3.3}$$

Each of the plots shows the highest value closest to the snake body and values that approach zero at distances away from the snake. $\frac{Cp}{Uo} = 0.4$ and 0.8 show similar values of u'. However, $\frac{Cp}{Uo} = 1.2$, shows much lower values. Then, as the value of $\frac{Cp}{Uo}$ increases, u' also increases. For $\frac{Cp}{Uo} = 2.0$ and 2.4, the u' level reaches values of 0.3 near the snake.

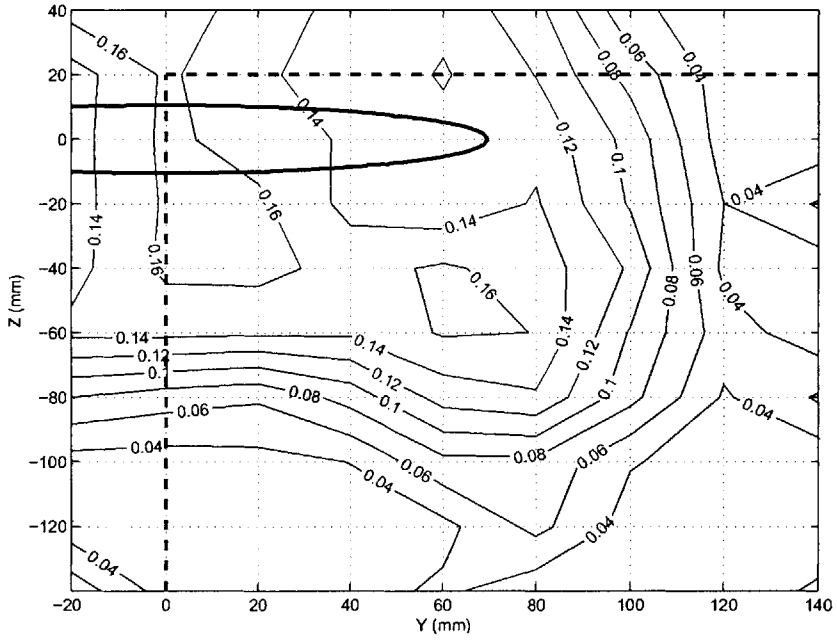

Figure 3-14: u' velocity fluctuations for $\frac{Cp}{Uo}$=0.4

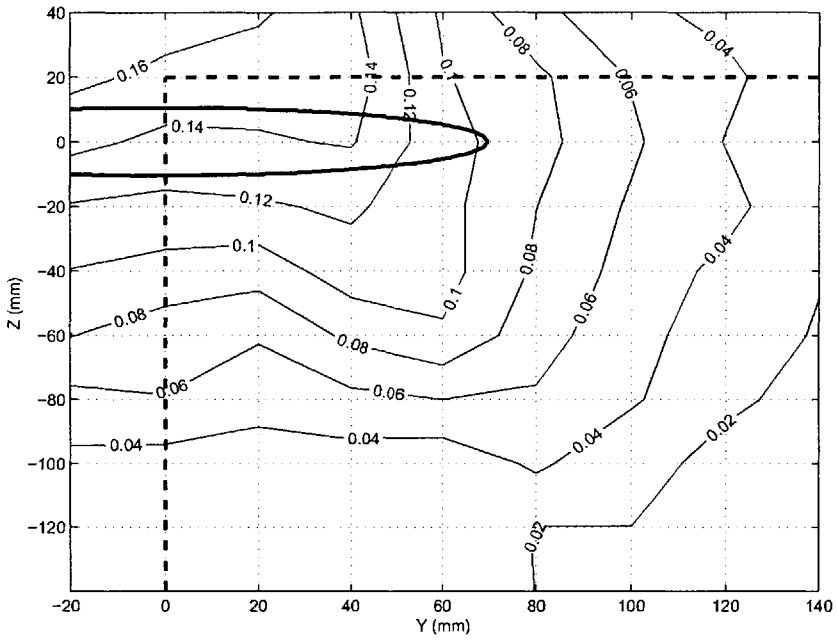

Figure 3-15: u' velocity fluctuations for $\frac{Cp}{Uo}$=0.8

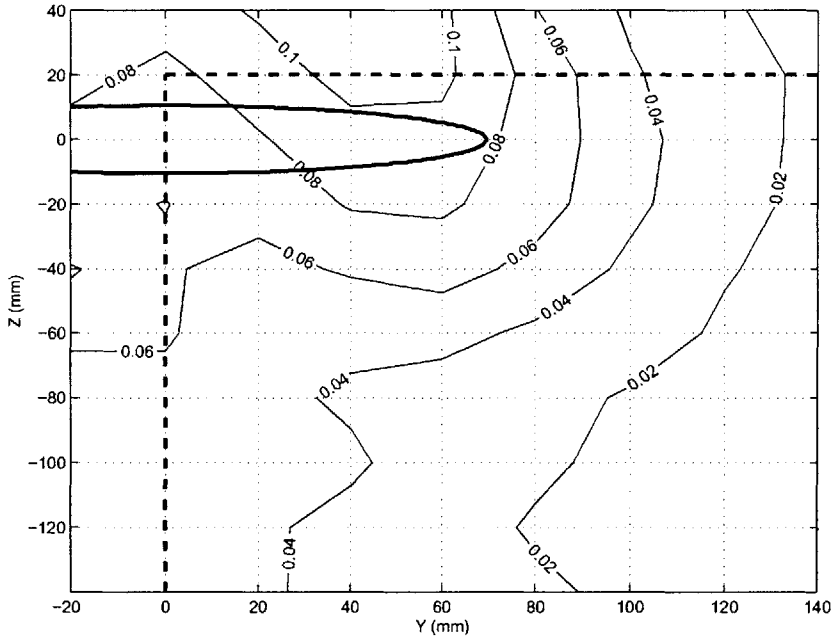

Figure 3-16: u' velocity fluctuations for $\frac{Cp}{Uo}$=1.2

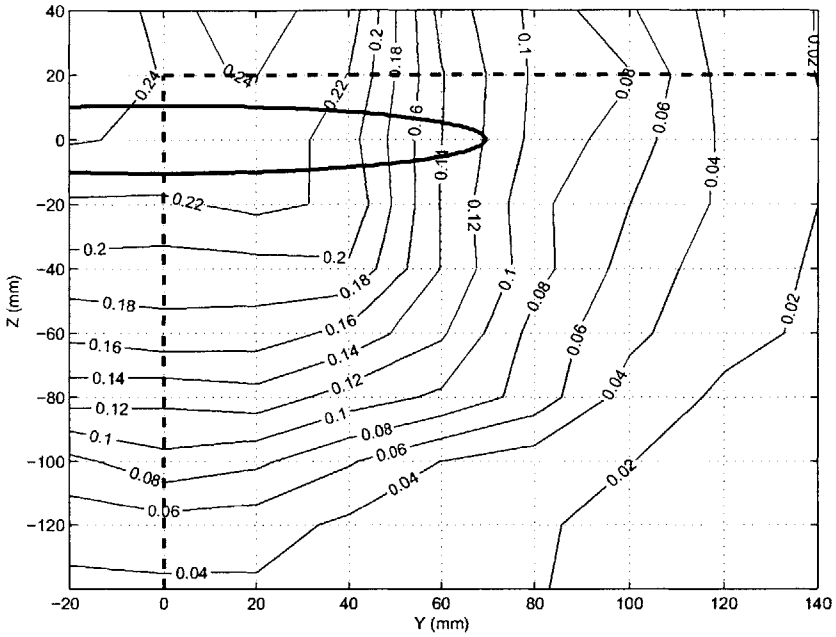

Figure 3-17: u' velocity fluctuations for $\frac{Cp}{Uo}$=1.6

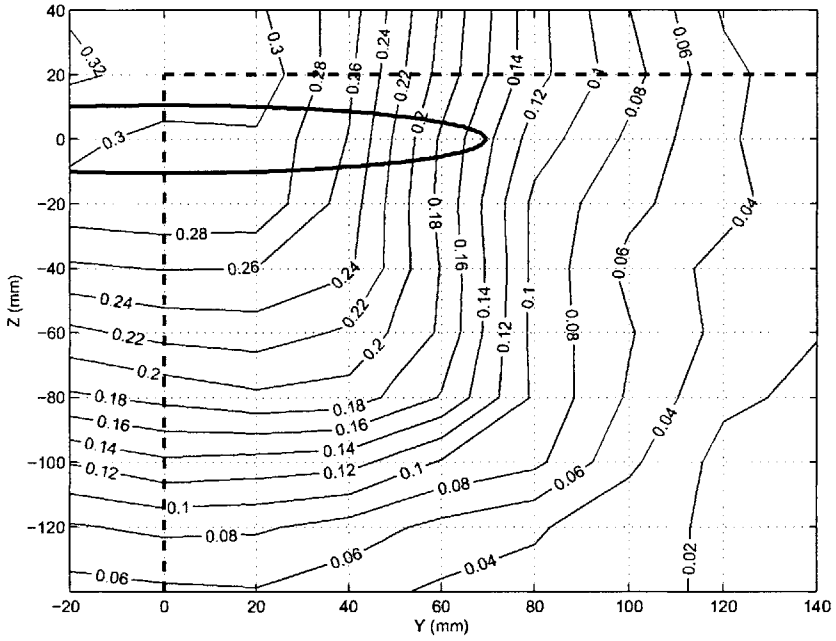

Figure 3-18: u' velocity fluctuations for $\frac{Cp}{Uo}$=2.0

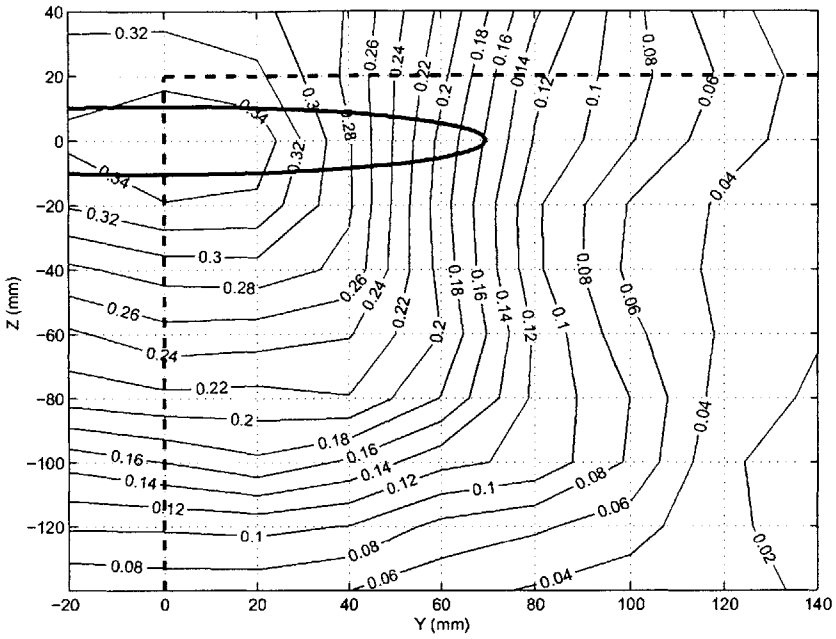

Figure 3-19: u' velocity fluctuations for $\frac{Cp}{Uo}$=2.4

3.5.3 Wake Velocity Total u Component

The total u velocity component is the sum of the $\overline{u}$ and its fluctuations, u'. The fluctuations are significant therefore, the wake velocity now shows values of up to 1.08 m/s for $\frac{Cp}{Uo}$ = 0.4 and 0.8. Since the fluctuations were significantly less for $\frac{Cp}{Uo}$ = 1.2, the total u velocity plot shows that the maximum velocity is 1.04 m/s. This velocity is only in a very small region and the dominant velocity is from 1.00-1.02 m/s. $\frac{Cp}{Uo}$ = 1.6 and 2.0 show higher velocities than the $\frac{Cp}{Uo}$ = 1.2 case. $\frac{Cp}{Uo}$ = 2.4 show significant velocities reaching 1.18 m/s.

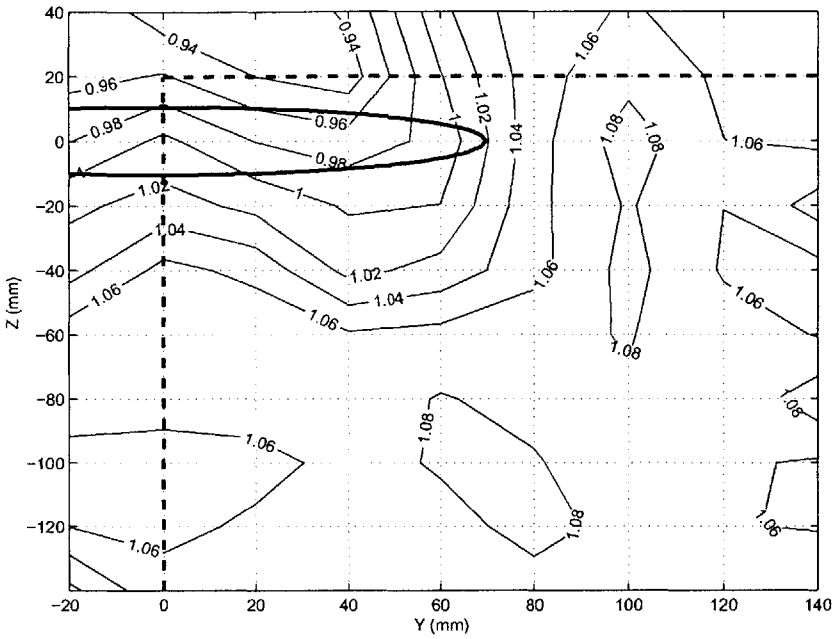

Figure 3-20: u velocity for $\frac{Cp}{Uo}$=0.4

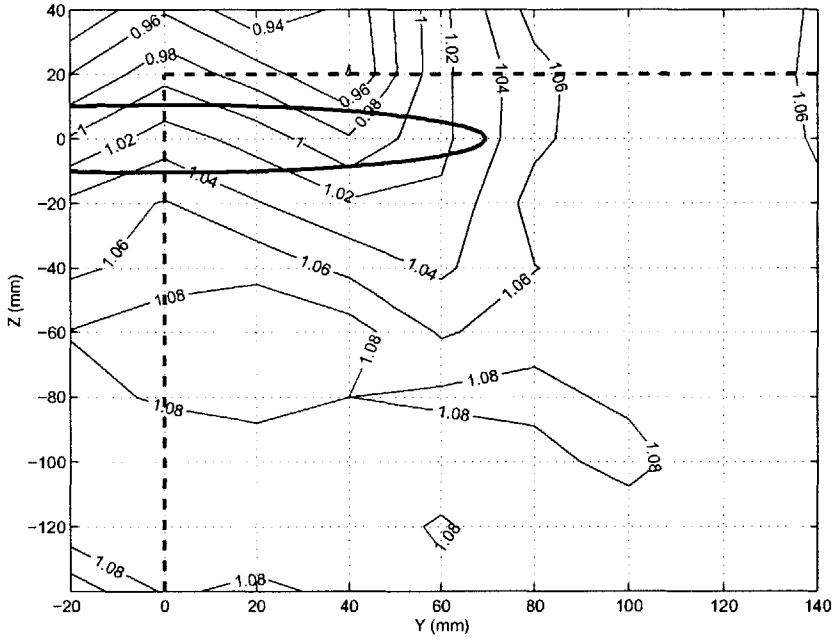

Figure 3-21: u velocity for $\frac{Cp}{Uo}$=0.8

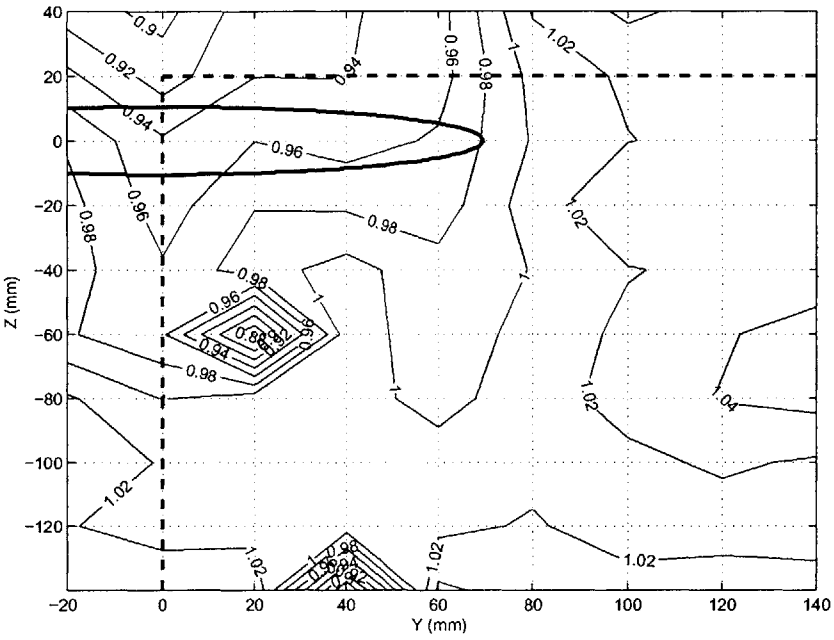

Figure 3-22: u velocity for $\frac{Cp}{Uo}$=1.2

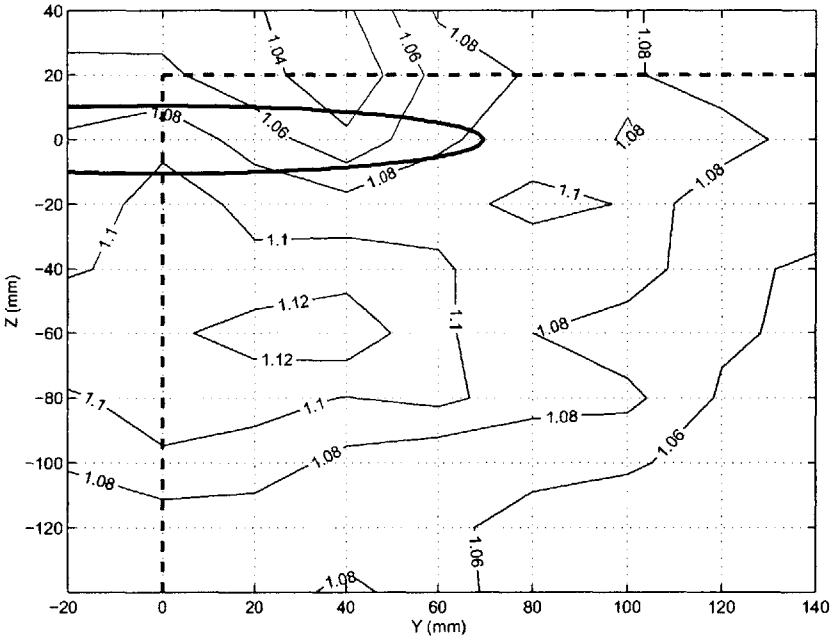

Figure 3-23: u velocity for $\frac{Cp}{Uo}$=1.6

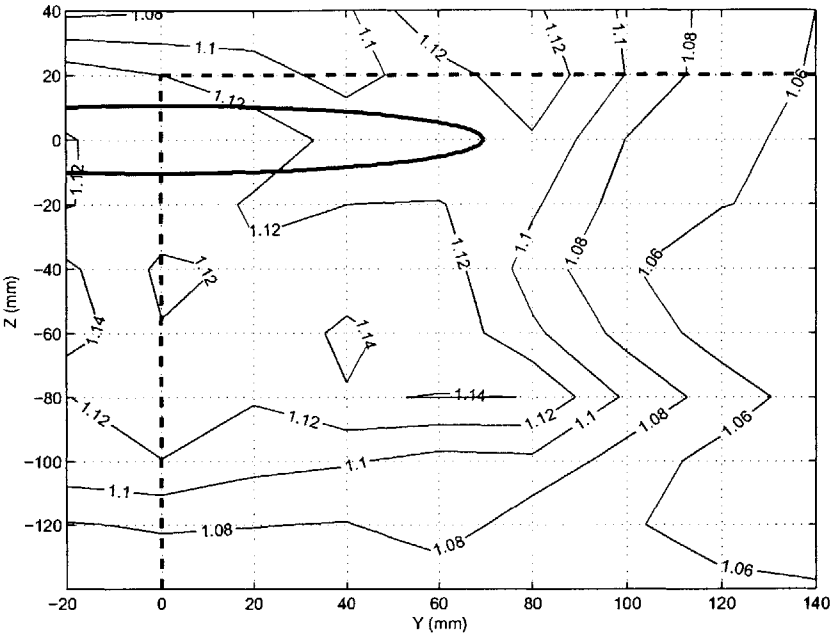

Figure 3-24: u velocity for $\frac{Cp}{Uo}$=2.0

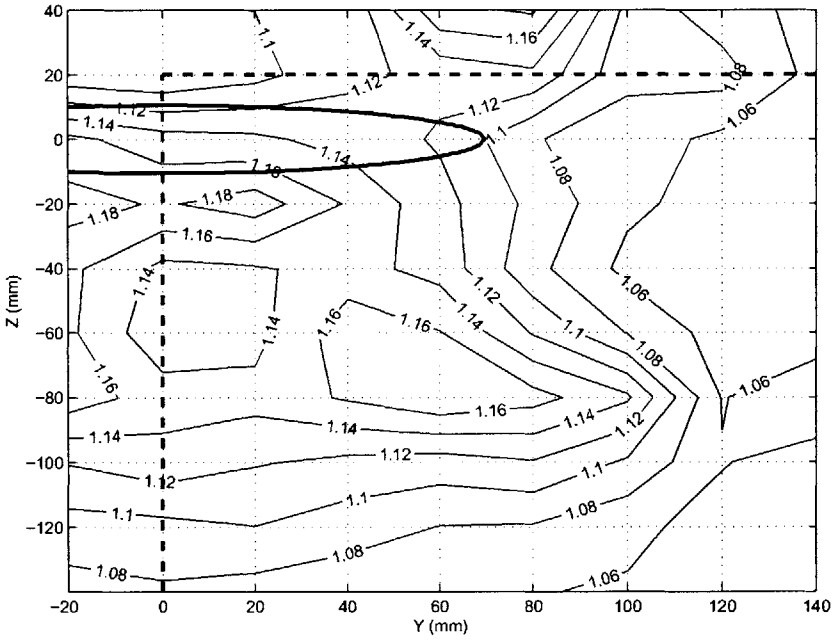

Figure 3-25: u velocity for $\frac{Cp}{Uo}$=2.4

3.5.4 Wake Velocity $\overline{v}$ Component

Figures 3-26 through 3-31 show the $\overline{v}$ component of the velocity. These values are much smaller than both the $\overline{u}$ and the u' values. The $\overline{v}$ velocity increases in the region close to the snake; however, the greatest velocity seen on any of the plots is only 0.12 m/s. This is an opposite effect than is shown in the plots of $\overline{u}$ which show the highest velocity away from the snake. All of the plots show a circular area in the top right. This may be an effect of the vortices shed from the tail. For $\frac{Cp}{Uo}$ = 1.6, 2.0, and 2.4, an area on the right lower side of the tail is present and extends significantly.

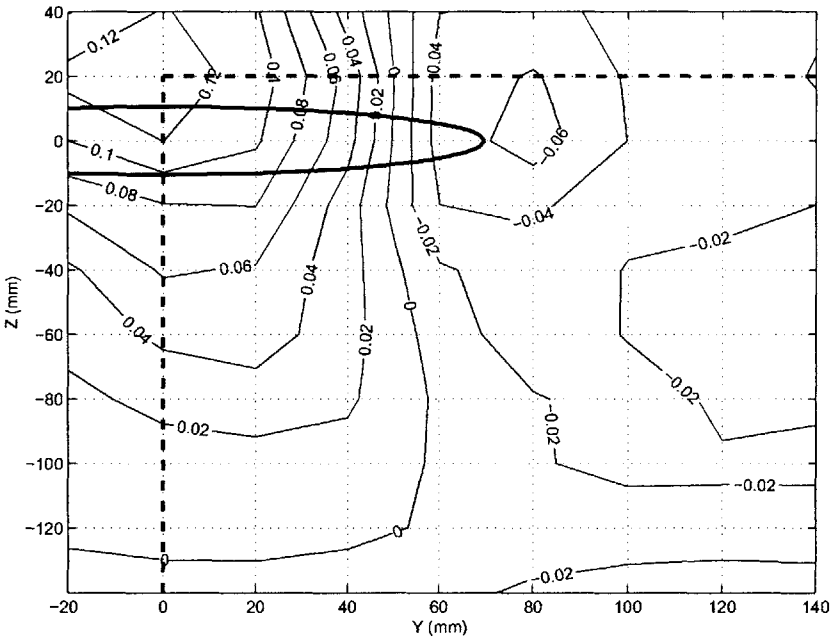

Figure 3-26: $\overline{v}$ velocity component for $\frac{Cp}{Uo}$=0.4

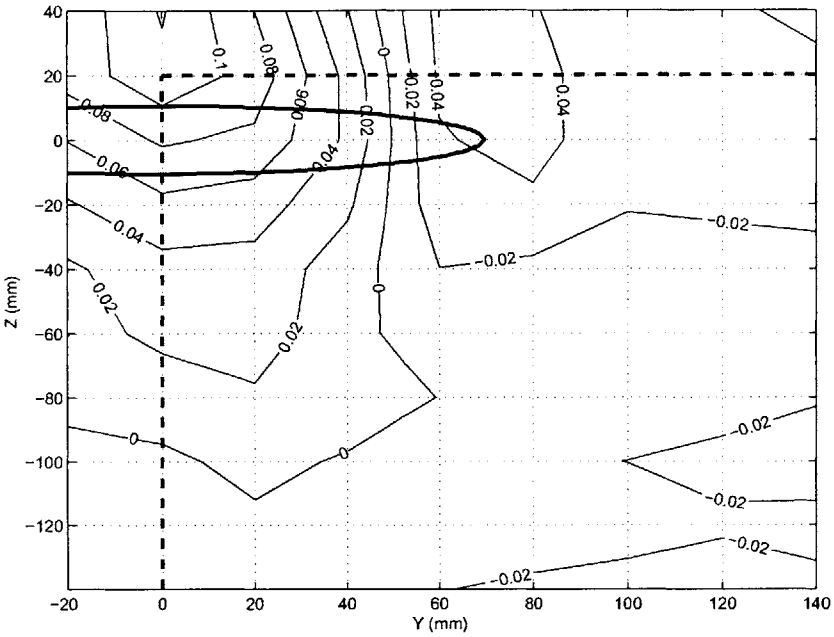

Figure 3-27: $\overline{v}$ velocity component for $\frac{Cp}{Uo}$=0.8

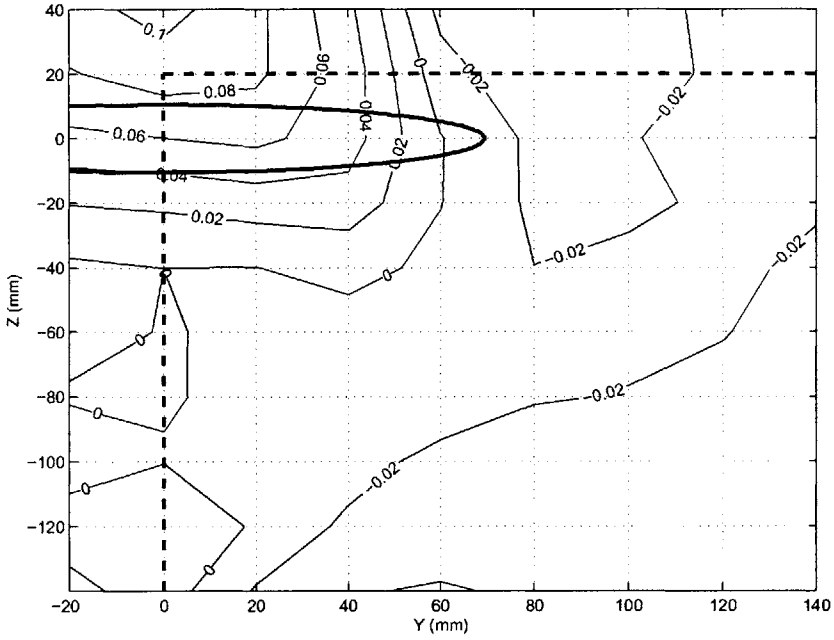

Figure 3-28: $\overline{v}$ velocity component for $\frac{Cp}{Uo}$=1.2

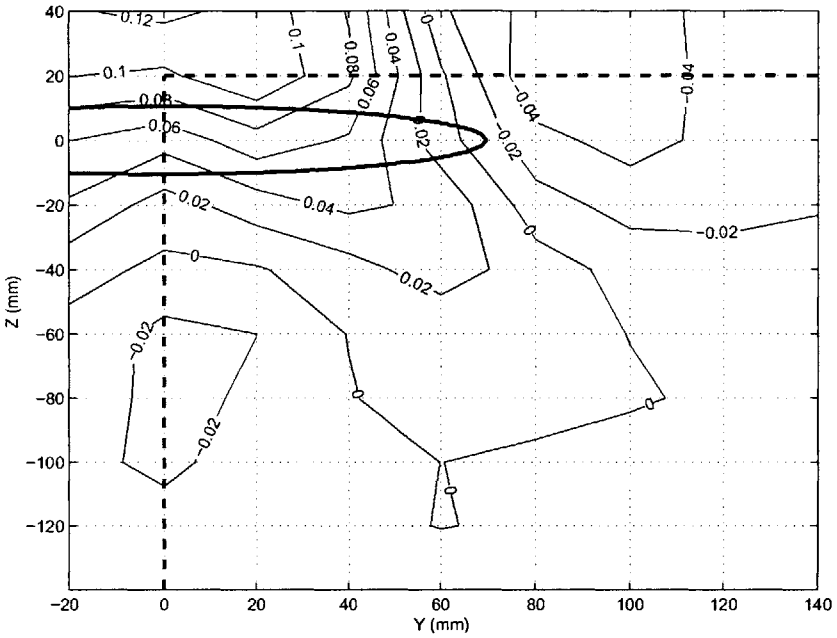

Figure 3-29: $\overline{v}$ velocity component for $\frac{Cp}{Uo}$=1.6

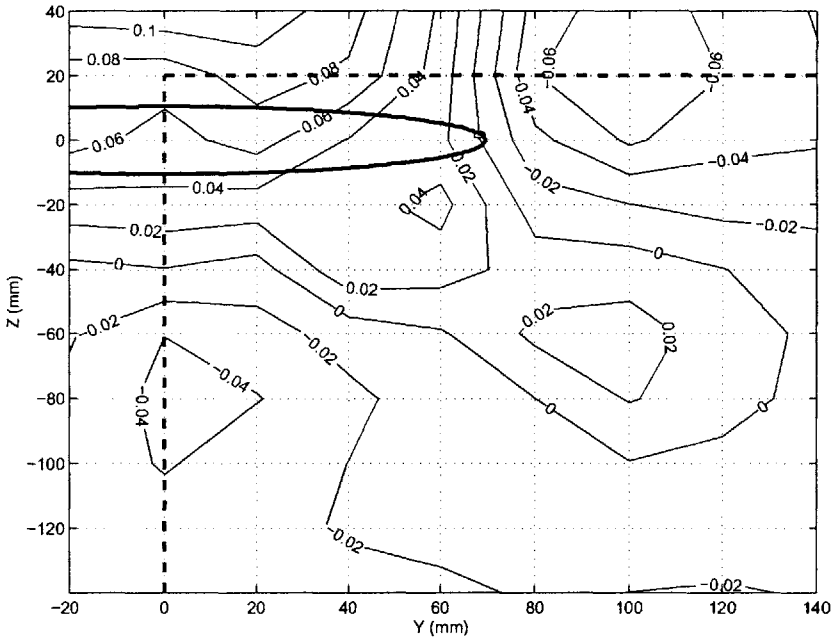

Figure 3-30: $\overline{v}$ velocity component for $\frac{Cp}{Uo}$=2.0

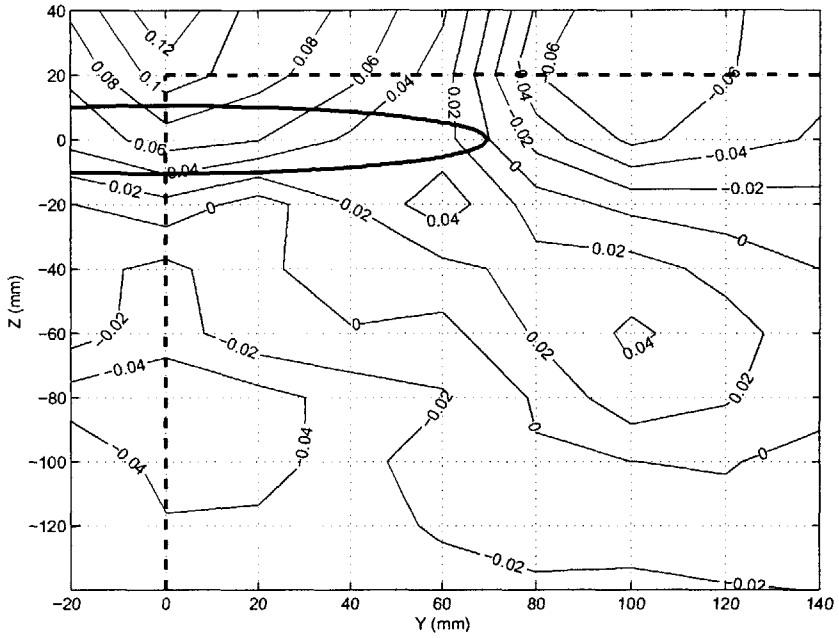

Figure 3-31: $\overline{v}$ velocity component for $\frac{Cp}{Uo}$=2.4

3.5.5 RMS of the v Velocity Component: v'

Figures 3-32 through 3-37 show the rms of the v velocity component. The v' component is defined in the same way as u' was in section 3.5.2. The v' values have the same order of magnitude as the $\overline{v}$ values. $\frac{Cp}{Uo}$ values of 2.0 and 2.4 show rapid increase from 0.02 to 0.32. $\frac{Cp}{Uo} = 1.2$ again shows the lowest values.

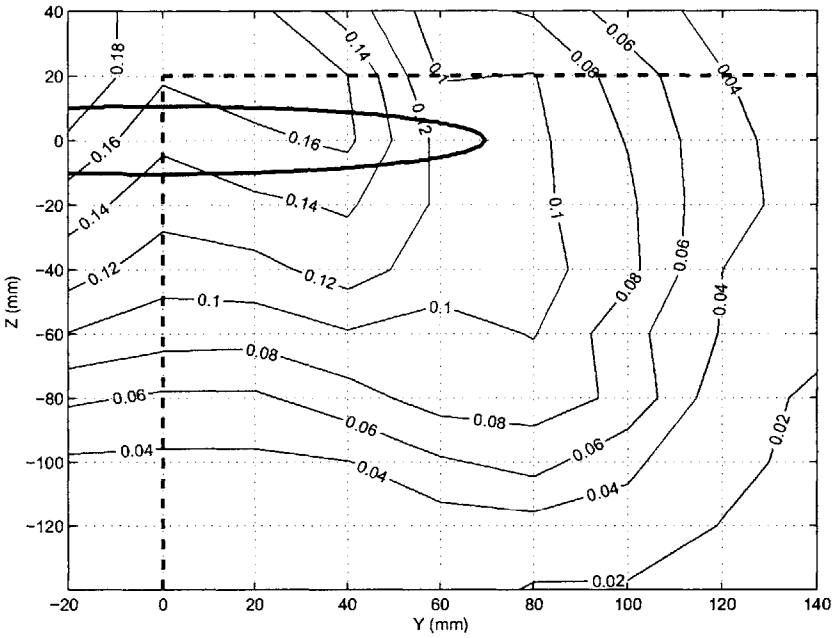

Figure 3-32: v' velocity fluctuations for $\frac{Cp}{Uo}$=0.4

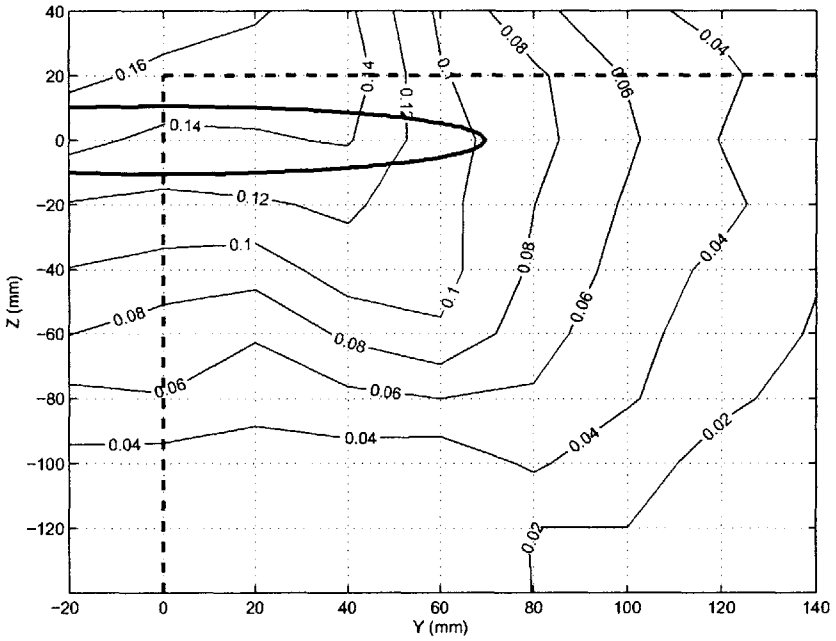

Figure 3-33: v' velocity fluctuations for $\frac{Cp}{Uo}$=0.8

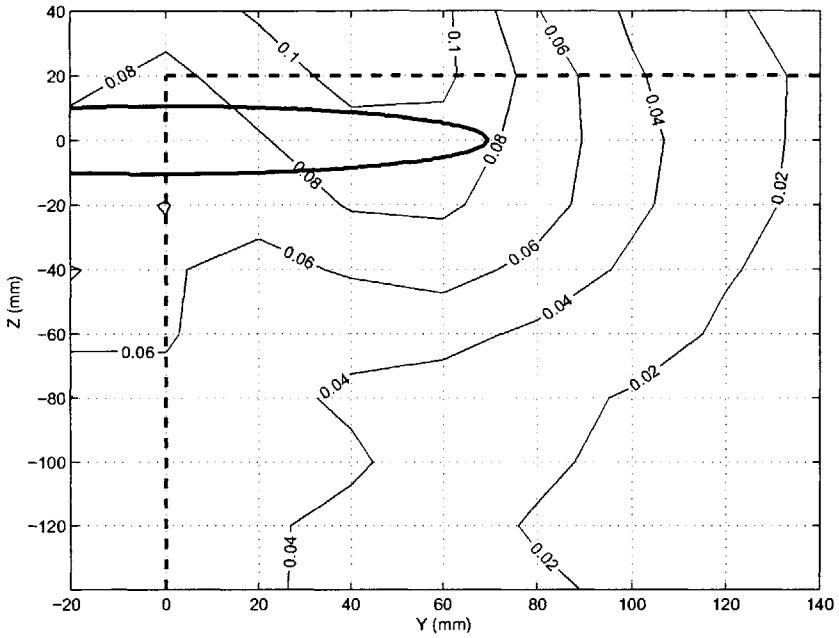

Figure 3-34: v' velocity fluctuations for $\frac{Cp}{Uo}$=1.2

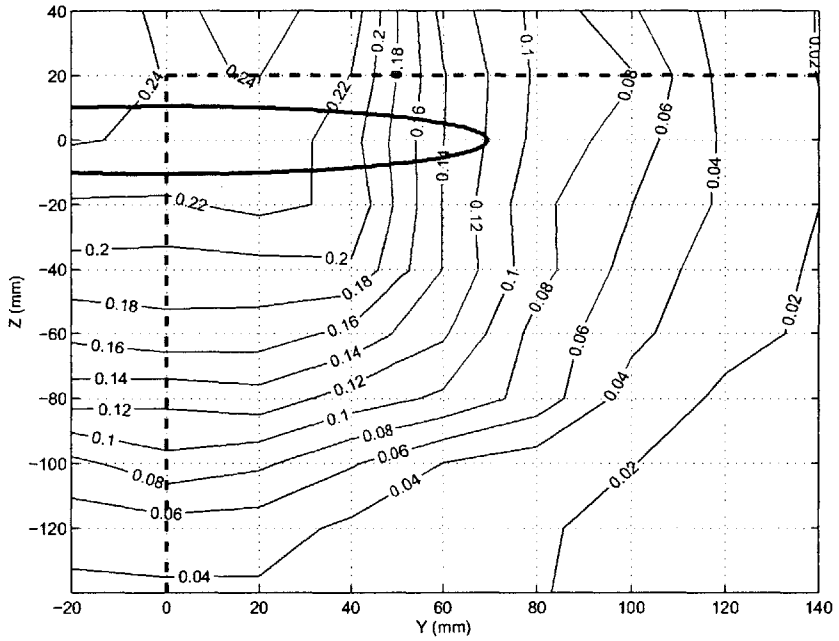

Figure 3-35: v' velocity fluctuations for $\frac{Cp}{Uo}$=1.6

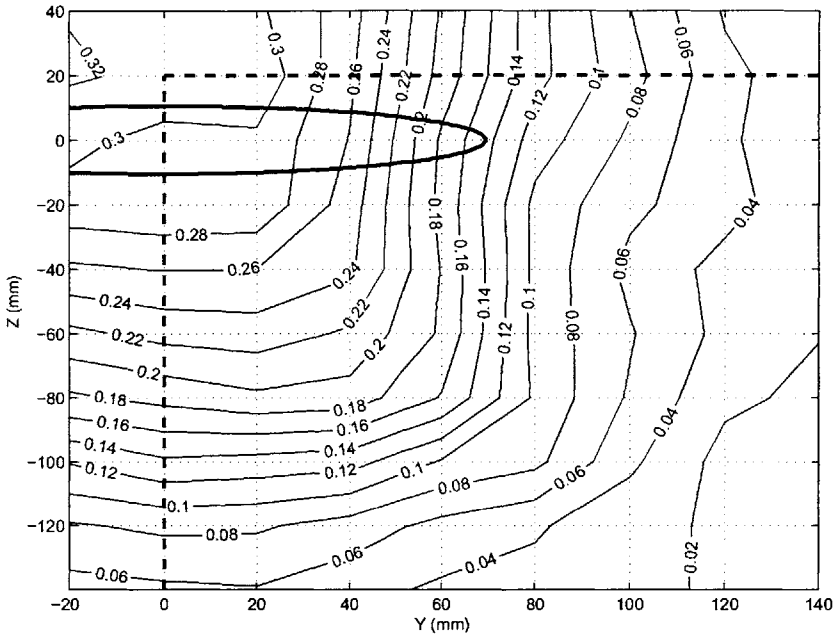

Figure 3-36: v' velocity fluctuations for $\frac{Cp}{Uo}$=2.0

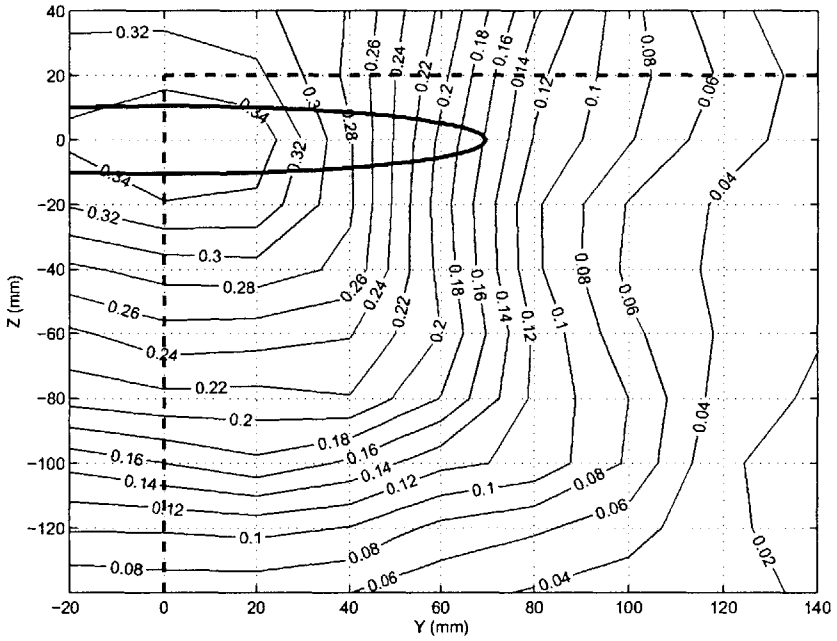

Figure 3-37: v' velocity fluctuations for $\frac{Cp}{Uo}$=2.4

3.5.6 Wake Velocity Total v Component

Figures 3-38 to 3-43 show the total v velocity component. Unlike the total u velocity which shows higher velocities away from the body, the velocity is highest here closest to the body. The $\frac{Cp}{Uo} = 1.2$ case shows the smallest v velocity component.

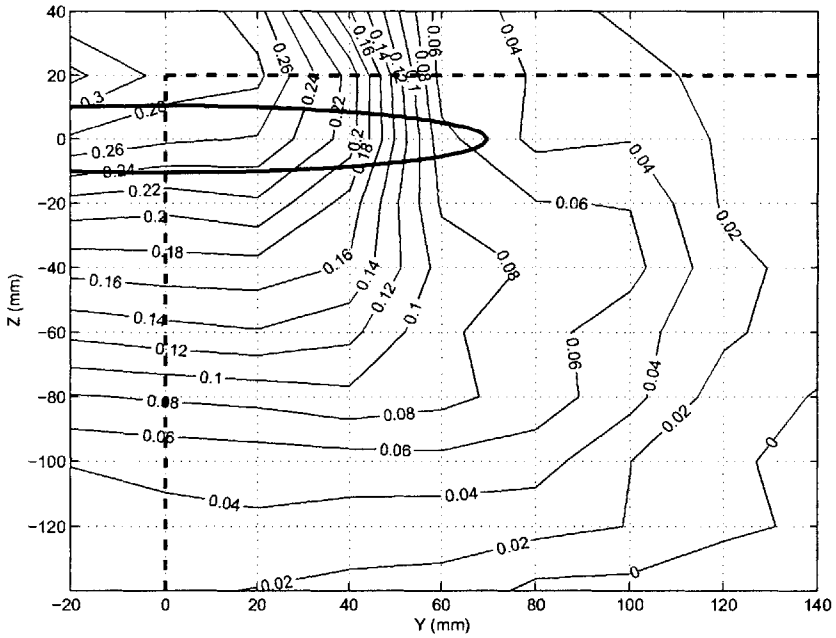

Figure 3-38: v velocity for $\frac{Cp}{Uo}$=0.4

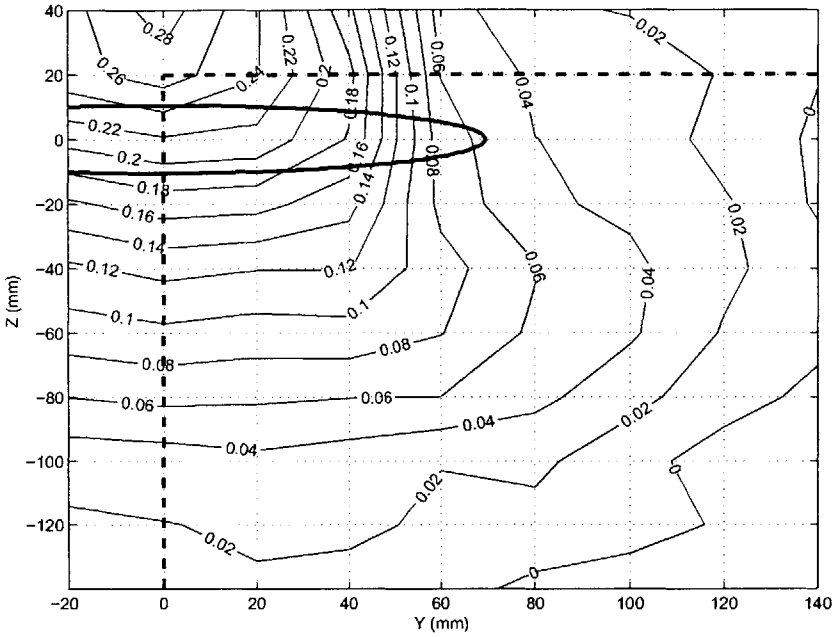

Figure 3-39: v velocity for $\frac{Cp}{Uo}$=0.8

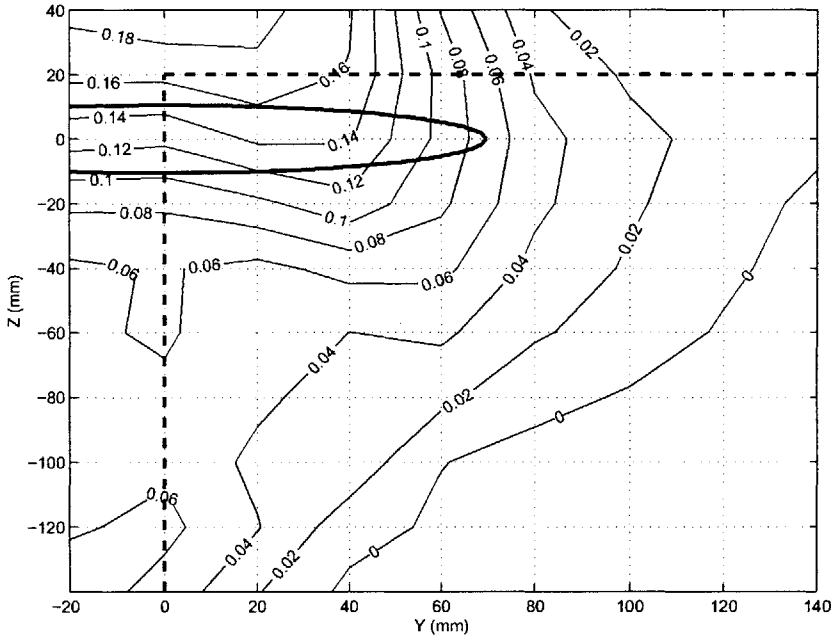

Figure 3-40: v velocity for $\frac{Cp}{Uo}$=1.2

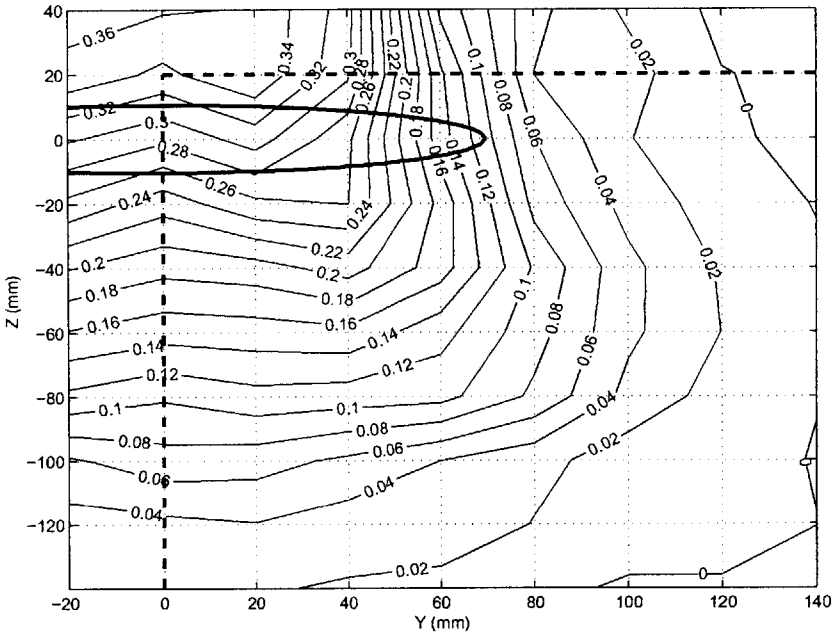

Figure 3-41: v velocity for $\frac{Cp}{Uo}$=1.6

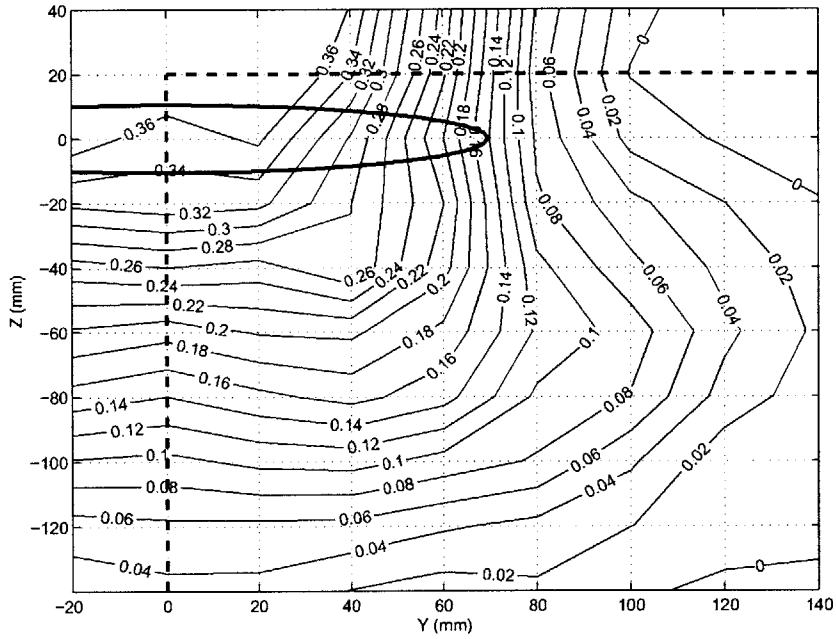

Figure 3-42: v velocity for $\frac{Cp}{Uo}$=2.0

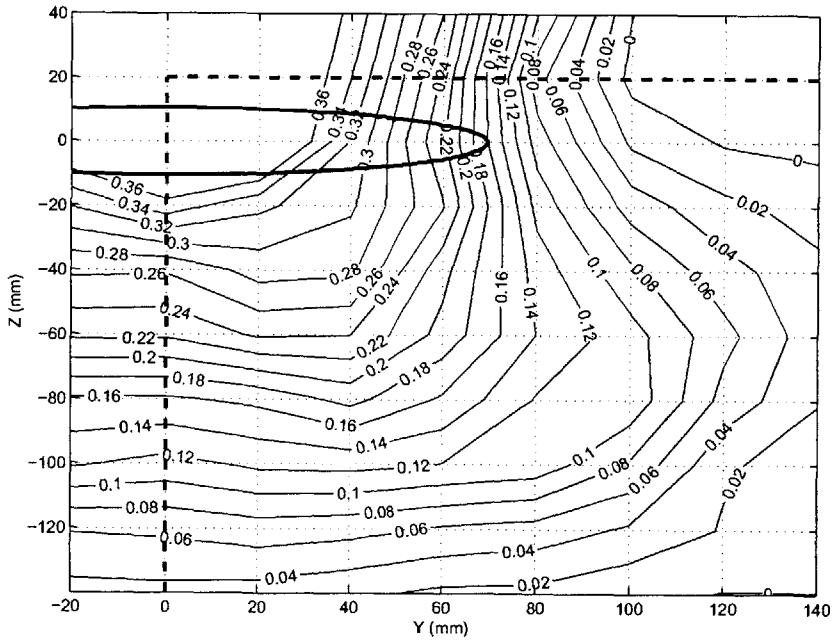

Figure 3-43: v velocity for $\frac{Cp}{U_o}$=2.4

Chapter 4

Pressure Field in the Wake of the Snake

Pressure measurements are taken in order to quantify the wake characteristics of the swimming sea snake. This chapter details the technique used to measure the pressure with kiel probes. It also presents detailed graphs of the wake of the sea snake for several swimming cases.

4.1 Kiel Probe Pressure Measurement Technique

Total or stagnation pressure in the wake was measured by directional pressure sensors called kiel probes. Stagnation pressure is defined as the pressure where the fluid velocity has been reduced to zero [21]. A kiel probe is a modified pitot tube with a shielded tip as shown in figure 4-1. The probe head contains a tube within a duct. The duct directs the local flow into the tube allowing for accurate stagnation pressure measurements without the need for precision alignment of the head. By shielding the probe, the alignment error is significantly reduced. Kiel probes are yaw insensitive making the errors due to turbulence negligible. The kiel probes are also largely pitch insensitive. The United Sensor probes used in these experiments are rated for use with inflow directions between $\pm 54^{\circ}$ of yaw and $\pm 49^{\circ}$ of pitch [1]. The yaw and pitch angles in which the angle of measurement is valid are shown in figure 4-2.

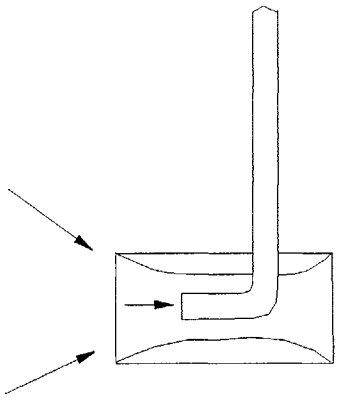

Figure 4-1: Schematic drawing of a kiel probe. The flow direction is shown by the two angled arrows. The kiel probe head guides the flow inside of it so that the stagnation pressure can be measured. [10].

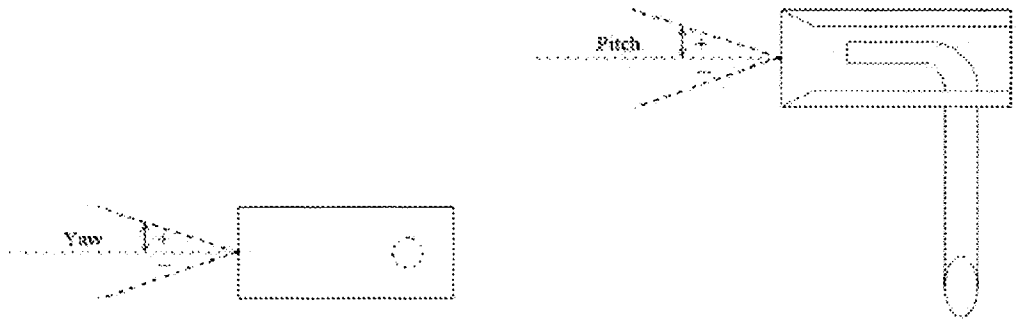

(a) Yaw Angle) **(b) Pitch Angle**

Figure 4-2: Angles of pitch and yaw over which the kiel probes are valid. Figure (a) shows the yaw angle which is valid over $\pm 54°$. Figure (b) shows the pitch angle which is valid over $\pm 49°$.

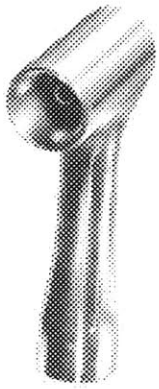

Figure 4-3: Photograph of the kiel probe head. The small inner pitot tube where the pressure measurement is made is seen inside the outer shielding [1].

4.2 Kiel Probe Experimental Set-up

United Sensor KCF-"24" kiel probes made of stainless steel were used for the pressure measurements. These probes have a $\frac{1}{4}$" diameter sensing head 4-3. The probe diameter is $\frac{1}{8}$" and has a length of 24".

Two kiel probes were used to measure a pressure differential. One probe was placed upstream of the snake and the other probe was placed in the wake of the snake. The upstream probe measures the incoming flow which is assumed to be uniform. The wake probe was placed at the same location where the velocity data was obtained by the LDV (figure 4-4).

A mechanical system was designed to allow the probes to be positioned at any Y, Z point in the wake. The X position was set at 108 mm aft of the snake body which is ~0.1L. The kiel probe Y, Z position was controlled by a traverse system with the same coordinate system as described for the LDV system.

CAD drawings of the mechanical system designed to attach the kiel probe to the tunnel are shown in figures 4-5 and 4-6 with the pieces identified. A delrin piece was machined to hold a valve through which the kiel probe passed. The designs show four holes in the delrin piece. This piece was modified for the actual experiment to use only one hole. The delrin piece fit between two aluminum brackets which were mounted onto a polycarbonate window that fit the front side of the tunnel. The

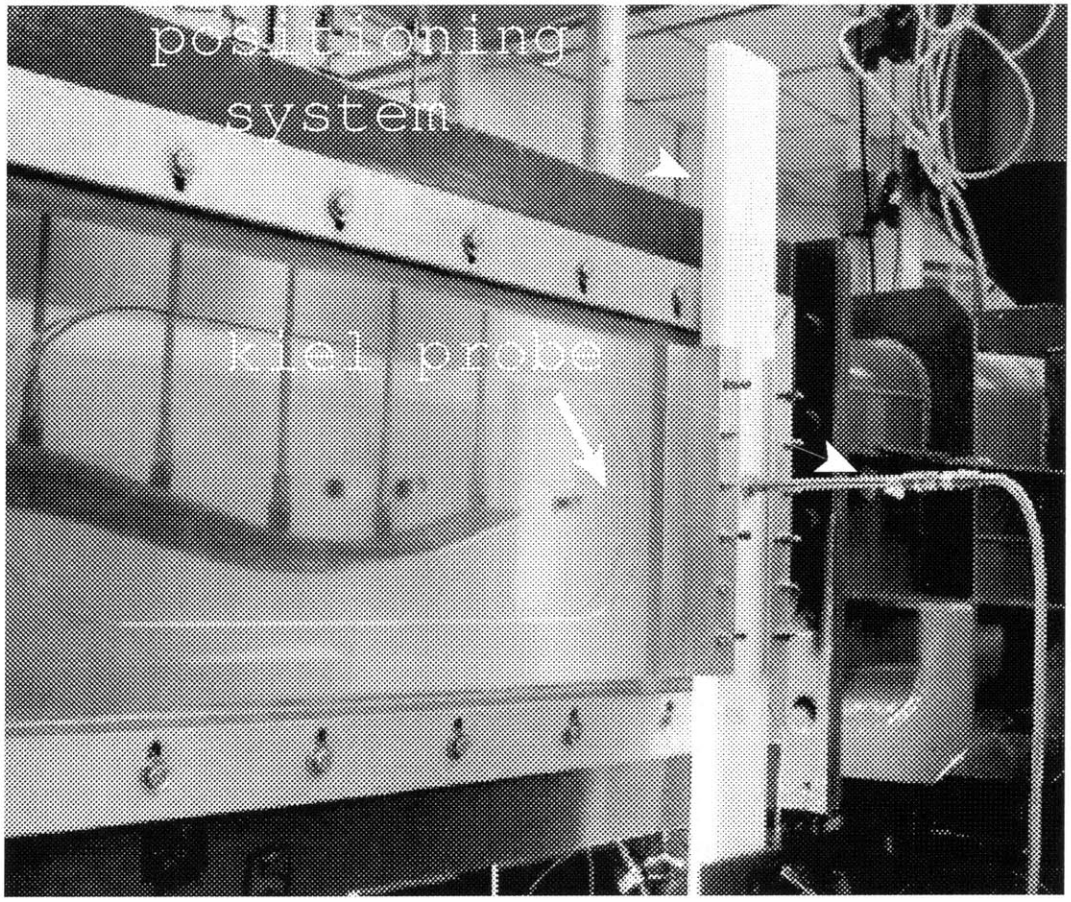

Figure 4-4: Photograph showing the experimental set-up of the kiel probe in the wake. The positioning system allows the probe to move up and down and in and out of the tunnel. The kiel probe positioning is controlled by a traverse system.

brackets were bolted onto the plate and when loosened, the delrin piece could slide up and down. The window was specially machined to have a slot in which the probe could slide. An o-ring sealed the delrin piece to the window to prevent leakage.

Electronic strain-gauge type pressure transducers, manufactured by Sensotec and connected to strain gauge conditioners, were used for the pressure measurements. A Krohn-Hite Model 3384 Filter decreased the noise from the measurements. The filter cutoff frequency was set to 30 hz, the input gain was set at 50 db, and the output gain was set at 10 db. The filter was a low pass Butterworth filter. The filtered signal went into a 12 bit computer data acquisition board and was saved for later processing.

The pressure transducers were calibrated with a water manometer system. This system uses a known amount of water for the calibration. A tube is connected from each side of the pressure gauge to the manometer. Water on one side of the manometer is pumped to a height above that of the other side and the height difference is measured. This known height is then used in equation 4.1:

$$\Delta p = \rho g \Delta H \tag{4.1}$$

where g is gravity and ρ is the density of water. The resulting Δp is the pressure that was applied. The uncertainty in this pressure measurement is dependent on the accuracy of the water column height. The details of the calibration are outlined in Batcheller and Kimball [4].

Surveys of wake pressure were carried out for $\frac{Cp}{Uo}$ = [0.4, 0.8, 1.2, 1.6, 2.0, and 2.4]. Each survey involved 195 physical locations (a 13 x 15 grid) in the wake. This grid covers an area spanning 240 mm in the Y direction and 280 mm in the Z direction. The pressure plots were made in the area of Y = -100 mm to 140 mm and Z = -140 mm to 140 mm and measurements were taken every 20 mm. At each point, data was recorded for at least 30 oscillations of the snake to obtain mean wake pressure.

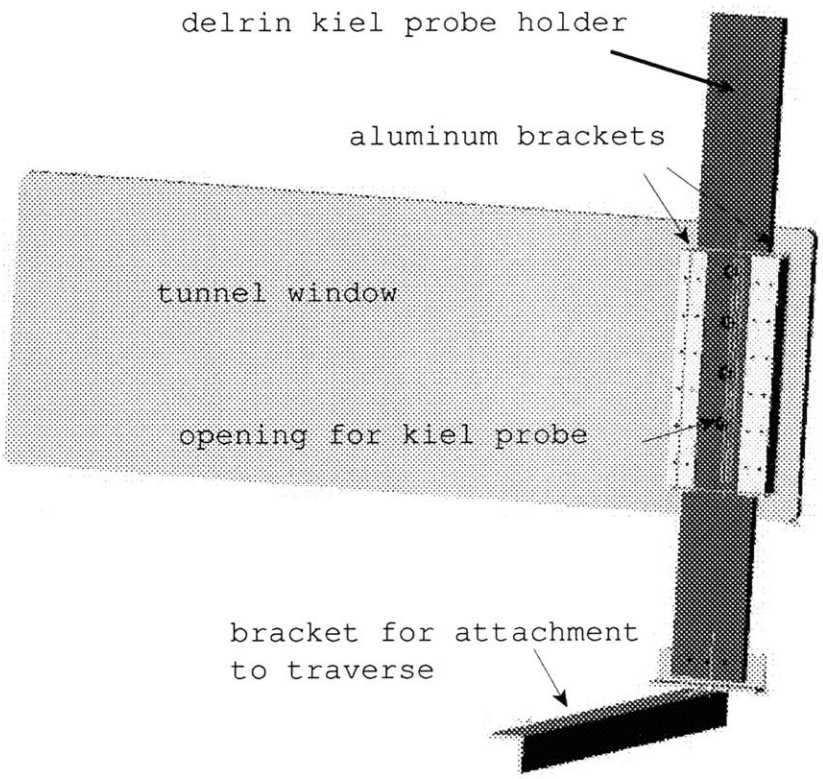

Figure 4-5: CAD drawing of the front of the kiel probe movement system. This view shows how the pieces attach to the front of a specially modified tunnel window. The delrin piece holds the kiel probe and slides in the Z direction for positioning of the probe. Aluminum brackets attach the delrin to the specially modified tunnel window. A bracket is used to attach the system to the traverse.

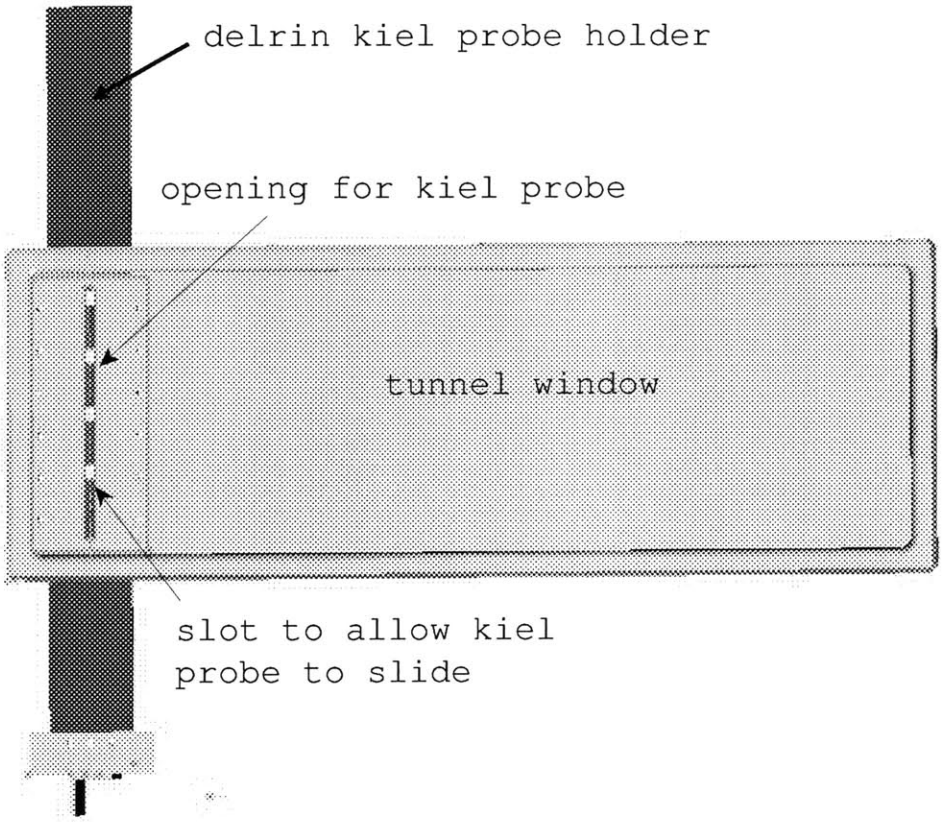

Figure 4-6: CAD drawing of the back of the kiel probe movement system. This view is looking out at the window from the inside of the tunnel. The window was specially designed with a slot to allow the kiel probe to move in the Y and Z directions.

4.3 Initial Kiel Probe Wake Cut

In order to preliminarily determine the distance across the tunnel where pressure differences are seen, an initial pressure cut was taken at ~0.1L aft of the snake tail. The cut was made in the Y direction with very coarse spacing without the use of the traverse system for accuracy. The results are shown in figure 4-7. In this plot, the center of the snake is at Y=0. This data shows a symmetry of pressure behind the snake with some skewness. The imprecision introduced from not using the traverse introduced error which may account for some of the skewness. However, results shown later also show this skewness. Therefore, the tunnel inflow may not be perfectly uniform.

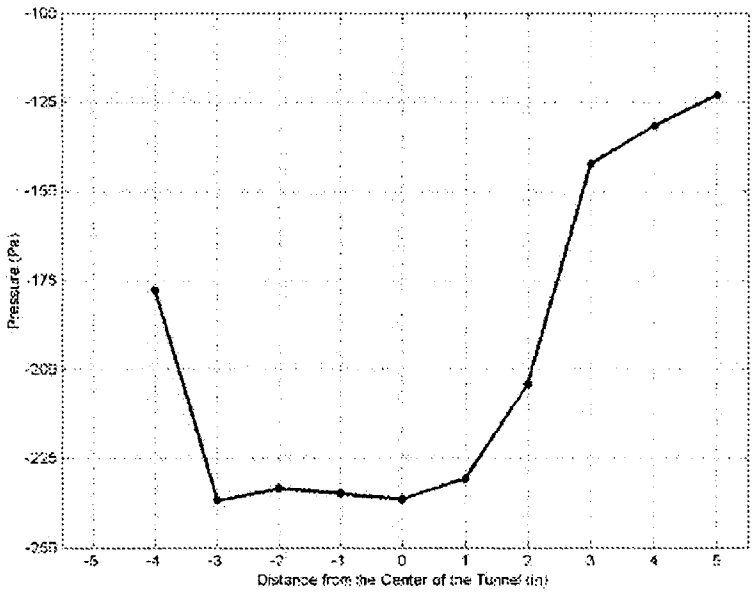

Figure 4-7: Initial kiel probe wake cut. The plot shows the pressure at different distances away from the tunnel center. This preliminary test did not use the traverse for accurate positioning.

4.4 Pressure Wake Profiles

The results of the pressure wake cuts made with the kiel probes in the Y-Z plane are shown in figures 4-8 to 4-21 for $\frac{Cp}{Uo}$ values of 0.4, 0.8, 1.2, 1.6, 2.0, and 2.4. For each $\frac{Cp}{Uo}$ value, two plots are shown. The first plot contains the raw data and the second plot contains the normalized data. The pressure differential far from the snake should be zero and therefore to account for any drift in the sensors or air bubbles in the lines, the data was normalized. The pressure data was normalized by averaging Y= -20 mm to 140 mm at Z= -140 mm. The average of this area was then set to be zero and all points were normalized using an offset. The mean position of the snake tail is shown in both plots.

As previously discussed in section 3.5, the coordinate system used is based off the (X,Y,Z) = (0,0,0) position set at the center point of the tip of the tail when the snake is set at its mean position. X is defined as the coordinate lateral to the snake body. The coordinate system used is shown in figure 2-8. The tail's motion is present during some part of its cycle in the region from -64 mm to 64 mm.

For all of the runs, apart from the disturbance by the pistons, some symmetry is seen for the top and bottom halves of the profile. In addition, a right-left symmetry is present in the pressure plots. This symmetry shows some skewness at the top which may be due to the probes drifting or to the tunnel inflow not being completely uniform. In order to further study the entire wake without including the influence of the pistons, an area representing a quarter of the wake was identified using the top-bottom and right-left symmetry. This area has been marked by a dashed line in each plot and is the same area identified in the velocity plots in chapter 3. The pressure and velocity plots show similar structures developing in the wake.

The influence of the piston rods that drive the snake is apparent in each profile indicated by the low pressure region in the top center of each figure. Below the snake, this low pressure area is not present. This suggests that the wake pressure profile below the snake well represents half of the wake. It should be noted that when the snake is at its lower range, the piston rods enter some of the area below the dashed

line. Therefore some effect of the pistons occurs below the mean position of the snake.

For $\frac{Cp}{Uo} = 0.4$ and 0.8 (figures 4-8 to 4-9) the pressure profiles show very similar characteristics. The plots are right-left symmetric. A constant increase in pressure occurs as distance from the tail increases. The contour lines show a well-defined concentric shape. Each contour shows little variation from the concentric shape.

Figures 4-12 and 4-13 show the wake survey for $\frac{Cp}{Uo} = 1.2$. The contour lines now show more variation. The lines are no longer constant and instead have indentations. The center of the contour lines below the snake shows a downwards peak developing with additional downward peaks under each tip on the tail.

Figures 4-14 and 4-15 show the wake survey for $\frac{Cp}{Uo} = 1.6$. The central peak region below the snake exists again and is more well-defined in these plots. The contours also increase in pressure values more rapidly away from the snake tail. The effect of the tail appears to extend all of the way to the bottom of the figure.

Two runs were made for $\frac{Cp}{Uo} = 2.0$ (figures 4-16 to 4-19). They show similar general structures with a prominent central peak that extends down significantly. To the right and left of the central peak, two areas of positive pressure appear. Run two shows substantially less defined features. Figures 4-16 and 4-19 show circular regions on the right and left sides of the mean position of the tail. These are areas of low pressure.

The result of the $\frac{Cp}{Uo} = 2.4$ run is shown in figures 4-20 and 4-21 . The central peak is prominent and extends to the base of the plot suggesting that the tail is influencing flow all the way to the bottom of the tunnel. On each side of the central peak, positive pressure regions exist. At each tip of the snake, a prominent low pressure region is again present. $\frac{Cp}{Uo}$ of 2.4 shows the most structured and complex pressure profile; yet, it is similar to the profiles shown for $\frac{Cp}{Uo} = 2.0$.

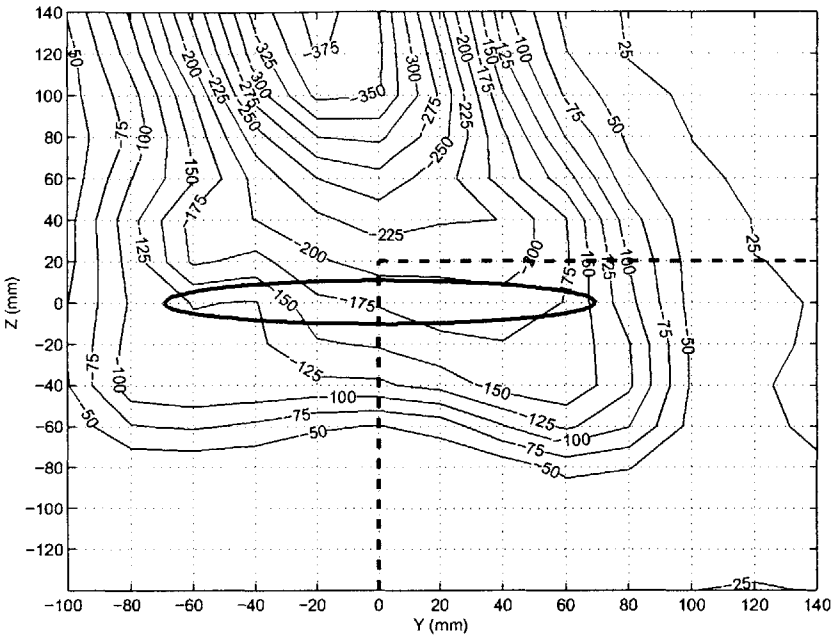

Figure 4-8: Wake pressure profile for $\frac{Cp}{Uo} = 0.4$

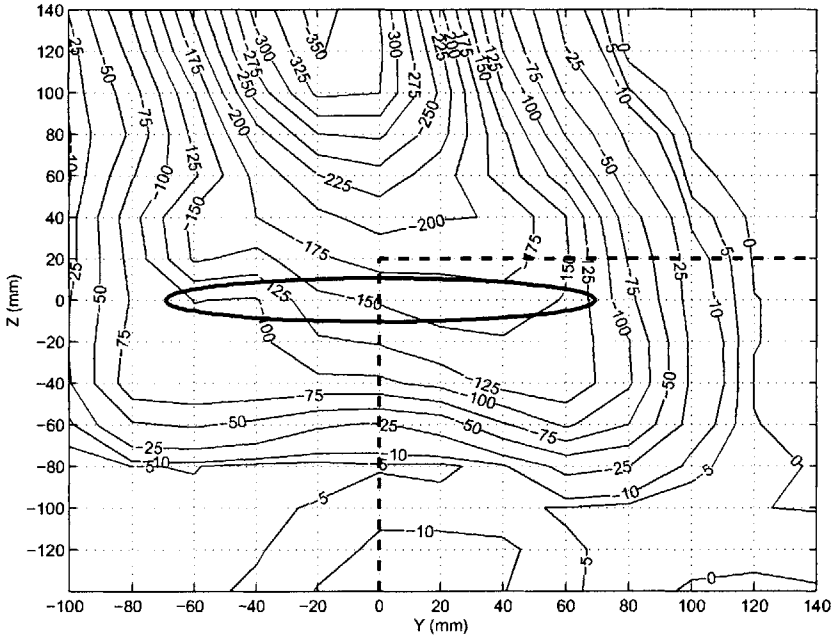

Figure 4-9: Normalized wake pressure profile for $\frac{Cp}{Uo} = 0.4$

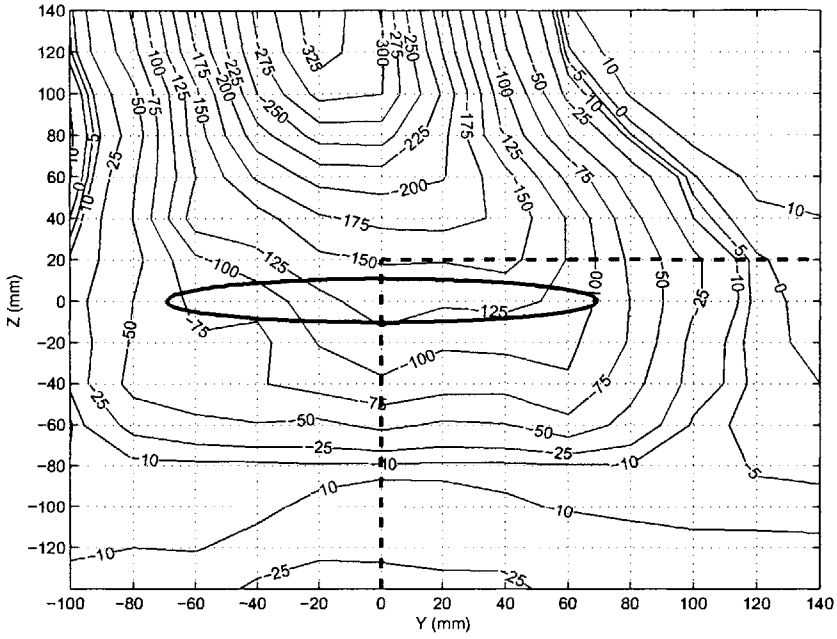

Figure 4-10: Wake pressure profile for $\frac{Cp}{Uo} = 0.8$

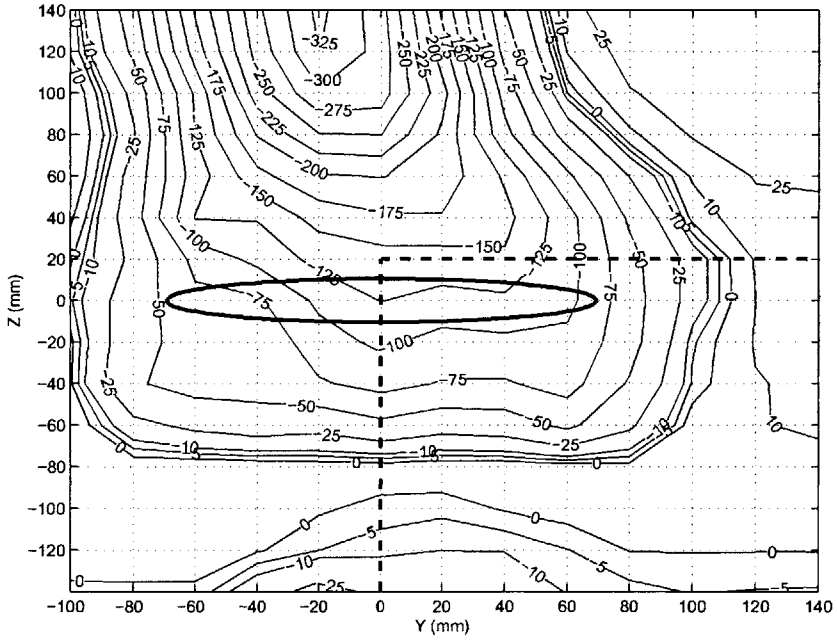

Figure 4-11: Normalized wake pressure profile for $\frac{Cp}{Uo} = 0.8$

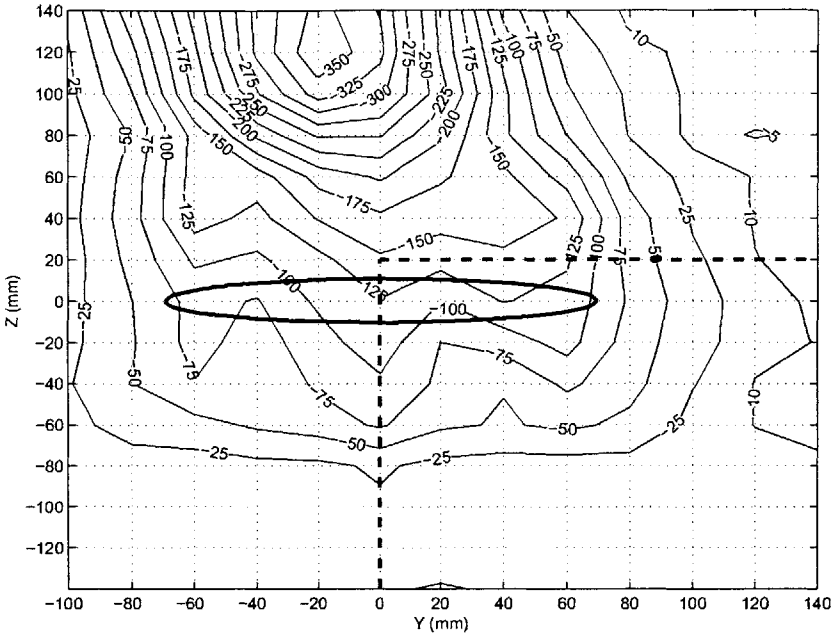

Figure 4-12: Wake pressure profile for $\frac{Cp}{Uo} = 1.2$

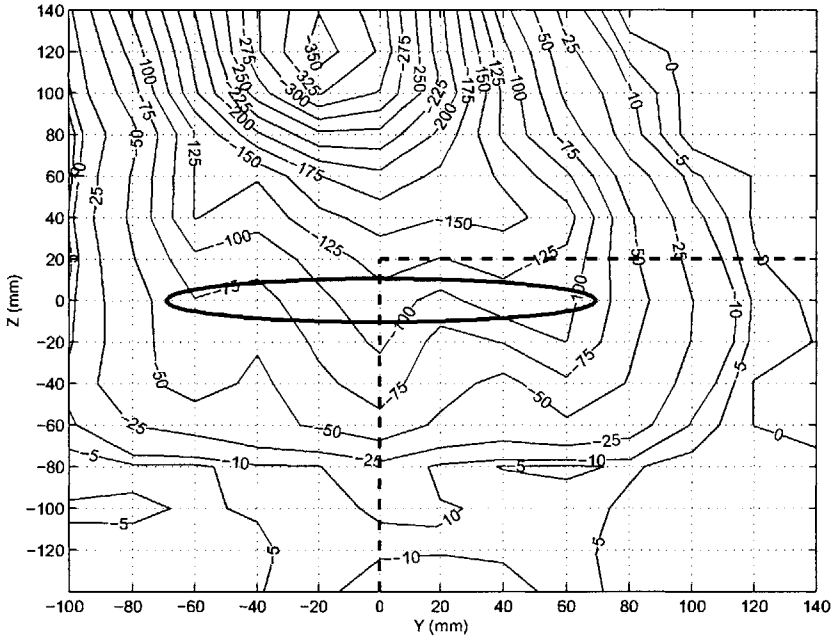

Figure 4-13: Normalized wake pressure profile for $\frac{Cp}{Uo} = 1.2$

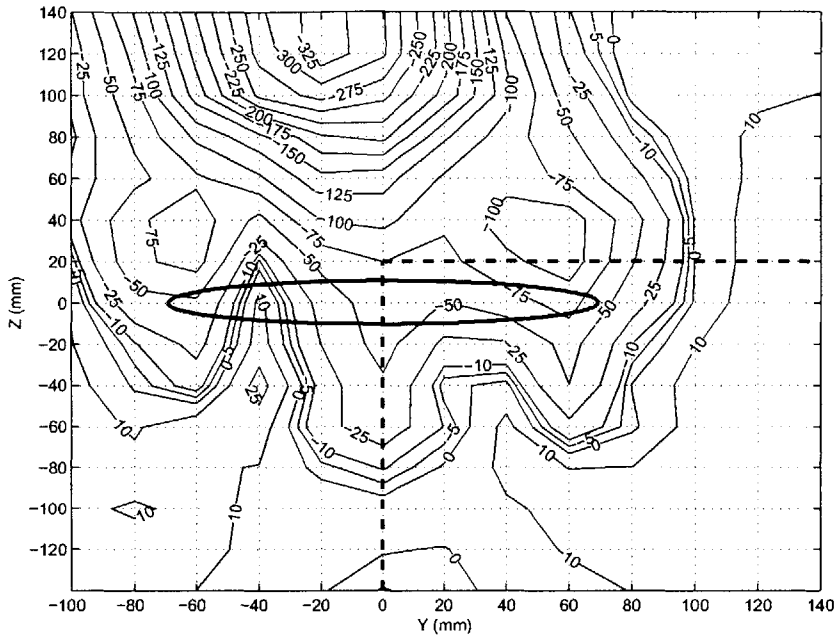

Figure 4-14: Wake pressure profile for $\frac{Cp}{Uo} = 1.6$

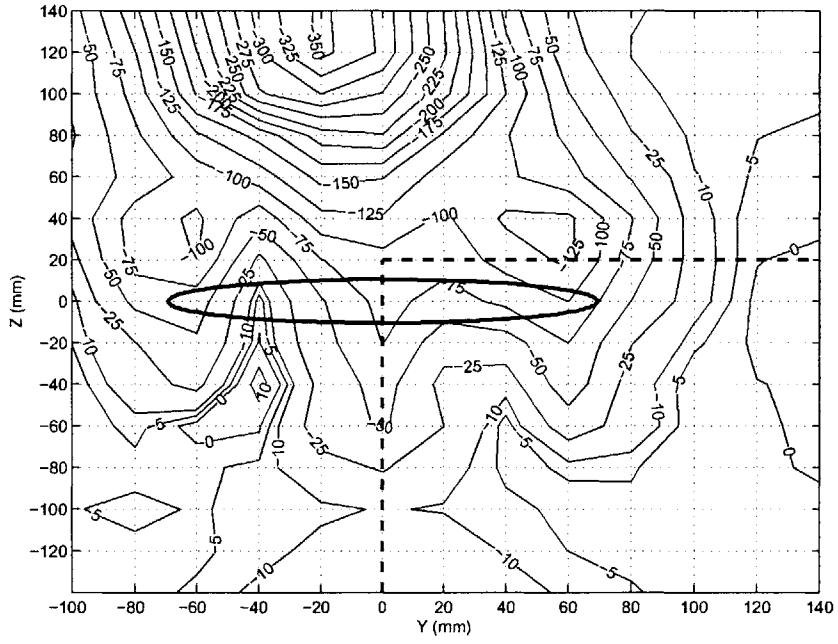

Figure 4-15: Normalized wake pressure profile for $\frac{Cp}{Uo} = 1.6$

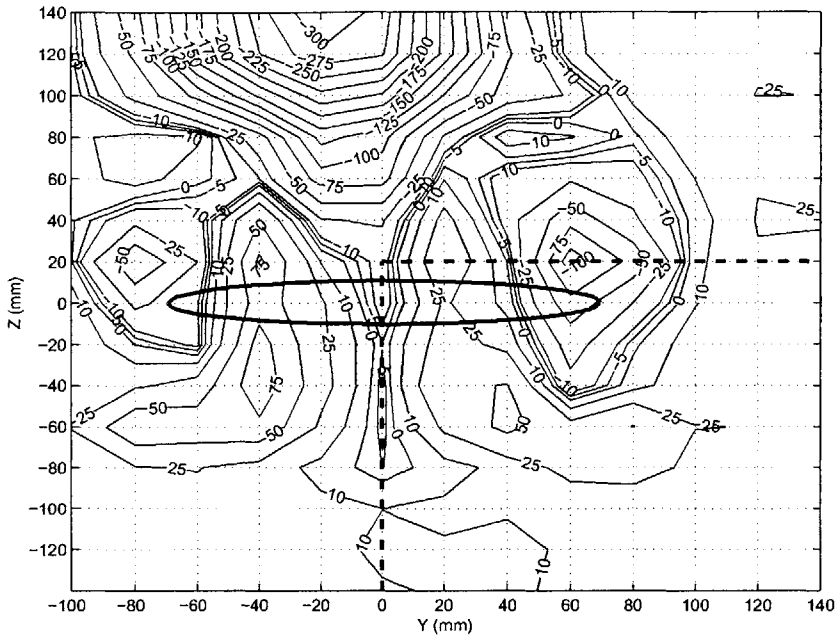

Figure 4-16: Wake pressure profile for $\frac{Cp}{Uo} = 2.0$, Run 1

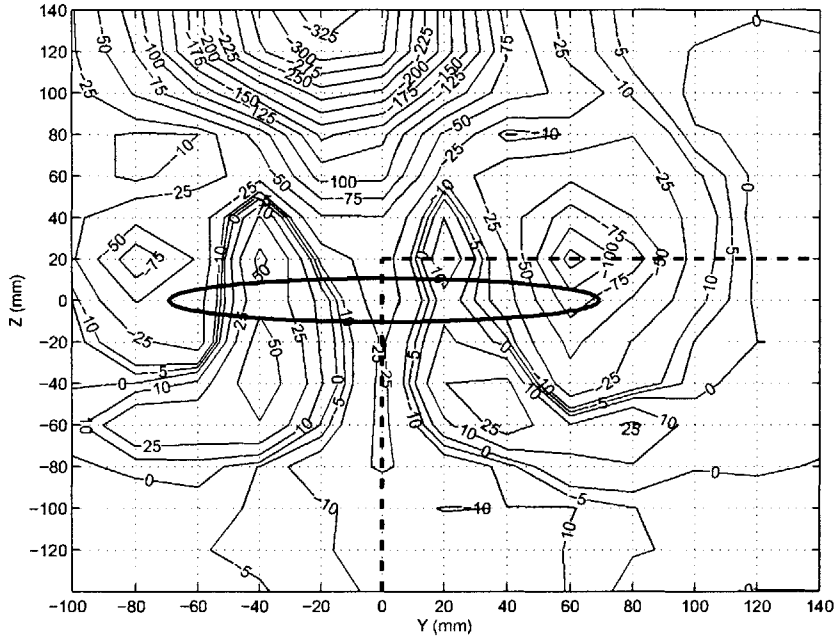

Figure 4-17: Normalized wake pressure profile for $\frac{Cp}{Uo} = 2.0$, Run 1

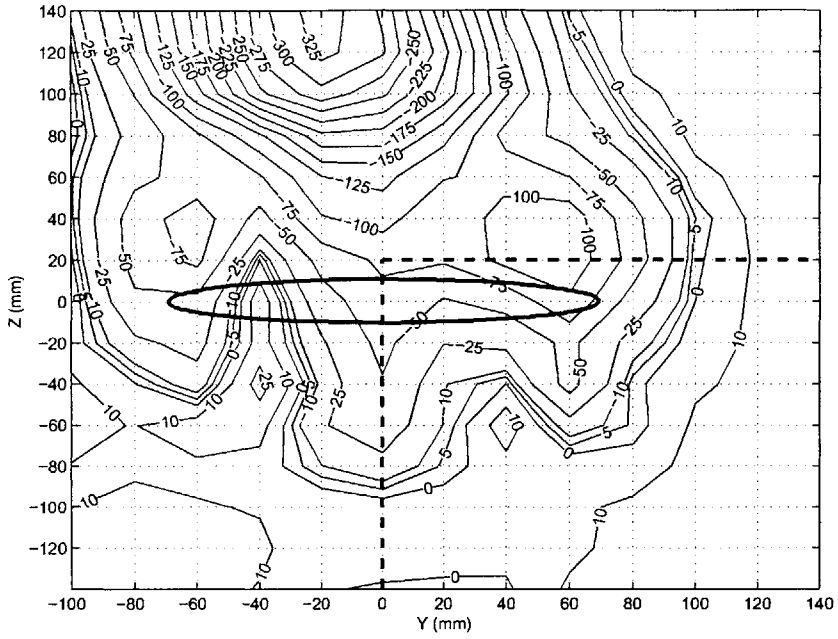

Figure 4-18: Wake pressure profile for $\frac{Cp}{Uo} = 2.0$, Run 2

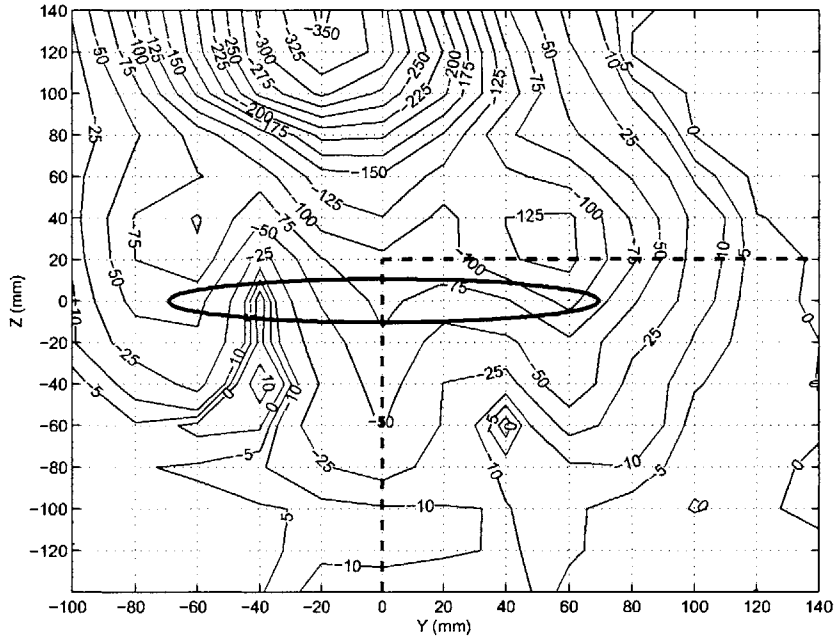

Figure 4-19: Normalized wake pressure profile for $\frac{Cp}{Uo} = 2.0$, Run 2

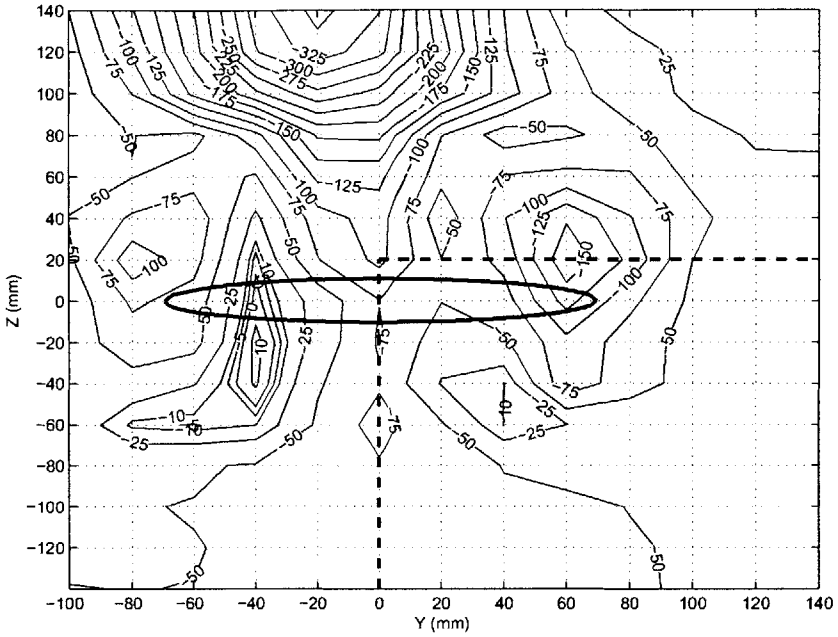

Figure 4-20: Wake pressure profile for $\frac{Cp}{Uo} = 2.4$

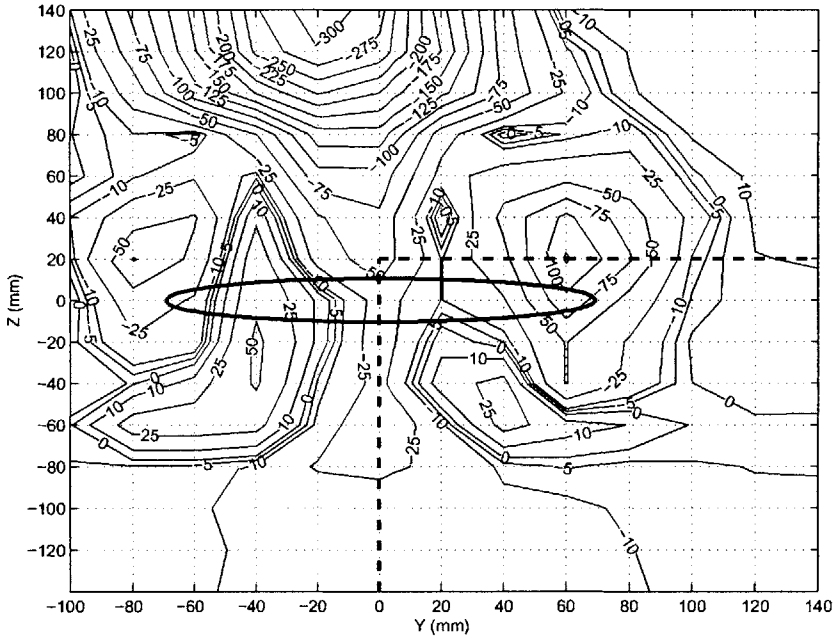

Figure 4-21: Normalized wake pressure profile for $\frac{Cp}{Uo} = 2.4$

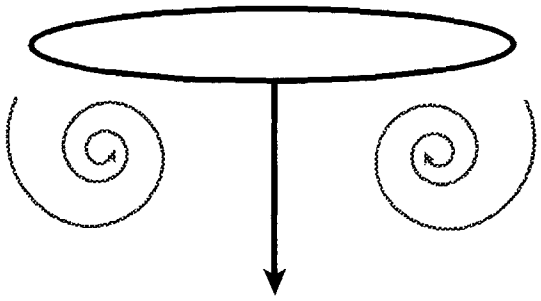

Figure 4-22: Schematic drawing of the flow under the snake. This flow is suggested by the pressure and velocity profiles. When the center of the tail moves downwards, as indicated by the arrow, fluid is pushed downwards and vortices are formed.

The shapes of these plots suggest that the snake is pushing the fluid down. When the fluid is forced down the center the peak develops along with indentations on each side. The central rib aids in pushing the fluid down and the thinner sides contribute to flow around the sides. Figure 4-22 shows an illustration of the type of flow that this suggests is taking place below the snake.

Chapter 5

Thrust Production in the Wake of the Swimming Snake Model

A primary interest in this thesis is the measurement of the thrust produced by a swimming sea snake by combining pressure and velocity measurements and through a conservation of momentum approach. This chapter presents the theory behind such calculations and the results obtained for the swimming snake. A theoretical derivation for thrust by Lighthill is examined and compared with the experimental results obtained.

5.1 Momentum Balance Approach to the Calculation of Thrust

Conservation of mass applied to the tunnel control volume requires that the mass flux into the test section is equal to the mass flux out of the test section. No mass is lost out of the sides of the tunnels. A momentum balance was completed for the water tunnel with the boundaries of the test section of the tunnel and the snake body as the sides of the control volume as shown in figure 5-1. The snake body is therefore excluded from the control volume. The entrance area is the cross-sectional area of the tunnel, fore of the snake and the exit area is the cross-sectional

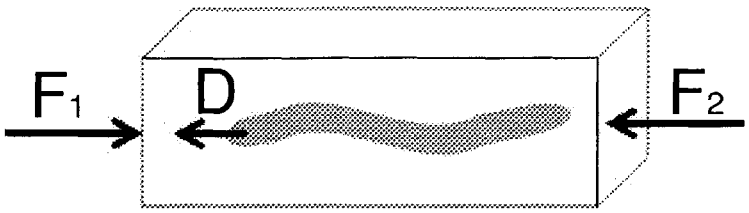

Figure 5-1: Illustration of the forces acting on the fluid in a control volume. The snake exerts a drag force, D, and a pressure force exists at both the entrance to the control volume, F_1, and at the exit, F_2.

area aft of the snake. The forces acting on the fluid are shown. A drag force is created by the snake body and is represented by D in figure 5-1. The drag force is equal to:

$$\vec{D} = \iint_s (\vec{\sigma} + \vec{\tau}) dA \tag{5.1}$$

where S is the surface of the snake body, $\vec{\sigma}$ is the stress in the normal direction, and $\vec{\tau}$ is the shear stress. At the entrance and exit areas, the force on the area includes a shear stress, $\vec{\tau}$, and a stress in the normal direction, $\vec{\sigma}$. It is assumed that at the entrance and exit of the control volume the shear stresses are negligible, hence, $\vec{\tau} \sim$ 0 and $\vec{\sigma} \sim$-p$\hat{n}$.

Therefore the forces at the entrance and exit become:

$$\vec{F_1} = \int_A p_1 \hat{n} dA \tag{5.2}$$

$$\vec{F_2} = -\int_A p_2 \hat{n} dA \tag{5.3}$$

where $A_{inflow} = A_{outflow} = A$.

The three forces acting on the fluid are summed to create the total force. The force applied on the exit area and the drag force are opposite in sign to the force

applied on the entrance of the control volume.

$$\begin{aligned}\sum \vec{F} &= \vec{F_1} + \vec{F_2} - \vec{D} \\ &= \int p_1 \hat{n} dA - \int p_2 \hat{n} dA - \vec{D} \end{aligned} \tag{5.4}$$

The momentum theorem states that the rate of increase of momentum in a control volume (cv) plus the momentum flux out of the control surface (cs) is equal to the sum of the forces acting on the volume. This is expressed mathematically:

$$\sum \vec{F} = \iiint_{cv} \frac{\partial \rho \vec{u}}{\partial t} d\forall + \iint_{cs} \rho \vec{u} (\vec{u} \cdot \vec{n}) dA \tag{5.5}$$

where F is force, ρ is density, $\forall$ is volume, A is area, and u is velocity. For periodic flow, averaging over one period harmonic terms results in a zero mean; therefore, the second term of equation 5.5 can be assumed to be zero. The conservation of momentum equation then is reduced to:

$$\overline{\sum \vec{F}} = \overline{\iint_{cs} \rho \vec{u} (\vec{u} \cdot \vec{n}) dA} \tag{5.6}$$

By taking the x-component of equation 5.6, we find

$$\overline{\sum F_x} = \overline{\iint_{cs_{out}} \rho u_{out}^2 dA} - \overline{\iint_{cs_{in}} \rho u_{in}^2 dA} \tag{5.7}$$

The forces acting on the fluid (equation 5.4) and the momentum flux (equation 5.7) are now equated:

$$\overline{\int_A p_1 dA} - \overline{\int_A p_2 dA} - \overline{D_x} = \overline{\iint_{cs_{out}} \rho u_{out}^2 dA} - \overline{\iint_{cs_{in}} \rho u_{in}^2 dA} \tag{5.8}$$

which can be rewritten as:

$$\begin{aligned} -\overline{D}_x &= \overline{\iint_{cs} \rho \Delta u^2 dA} + \overline{\int_A \Delta p dA} \\ &= \overline{\iint_{cs} (\rho \Delta u^2 + \Delta p) dA} \end{aligned} \tag{5.9}$$

where Δ(x) means the difference in the quantity x between out and in of the control surface.

If we define the thrust force as:

$$-\overline{D}_x = T \tag{5.10}$$

equation 5.9 becomes:

$$T = \overline{\iint_{cs} (\rho \Delta u^2 + \Delta p) dA} \tag{5.11}$$

5.2 Simplified Thrust Calculation

p is the static pressure and can be related to the stagnation or total pressure, $\hat{P}$, which is the pressure measured by the kiel probes in this experiment, by equation 5.12:

$$p = \hat{P} - \frac{1}{2}\rho q^2 \tag{5.12}$$

which when substituted into equation 5.11 results in the final equation for thrust:

$$T = \overline{\iint_{cs} \Delta(\hat{P} - \frac{1}{2}\rho q^2 + \rho u^2) dA} \tag{5.13}$$

Figure 5-2 shows the three-dimensional vortex flow and the jet it produces in the wake of a fish [20]. The tail of the snake acts the same as the tail of a fish; therefore, it is suggested that the wake produced would be like that shown in this figure. In the water tunnel, the snake is oriented with the tail motion occurring in the z direction; therefore, the wake of the snake model would actually be oriented 90 degrees from the wake shown. The wake in figure 5-2 shows dorsal and ventral tip vortices generated by the tail during the tail beat. In addition, vertical vortices are created at the trailing edge of the fish tail during each half-stroke. These vortices create a chain pattern. Within this chain, a jet of water undulates in the opposite direction to the swimming motion. For the snake, the vertical vortices would be rotating about the tunnel's y axis.

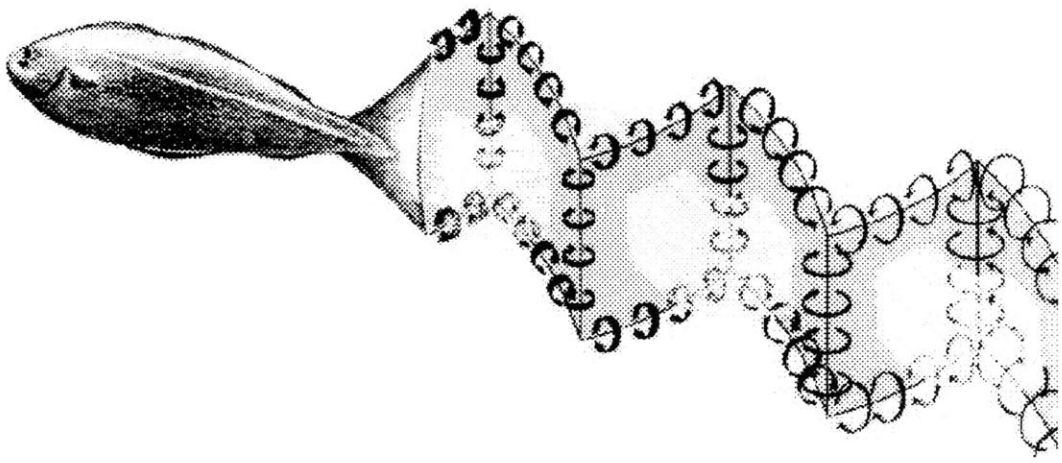

Figure 5-2: Vortex and jet production in the wake of a fish. The three-dimensional vortices shed by the tail are shown. The jet of water that undulates opposite to the swimming motion is seen between each vertical column of vortices [20].

A control volume approach allows an area in the wake to be selected that does not appear to have significant contributions from the pistons. The actual snake without the piston rods is axisymmetric about both the x and z planes. Therefore, if the piston rods were not present, it would be expected that each quadrant would be identical in features. The top half of the wake would be the mirror image of the bottom, and likewise the right half would be the mirror image of the left half. The area chosen for the thrust calculation represents one-quarter of the wake, and was represented in the wake velocity and pressure plots by the dashed line. The total thrust is then the thrust calculated in this one quarter multiplied by four. Use of the quarter wake area is also essential as system limitations with both the LDV and kiel probes made it impossible to collect data in the entire Y direction of the tunnel. The LDV data could not be collected much past the centerline of the tunnel due to a low data collection rate when the beam becomes attenuated from traveling such a distance. The kiel probes were also not long enough to reach all of the way through the tunnel. Equation 5.11 was applied to each gridded point in the quarter quadrant and the resulting values were summed and multiplied by four to get the final thrust values. The results of this calculation are shown in section 5.3.

The thrust calculation was applied first using a simplified approach and then an

improved one. For the simplified case, the approximation that q≅u is made. This reduces equation 5.13 to:

$$T = \iint_A \Delta(\hat{P} + \frac{1}{2}\rho u^2)dA \tag{5.14}$$

For the improved case:

$$q = |u, v, w| \tag{5.15}$$

therefore,

$$q^2 = u^2 + v^2 + w^2 \tag{5.16}$$

Each local velocity can be further broken down into its individual components, the mean velocity, and the fluctuations, which results in equation 5.17. All terms not shown are zero.

$$\overline{q^2} = \overline{u}^2 + \overline{v}^2 + \overline{w}^2 + \overline{u'^2} + \overline{v'^2} + \overline{w'^2} \tag{5.17}$$

The data obtained from the LDV gives results for both the u and v components. The $\overline{w}^2$ is unknown and it is assumed that this term is insignificant. The ventral and dorsal vortices have their significant fluctuations in the w component as these vortices rotate about the x axis at the tips of the tail as seen in figure 5-2. When they are shed, the rms of the w component will be significant. Since the LDV data does not provide data for the w component, the assumption can be made that $\overline{w'^2} \simeq \overline{u'^2}$. Using the above assumptions, equation 5.17 can be reduced to:

$$\overline{q^2} = \overline{u}^2 + \overline{v}^2 + +2\overline{u'^2} + \overline{v'^2} \tag{5.18}$$

As a result the equation for thrust becomes

$$T = \iint \overline{\Delta\hat{P}} + \frac{1}{2}\rho(\overline{u}^2 - U_o^2 - \overline{v}^2 - \overline{v'^2})dA \tag{5.19}$$

For each $\frac{Cp}{Uo}$ value tested, a wake profile was created and the total thrust summed.

5.3 Results of Thrust Calculation

Using the improved case calculation, profiles of the thrust production in the wake were created and are shown in figures 5-3 to 5-9. The velocity and pressure data was taken at distinct points in the wake that creates a grid. The thrust can thus be calculated at each point with the area of each grid element, taken to be 0.0004 cm^2, a square area around each point.The normalized pressure was used in the calculations. The tail is drawn in its mean position.

When $\frac{Cp}{Uo} = 0.4$, the thrust profile is complex. Large areas of negative thrust are seen and an elliptical region appears to the right of the tail. For $\frac{Cp}{Uo} = 0.8$ and 1.2, the profiles are very similar. Each plot shows the most negative region closest to the tail and a gradual increase in value further from the snake. The wake shows a concentric shape around the tail. $\frac{Cp}{Uo} = 1.6$ shows a concentric shape but with a curved region developing under the tail. $\frac{Cp}{Uo} = 2.0$ is shown for two runs. Each plot uses the same LDV data but different kiel probe data. The profiles are similar with a dip in the contour lines occurring at the right edge of the snake. The first run shows a region below the snake of positive thrust. A similar, but less developed region exists for run two. $\frac{Cp}{Uo} = 2.4$ shows a similar wake profile to $\frac{Cp}{Uo} = 2.0$ with a positive thrust formation below the snake. These plots appear to fall into three different modes of wake development. The first mode is characterized by the wake of $\frac{Cp}{Uo} = 0.4$. The wake is highly complex and is a drag wake. The second mode appears for $\frac{Cp}{Uo} = 0.8$ and 1.2. The wake is very clearly defined with concentric curves around the tail. The third mode is shown by $\frac{Cp}{Uo}$ =1.6, 2.0, and 2.4. These wakes show a peak in the center of the tail. The contour lines curve significantly and for all three $\frac{Cp}{Uo}$ values, the contour pattern is the same. A large indentation appears to the right of the center of the snake. In a few of these cases an oval area appears suggesting a vortex formation.

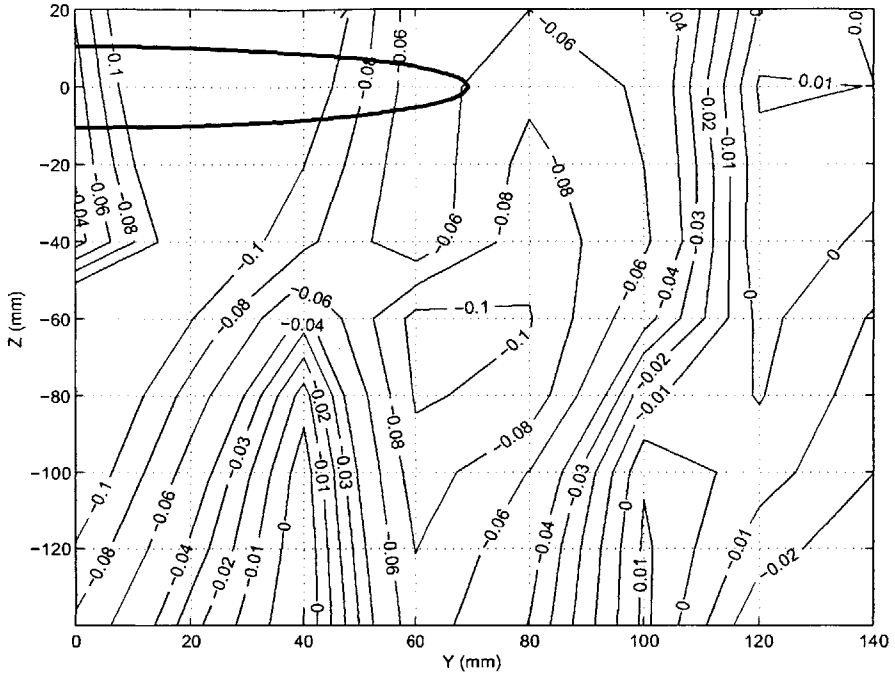

Figure 5-3: Wake profile of $\Delta(P + \frac{1}{2}\rho u^2)$ for $\frac{C_P}{U_o} = 0.4$.

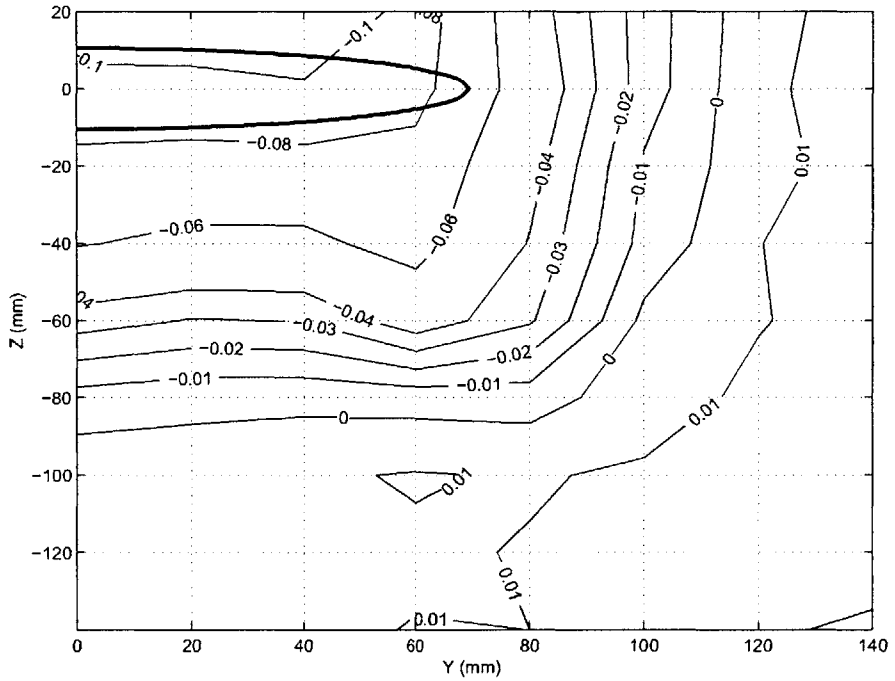

Figure 5-4: Wake profile of $\Delta(P + \frac{1}{2}\rho u^2)$ for $\frac{C_P}{U_o} = 0.8$.

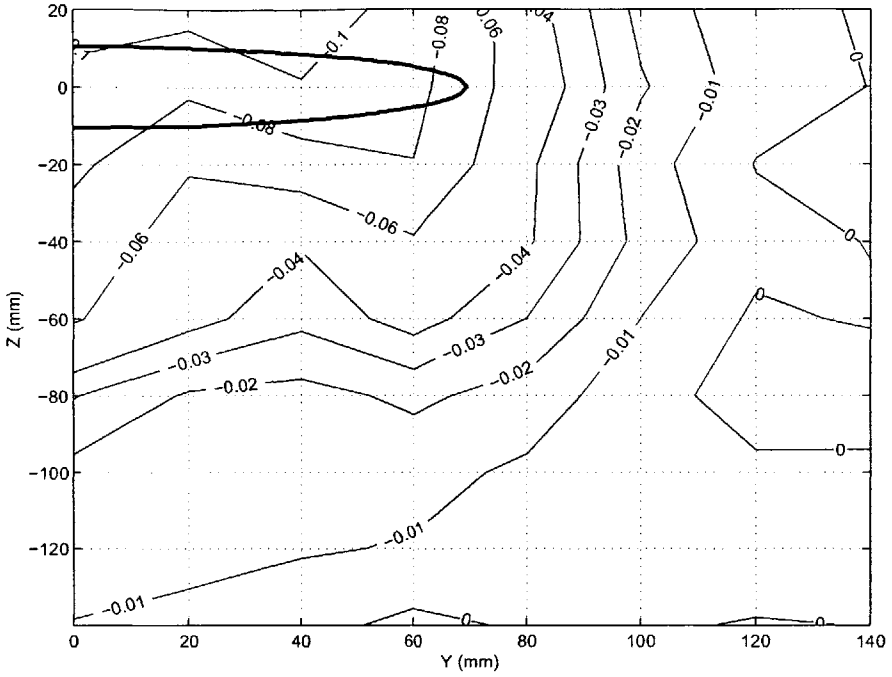

Figure 5-5: Wake profile of $\Delta(P + \frac{1}{2}\rho u^2)$ for $\frac{C_p}{U_o} = 1.2$.

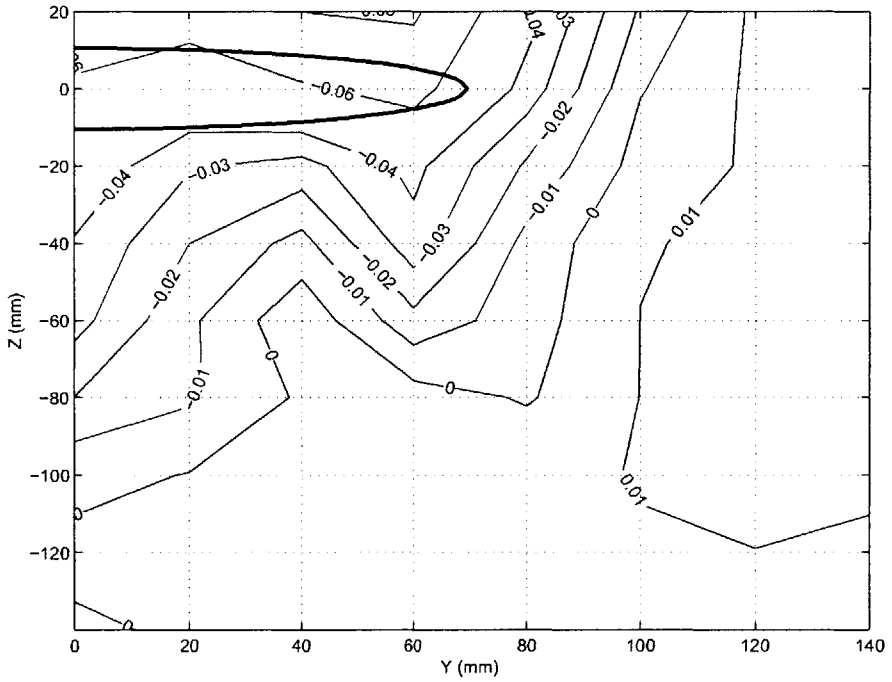

Figure 5-6: Wake profile of $\Delta(P + \frac{1}{2}\rho u^2)$ for $\frac{C_p}{U_o} = 1.6$.

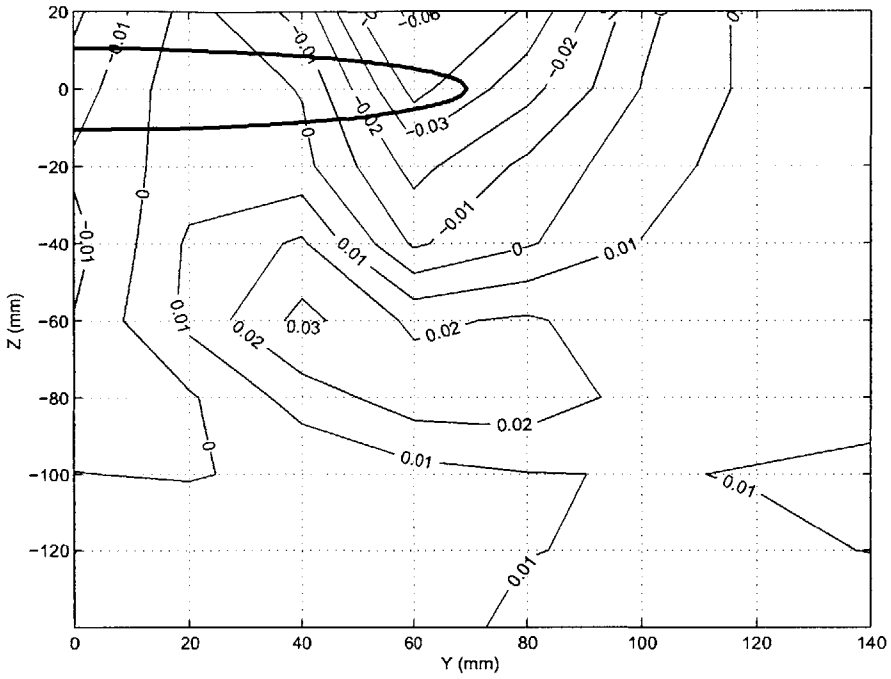

Figure 5-7: Wake profile of $\Delta(P + \frac{1}{2}\rho u^2)$ for $\frac{Cp}{Uo} = 2.0$ run 1.

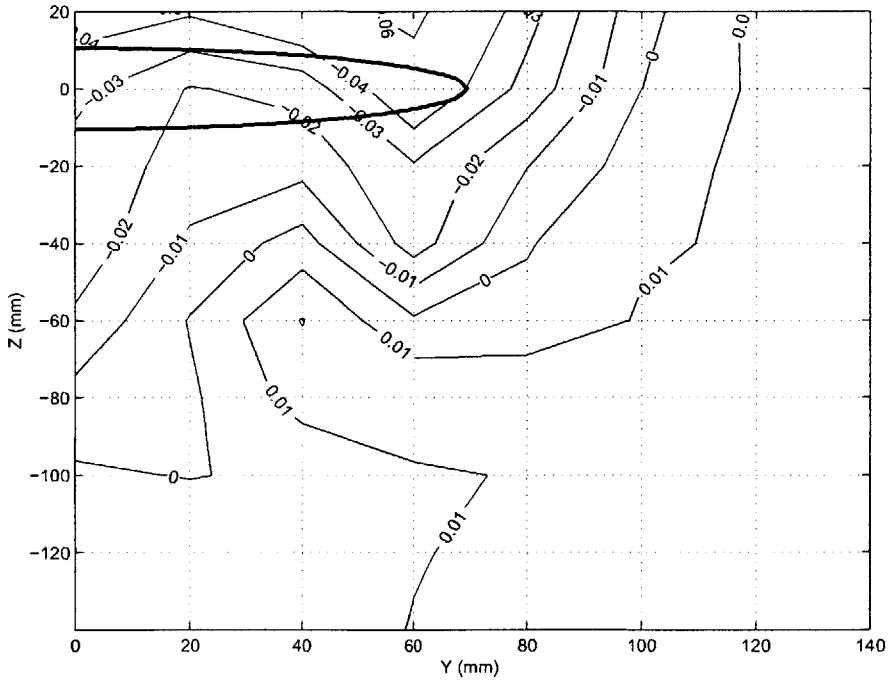

Figure 5-8: Wake profile of $\Delta(P + \frac{1}{2}\rho u^2)$ for $\frac{Cp}{Uo} = 2.0$ run 2.

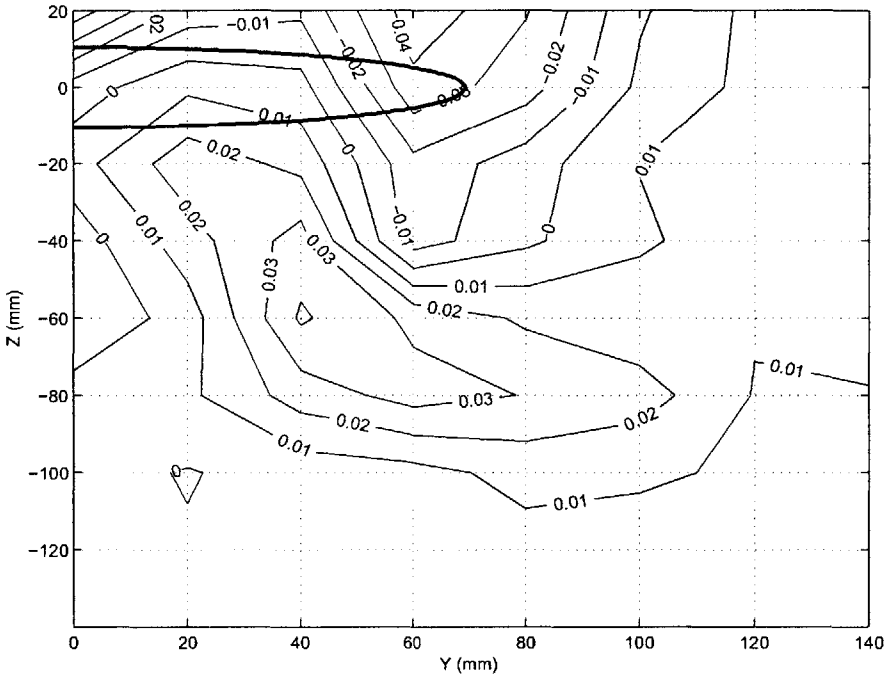

Figure 5-9: Wake profile of $\Delta(P + \frac{1}{2}\rho u^2)$ for $\frac{Cp}{Uo} = 2.4$.

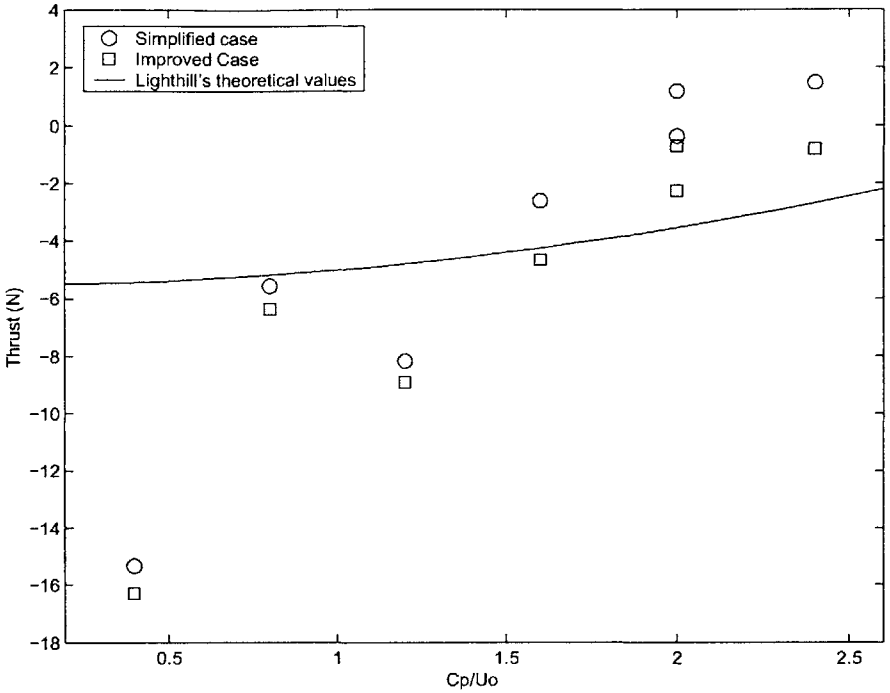

Figure 5-10: Thrust production in the wake for all values of $\frac{Cp}{Uo}$. Each point represents the data of the quarter quadrant used for the calculation multiplied by 4. The circles represent the calculation using the simplified case. The squares represent the calculation using the improved case. The line shows the slope of the theoretical curve predicted by Lighthill.

Figure 5-10 shows the results of the thrust calculations. The circles represent the results of running the simplified thrust calculation. The squares represent the results for the improved case. The line shows the theoretical result as predicted by Lighthill and described below. The general trend of the graphs shows that as $\frac{Cp}{Uo}$ increases, the thrust increases. There is a deviation from this at $\frac{Cp}{Uo} = 1.2$ where the thrust is lower than the value at $\frac{Cp}{Uo} = 0.8$. Negative thrust indicates that the drag force is greater than the thrust force. A large drag force exists at $\frac{Cp}{Uo} = 0.4$, which suggests that the snake is acting as a bluff body at this point. At $\frac{Cp}{Uo} = 2.0$ - 2.4, the snake begins to reach a level of zero thrust, which suggests that the snake is capable of self-propulsion here.

5.4 Lighthill's Theory on Thrust Production by Anguilliform Swimmers

Lighthill's theory was applied to the case of the snake to examine if his equations matched the results of the experimental snake. His derivation uses a kinetic energy balance for the calculation of thrust through a comparison of the work on the virtual mass of the lateral movement with its kinetic energy. Lighthill's equations show that with the assumption of inviscid theory and the assumption that vorticity is shed only from the tail, the propulsion of the snake comes only from the tail and that the body provides no propulsive force. Lighthill's theory shows that the body undulations are used to drive the tail and do not contribute significantly to the thrust [12]. If this is true, then the undulatory motion that the snake uses would have evolved for another reason, possibly drag reduction through the reduction of turbulence.

For anguilliform swimmers, Lighthill, shows that the power produced is equal to

$$P = [mw(W - \frac{1}{2}w)]_{x=L} - \frac{\partial}{\partial t}\int_0^l (mw\frac{\partial y}{\partial x})dx \tag{5.20}$$

where P is power, ρ is the water density, L is the length, x is the distance along the snake,
m is the virtual (added) mass per unit length and is approximated by:

$$m = \frac{1}{4}\pi s^2 \rho\beta \tag{5.21}$$

and β is a non-dimensional coefficient that is one for an elliptic cross-section of any eccentricity, therefore, is one for a snake or eel. w is the velocity that a water slice is laterally pushed and is defined as

$$w = \frac{\partial y}{\partial t} + U\frac{\partial y}{\partial x} \tag{5.22}$$

where y(x,t) is the amount that the cross-section is displaced during undulations and

for the snake this is defined as sinusoidal motion as previously described and is

$$y(x,t) = Ax\sin(\omega t - kx) \tag{5.23}$$

When the partial derivatives of equation 5.22 are applied to this equation the result is:

$$\begin{aligned} w &= (Ax(\omega - Uk)\cos(\omega t - kx) + UA\sin(\omega t - kx))|_{x=L} \\ &= AL(\omega - Uk)\cos(\omega t - kL) + UA\sin(\omega t - kL) \end{aligned} \tag{5.24}$$

W is the trailing-edge lateral velocity and can be defined as:

$$W = \frac{\partial y}{\partial t} \tag{5.25}$$

Again using the definition of y, W can be rewritten as

$$\begin{aligned} W &= Ax\omega\cos(\omega t - kx)|_{x=L} \\ &= AL\omega\cos(\omega t - kL) \end{aligned} \tag{5.26}$$

The first term of equation 5.27 is equal to zero since the time derivative of a fluctuating quantity has a mean of zero and therefore this equation can be reduced to:

$$P = [mw(W - \frac{1}{2}w)]_{x=l} \tag{5.27}$$

Taking the W and w expressions at x=L and plugging them into equation 5.27 and simplifying gives:

$$
\begin{aligned}
P &= m_L(AL(\omega - Uk)\cos(\omega t - kx) + UA\sin(\omega t - kx)) \\
&\quad (\frac{1}{2}AL(\omega + Uk)\cos(\omega t - kx) - \frac{1}{2}UA\sin(\omega t - kx)) \\
&= m_L(\frac{1}{2}A^2L^2(\omega - Uk)(\omega + Uk)\cos(\omega t - kx) - \frac{1}{2}A^2U^2\sin^2(\omega t - kx)) \quad (5.28)
\end{aligned}
$$

To calculate an average thrust, the average value of $\sin^2(\omega t - kx) = \frac{1}{2}$ and the average value of $\cos^2(\omega t - kx) = \frac{1}{2}$ are applied which simplifies the equation to:

$$\overline{P} = \frac{1}{4}m_L A^2[L^2(\omega^2 - U^2k^2) - U^2] \quad (5.29)$$

For the snake, m_L, can be calculated by approximating the tail as a flat plate and using a strip theory approach.

$$m_L = \rho\frac{\pi}{4}l^2 \quad (5.30)$$

where l is the width of the snake tail.

The amplitude of the snake is $A = \frac{x}{16}$ and since the expression is being evaluated at x=L, $A = \frac{1}{16}$. L is taken to be the length of the snake and equals one meter. ω is the value of 2πCp. U is the inflow velocity which equals 1 m/s. k is the wavenumber that equals $\frac{2\pi}{\lambda}$ where $\lambda = 1$. This equation was then used and the results are shown plotted as a line in figure 5-10. The slope of the Lighthill plot is the important element and not its position on the figure since his equation cannot account for viscous drag. The experimental results include the drag, therefore to make a comparison with Lighthill's theoretical results for outgoing thrust, Lighthill's curve was plotted in an area that would allow it to be compared to the slope of the experimental results.

Several assumptions are used by Lighthill in his derivation. Lighthill's equations are based on elongated-body theory which is an extension of inviscid slender-body theory. In addition, his derivations are based on an animal that satisfies his definition of pure-anguilliform. These swimmers, such as eels, possess long continuous dorsal and ventral fins, a continuous cross-sectional depth, and a tapered tail which provides a vertical trailing edge [12]. These fins and tapered tails are not present on the snake

model as they are not characteristic of a sea snake body. Lighthill also assumes that when water is pushed laterally, a certain lateral momentum for that water slice exists and the momentum is equal to mw per unit length. However, this value can be exceeded when viscous forces are accounted for, such as from streamwise vortex shedding.

Chapter 6

Conclusions

This thesis examines the hydrodynamics of a swimming sea snake model. This project demonstrated the ability to study the hydrodynamics, both near-body and wake, of anguilliform swimming motion with the use of the snake model developed and the MIT Water Tunnel. Two types of measurements were made, velocity and pressure. The experiments demonstrated the effectiveness of kiel probe and LDV technology for studying hydrodynamics in the water tunnel.

Using biomimetic principles, a model sea snake was designed. The snake was cast with polyurethane rubber and was constructed to use Techet's waving plate mechanism. Tests in the water tunnel showed that the snake model was capable of being used for characterizing the hydrodynamics of a three-dimensional swimming body.

Near-body turbulence was studied with the LDV system. Measurements were taken at pistons five and six with the snake in both the trough and crest position. At both piston locations, turbulence reduction was shown for the trough position for $\frac{Cp}{Uo} = 1.2$. This supports previous two-dimensional studies, both experimental and numerical. The crest position, however, showed the highest turbulence at $\frac{Cp}{Uo} = 1.2$. This differs from the two-dimensional studies which exhibited a turbulence minimum in the crest at this $\frac{Cp}{Uo}$ value. This near-body turbulence data raises important questions about the flow of the 3D snake vs. a 2D plate. Further work is needed to clarify this data.

Velocity and pressure profiles were made in the wake of the snake. The rms values of the velocity was shown to be significantly less for $\frac{C_p}{U_o} = 1.2$. The profiles suggest that the snake pushes the fluid downwards in its center causing both vorticity generation and flow over the sides of the snake. Dye visualization could be used in the future to better understand these profiles.

The velocity and pressure data was extended into a calculation of thrust in the wake using the momentum control volume approach. A derivation was made that enabled the stagnation pressure, measured by the kiel probes, to be used for calculating the thrust. The results showed that in general as $\frac{C_p}{U_o}$ increased, the thrust increased. However, for all of the cases less than $\frac{C_p}{U_o} = 2.0$, the thrust was significantly less than zero. This indicates that the drag of the snake body is greater than the thrust it is producing. The momentum profiles in the wake show different modes of development. The first mode shows a highly complex wake which suggests a drag wake. The second mode shows a highly ordered and symmetric wake. The third mode shows the fluid being pushed downwards and vortices being generated.

Appendix A

Turbulence Levels for Piston Five

This appendix includes the data for all of the distances where turbulence intensity was measured at the piston five location. For each $\frac{Cp}{Uo}$ value, two plots are shown. The top plot shows the average turbulence intensity at four values of $\frac{Cp}{Uo}$. The lower plot shows the turbulence intensity measured over 360 degrees, with two cycles being shown. Trough and crest data are shown in separate figures. The figures are organized first by position, trough and then crest, and then by distance from the snake body.

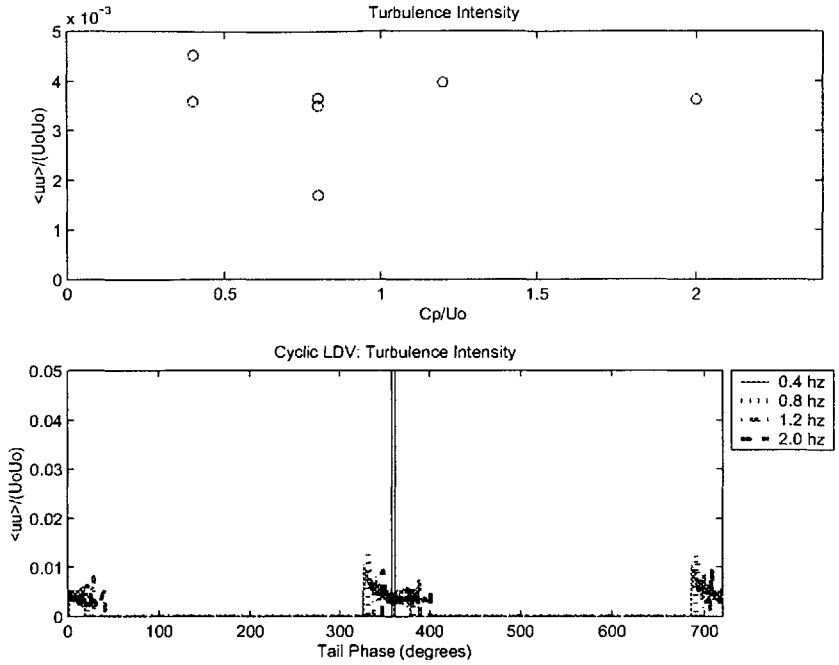

Figure A-1: Turbulence intensity for piston five trough position at a distance of 2 mm away from the snake body.

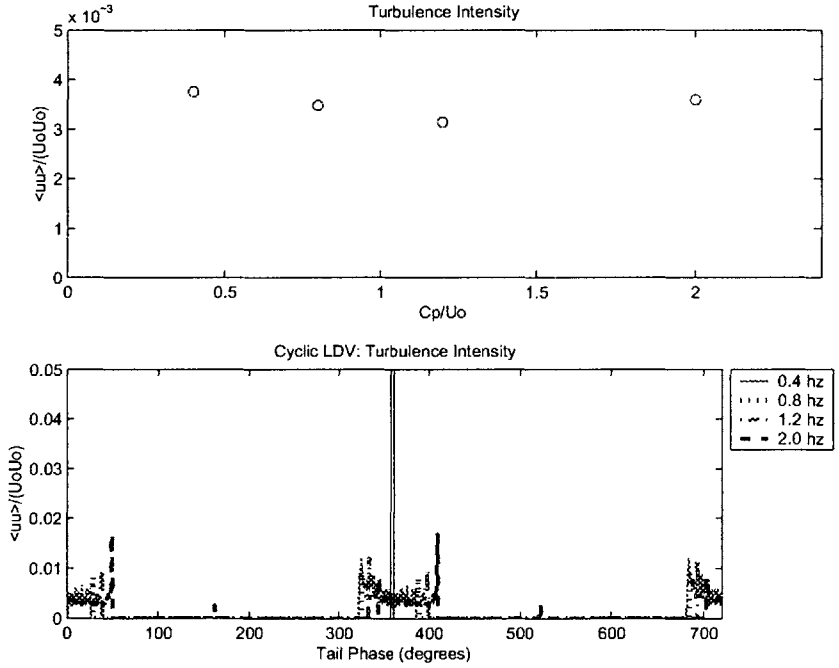

Figure A-2: Turbulence intensity for piston five trough position at a distance of 4 mm away from the snake body.

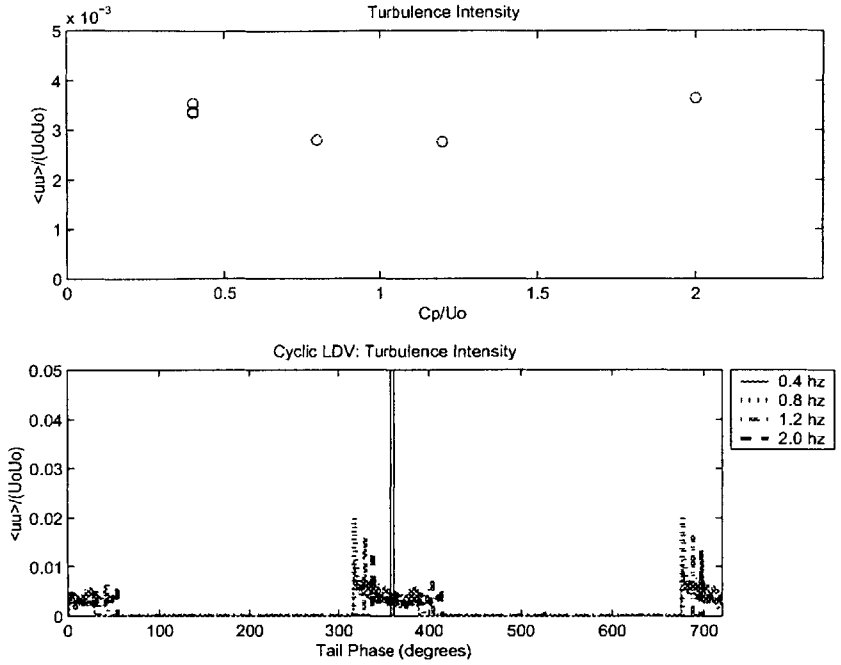

Figure A-3: Turbulence intensity for piston five trough position at a distance of 6 mm away from the snake body.

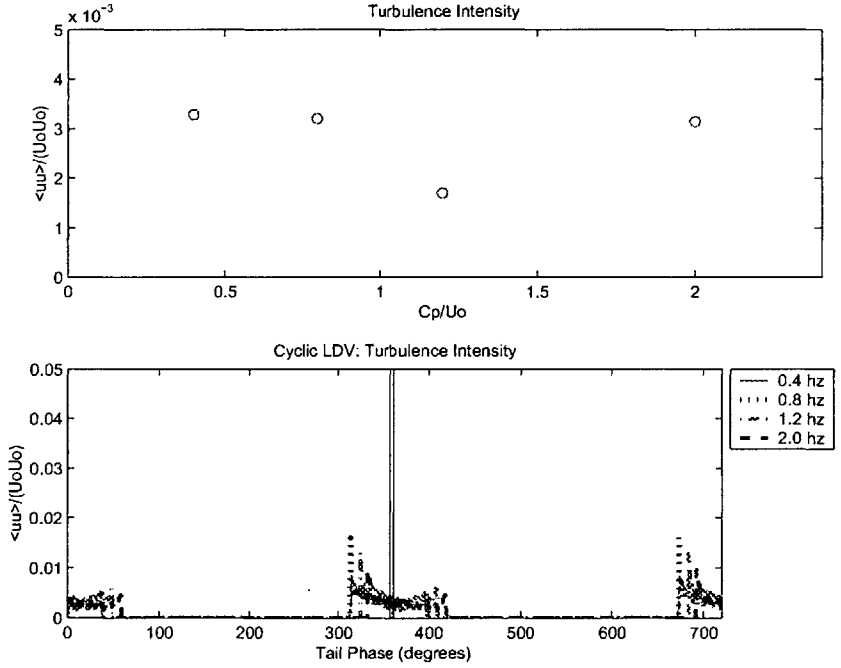

Figure A-4: Turbulence intensity for piston five trough position at a distance of 8 mm away from the snake body.

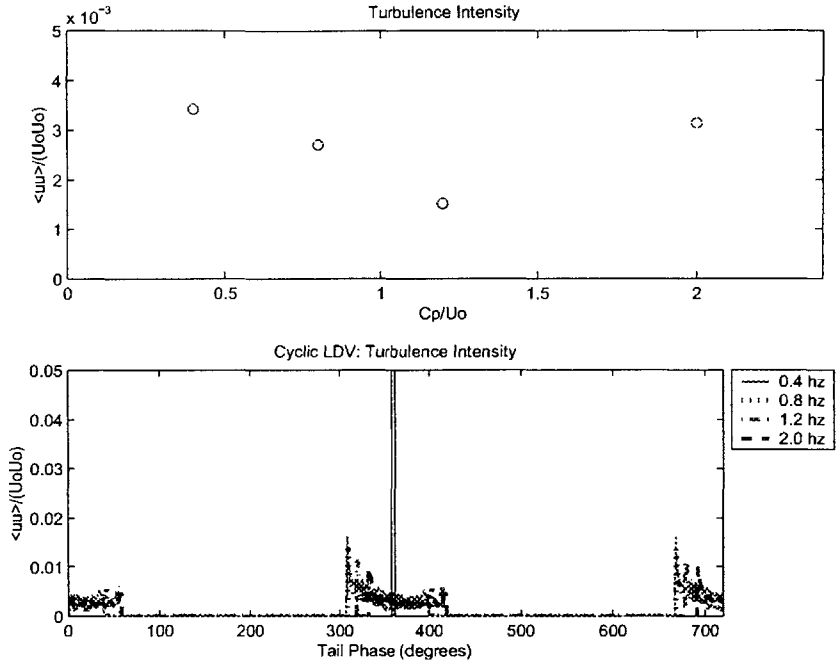

Figure A-5: Turbulence intensity for piston five trough position at a distance of 10 mm away from the snake body.

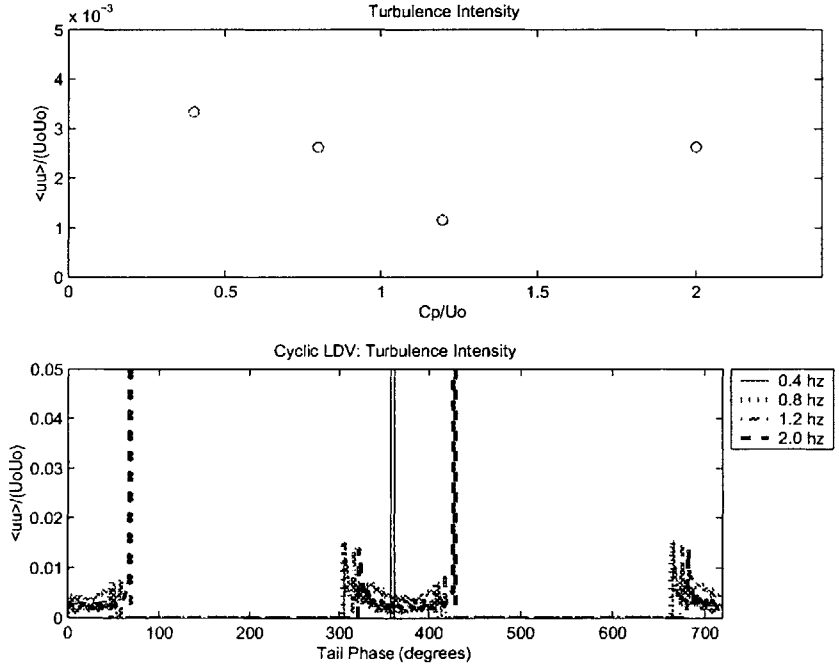

Figure A-6: Turbulence intensity for piston five trough position at a distance of 12 mm away from the snake body.

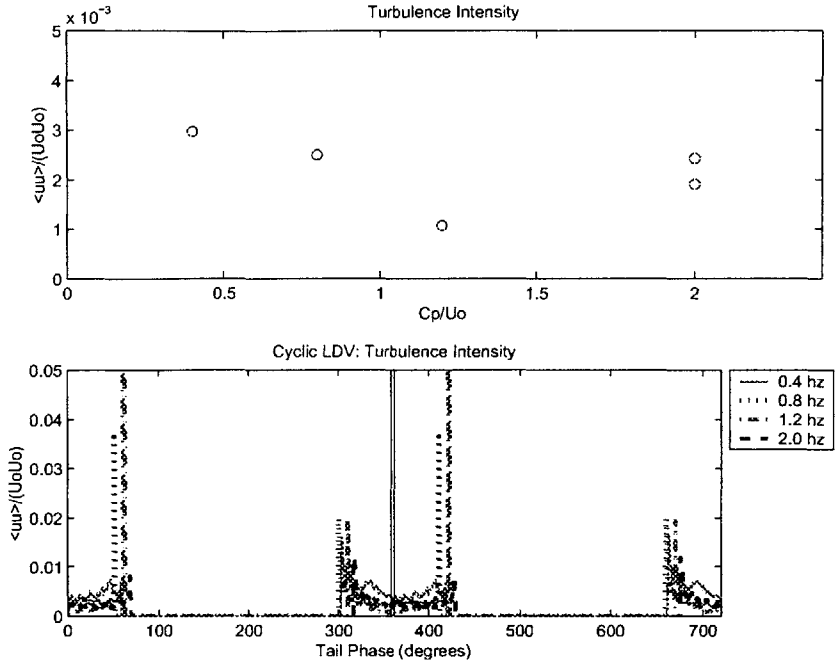

Figure A-7: Turbulence intensity for piston five trough position at a distance of 14 mm away from the snake body.

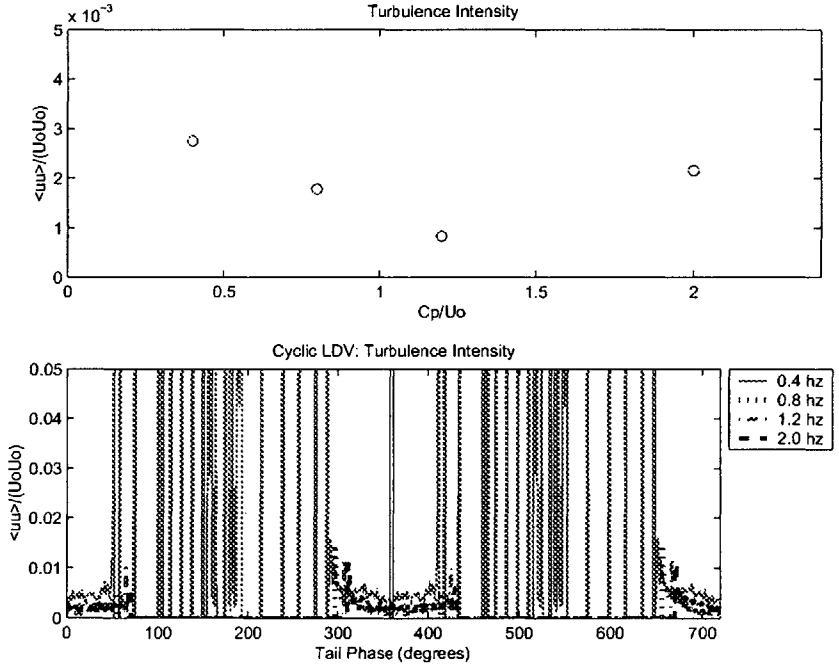

Figure A-8: Turbulence intensity for piston five trough position at a distance of 16 mm away from the snake body.

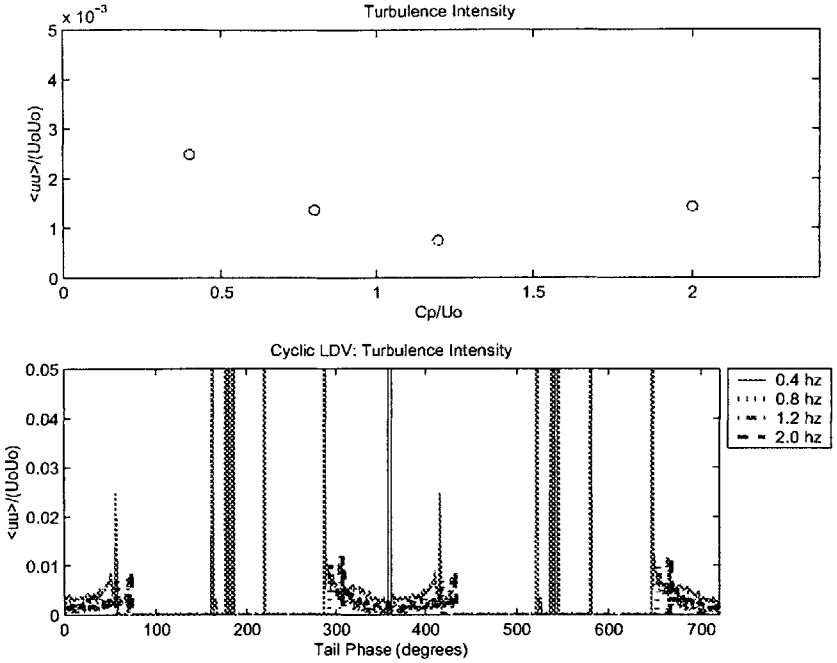

Figure A-9: Turbulence intensity for piston five trough position at a distance of 18 mm away from the snake body.

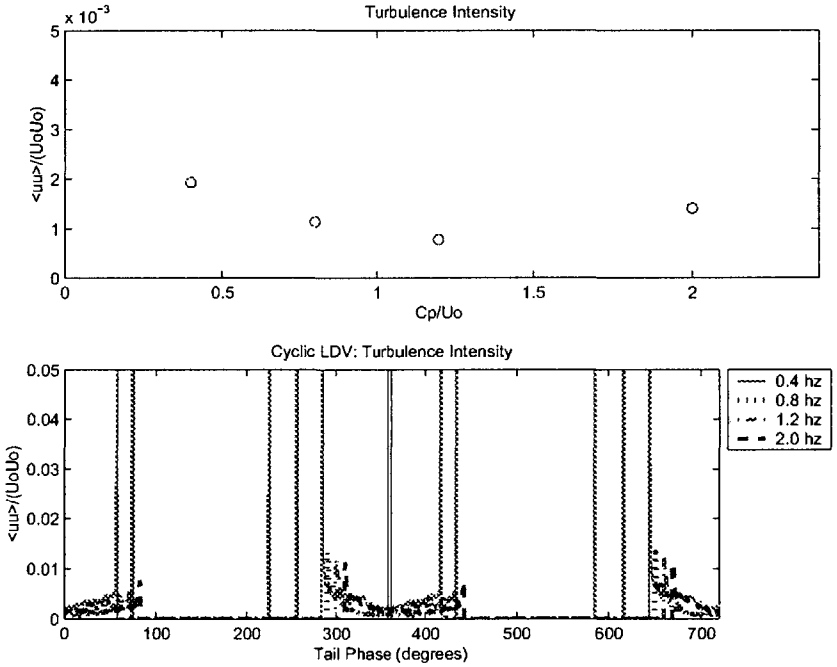

Figure A-10: Turbulence intensity for piston five trough position at a distance of 20 mm away from the snake body.

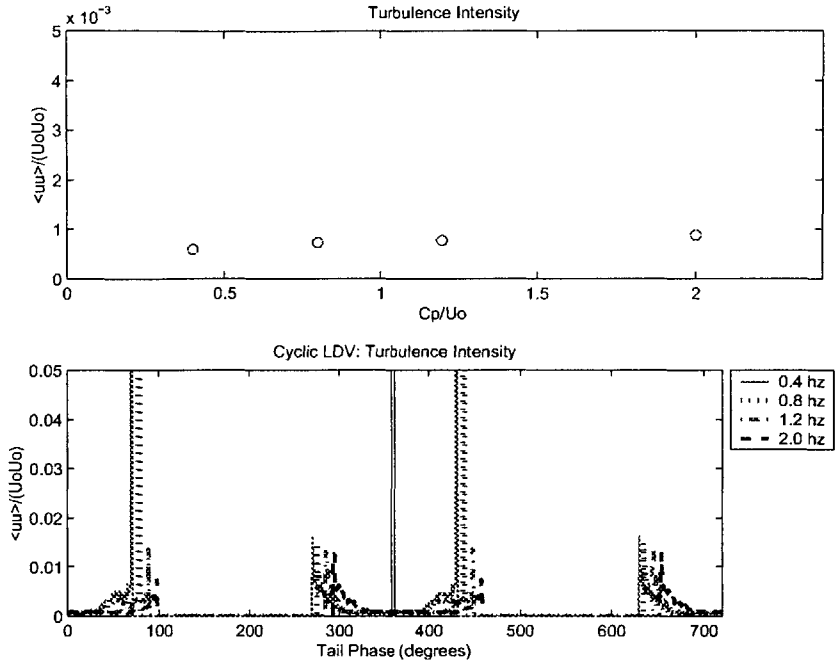

Figure A-11: Turbulence intensity for piston five trough position at a distance of 30 mm away from the snake body.

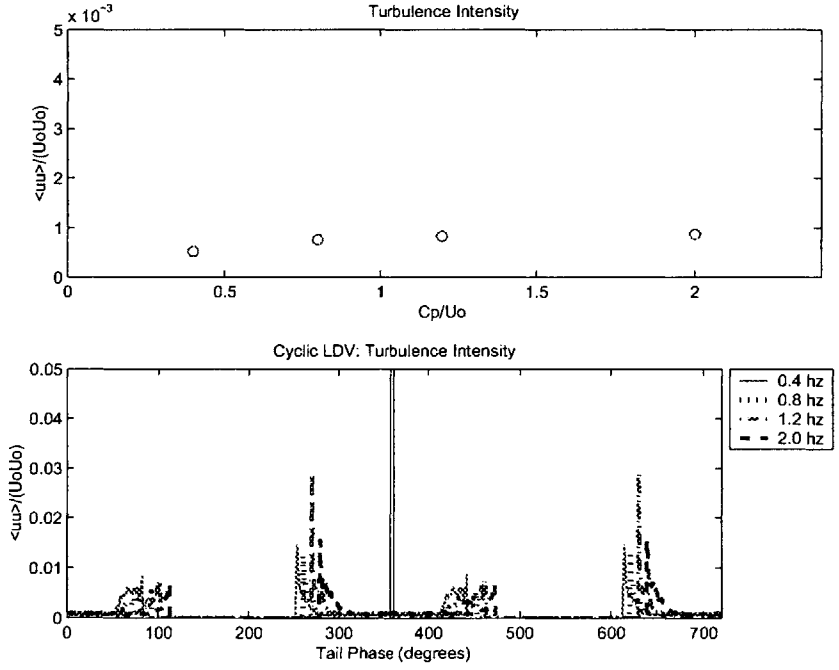

Figure A-12: Turbulence intensity for piston five trough position at a distance of 40 mm away from the snake body.

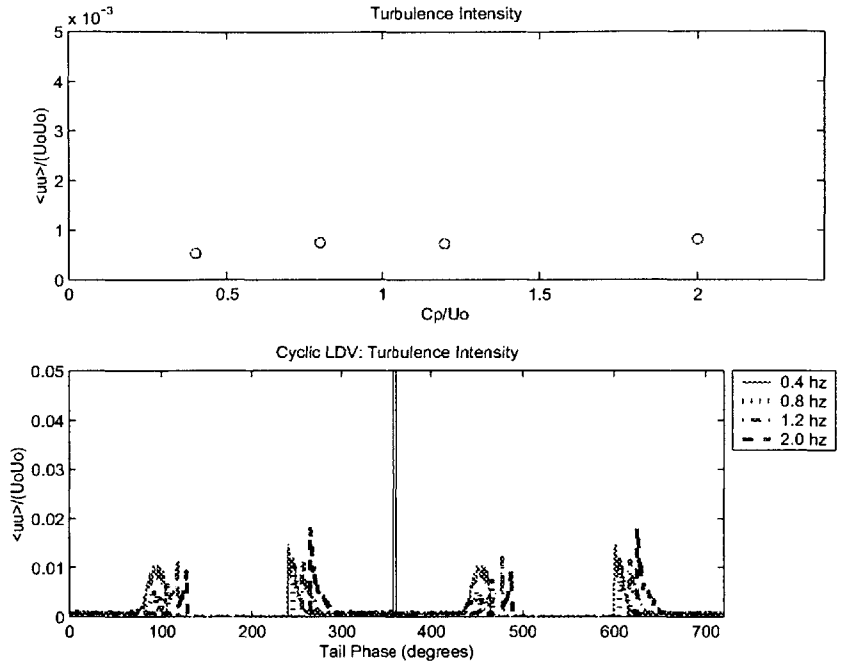

Figure A-13: Turbulence intensity for piston five trough position at a distance of 50 mm away from the snake body.

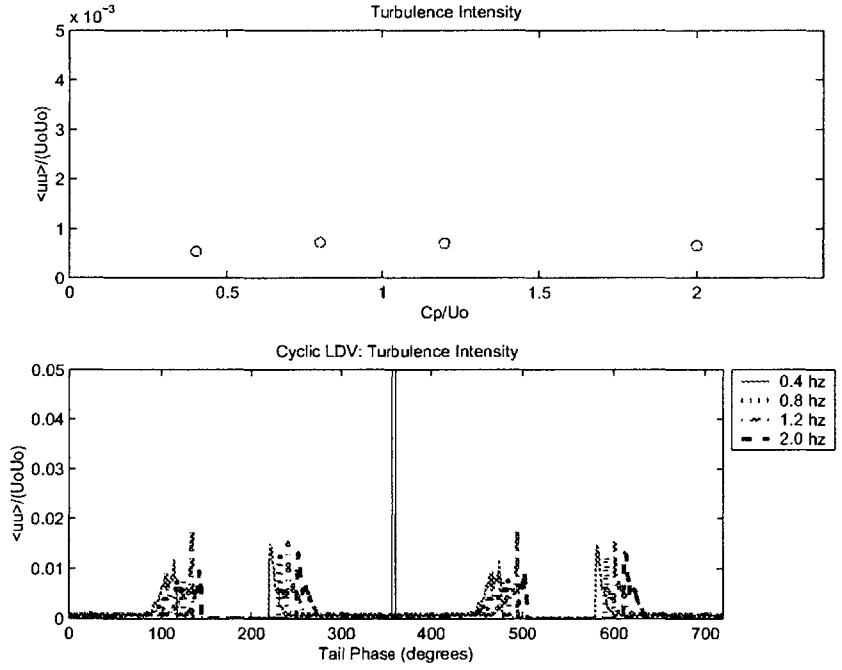

Figure A-14: Turbulence intensity for piston five trough position at a distance of 60 mm away from the snake body.

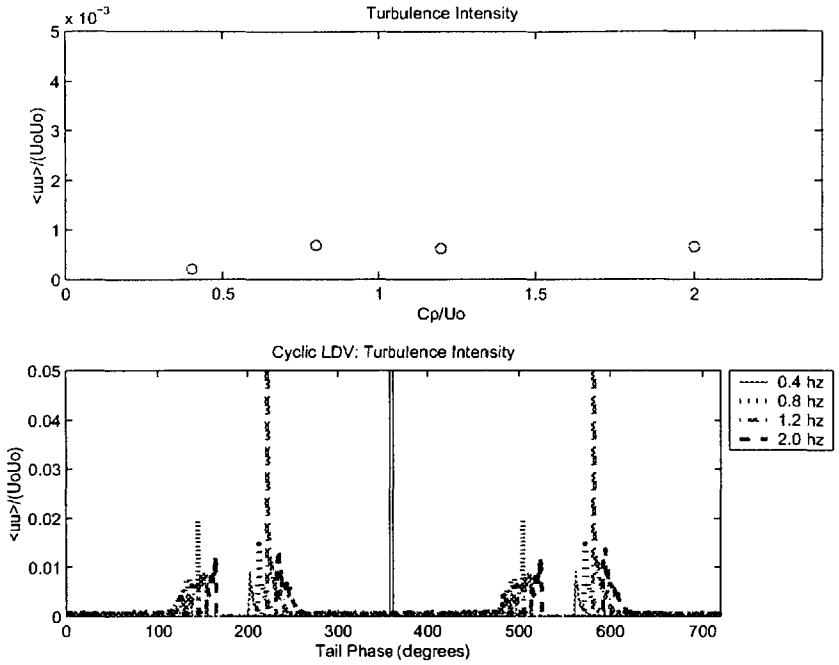

Figure A-15: Turbulence intensity for piston five trough position at a distance of 70 mm away from the snake body.

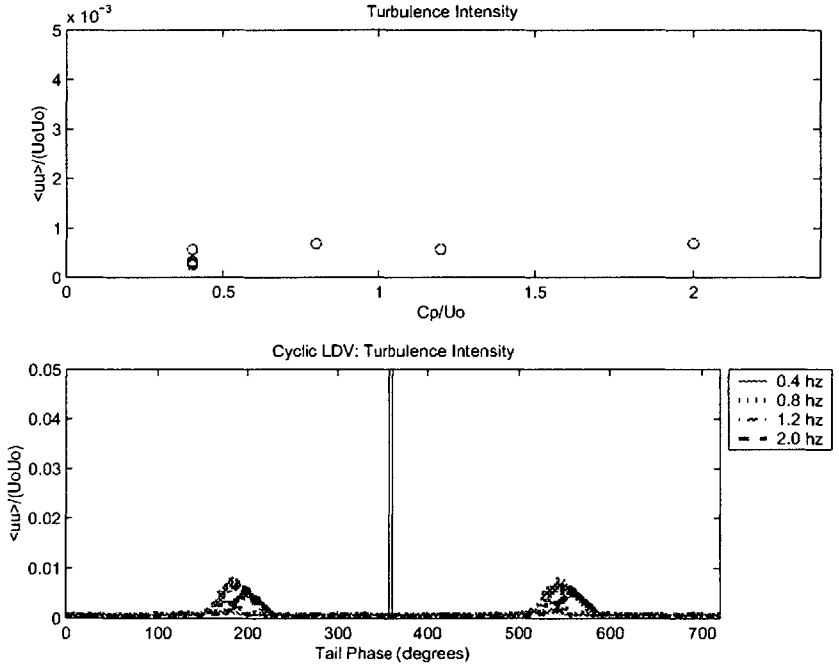

Figure A-16: Turbulence intensity for piston five trough position at a distance of 82 mm away from the snake body.

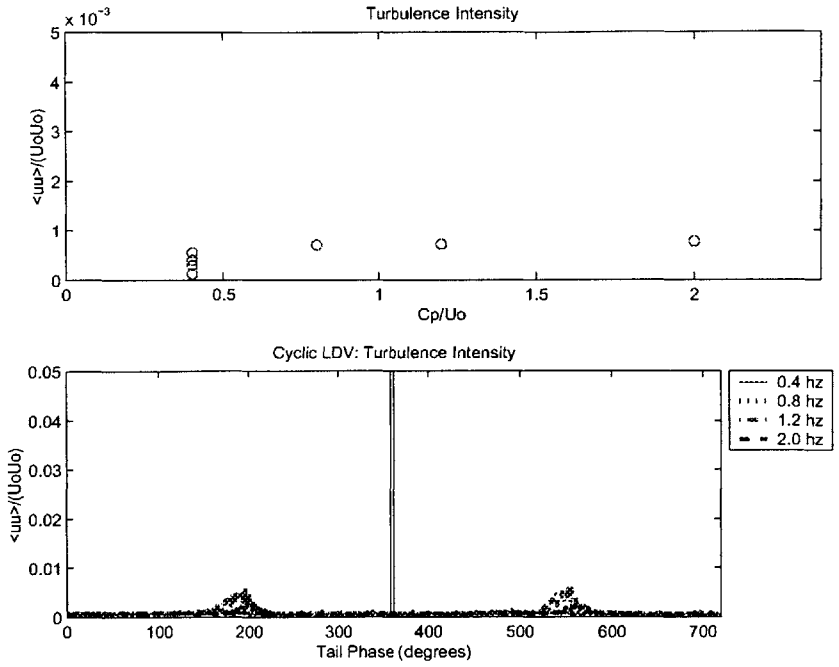

Figure A-17: Turbulence intensity for piston five trough position at a distance of 84 mm away from the snake body.

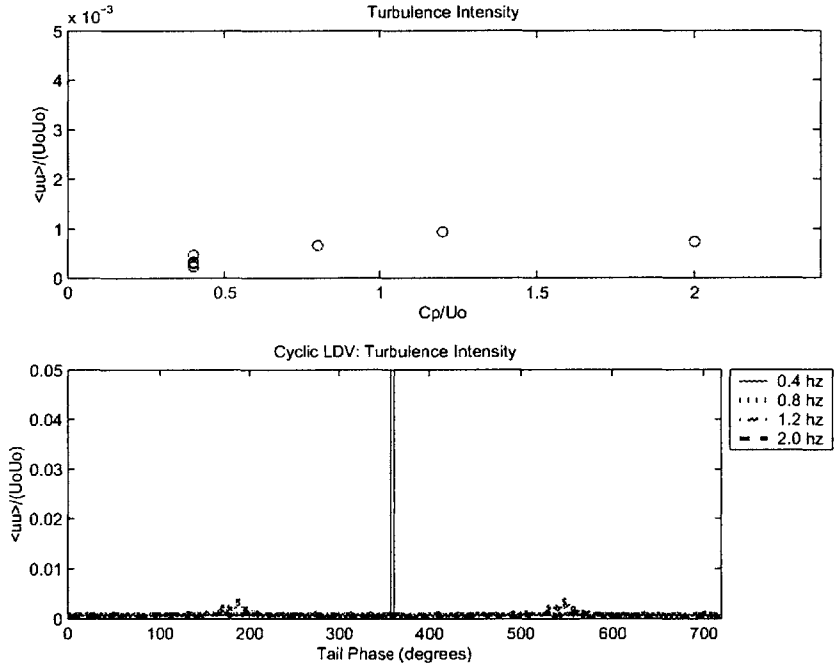

Figure A-18: Turbulence intensity for piston five trough position at a distance of 86 mm away from the snake body.

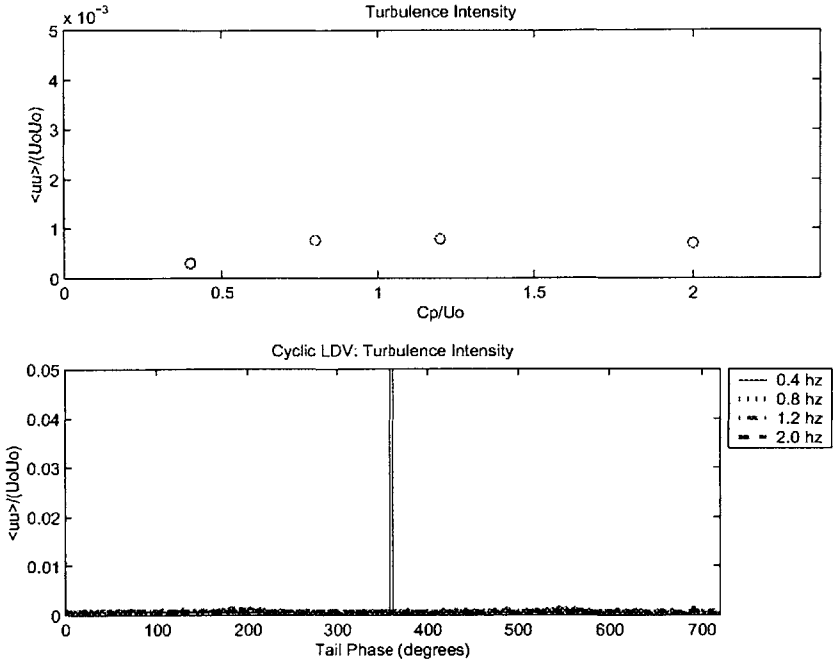

Figure A-19: Turbulence intensity for piston five trough position at a distance of 88 mm away from the snake body.

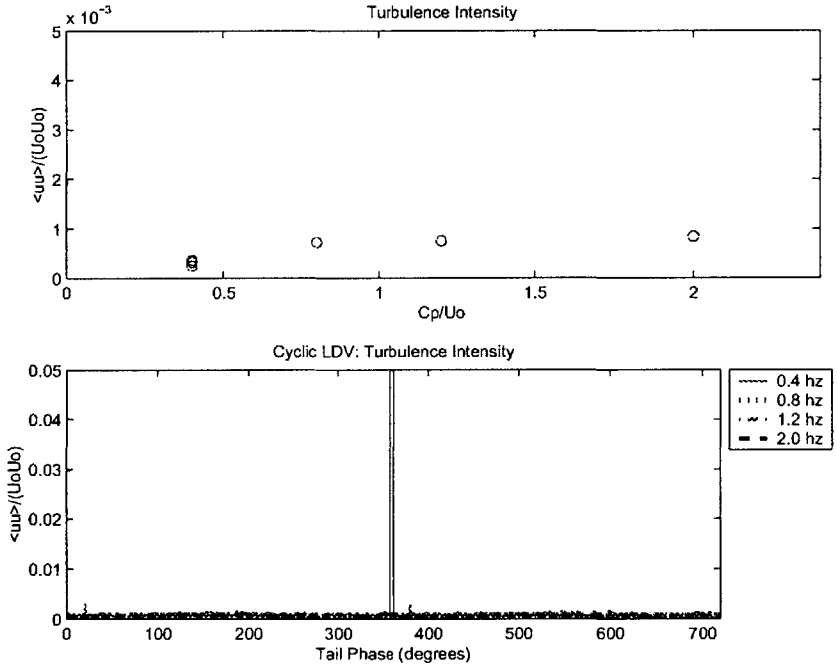

Figure A-20: Turbulence intensity for piston five trough position at a distance of 90 mm away from the snake body.

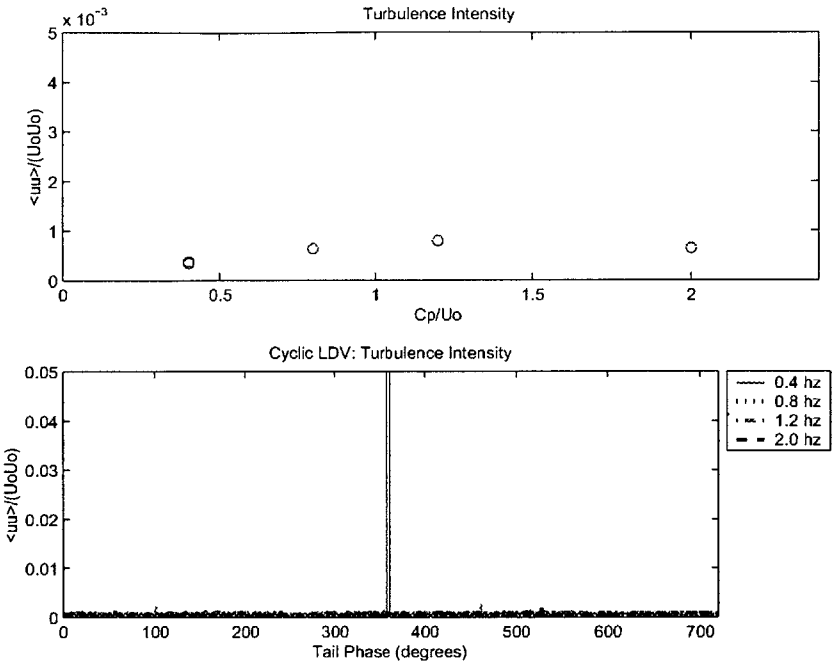

Figure A-21: Turbulence intensity for piston five trough position at a distance of 95 mm away from the snake body.

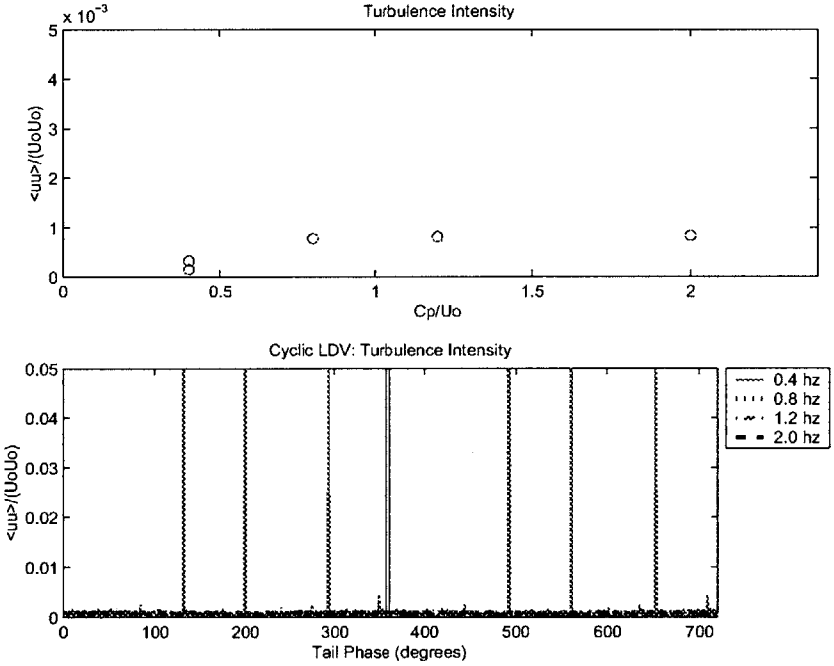

Figure A-22: Turbulence intensity for piston five trough position at a distance of 110 mm away from the snake body.

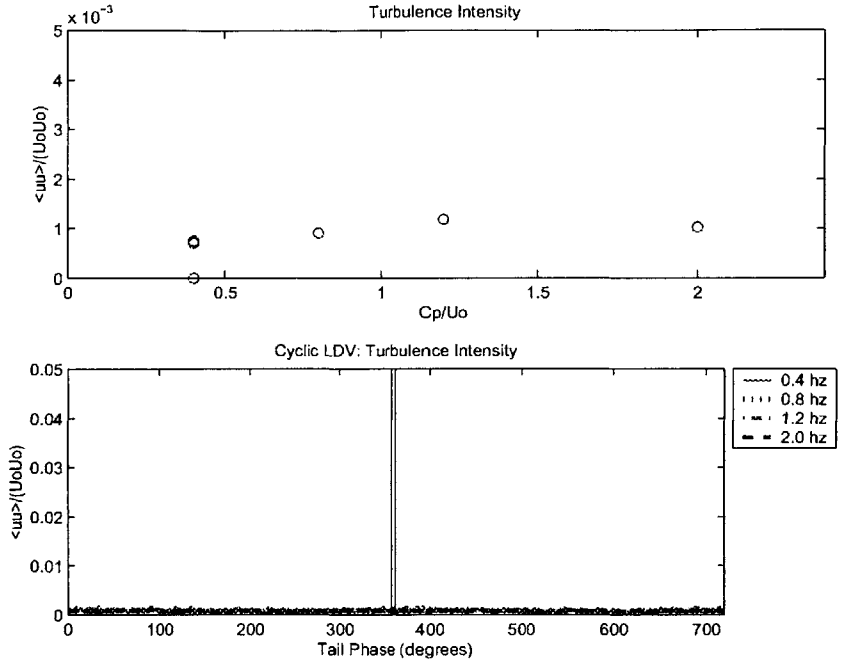

Figure A-23: Turbulence intensity for piston five trough position at a distance of 115 mm away from the snake body.

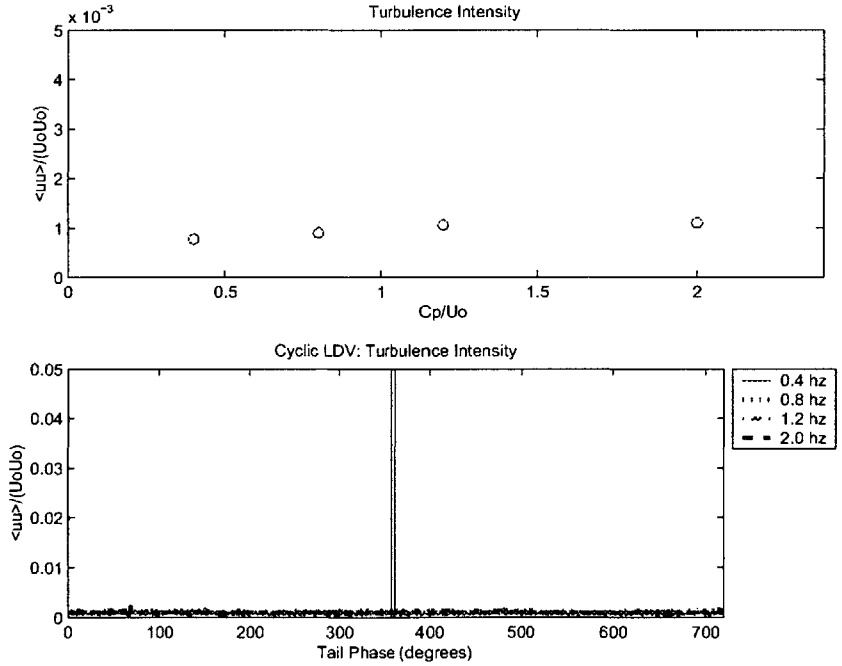

Figure A-24: Turbulence intensity for piston five trough position at a distance of 120 mm away from the snake body.

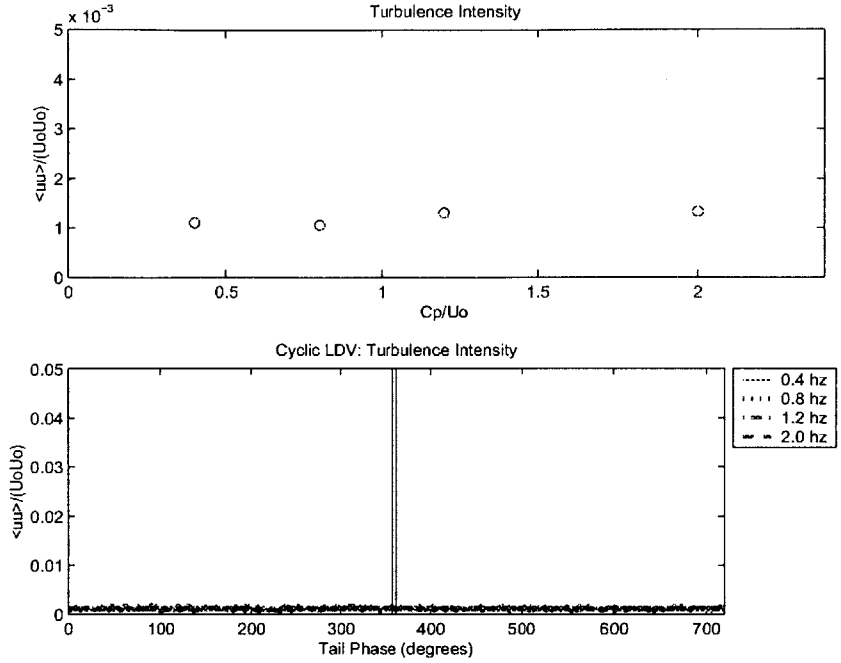

Figure A-25: Turbulence intensity for piston five trough position at a distance of 145 mm away from the snake body.

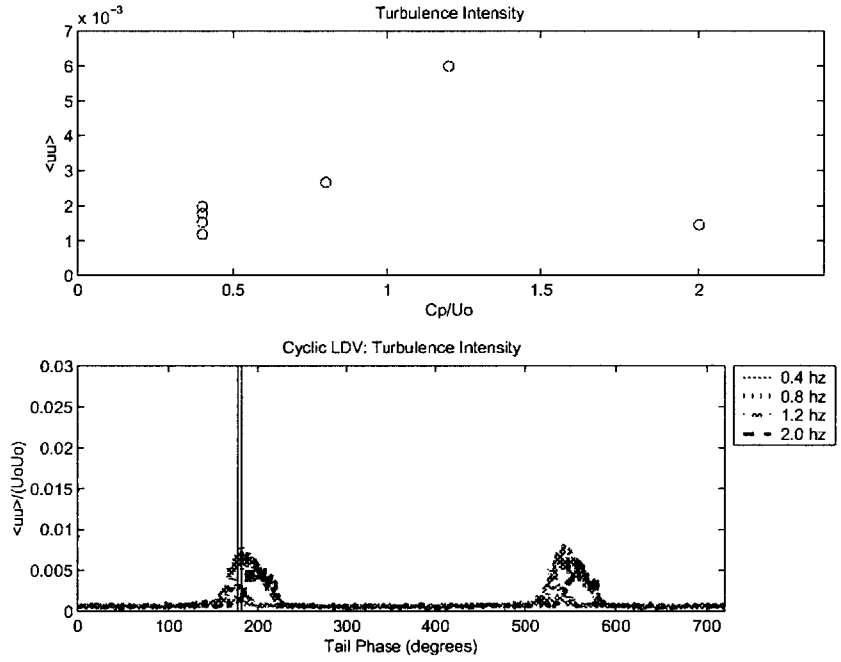

Figure A-26: Turbulence intensity for piston five crest position at a distance of 8 mm away from the snake body.

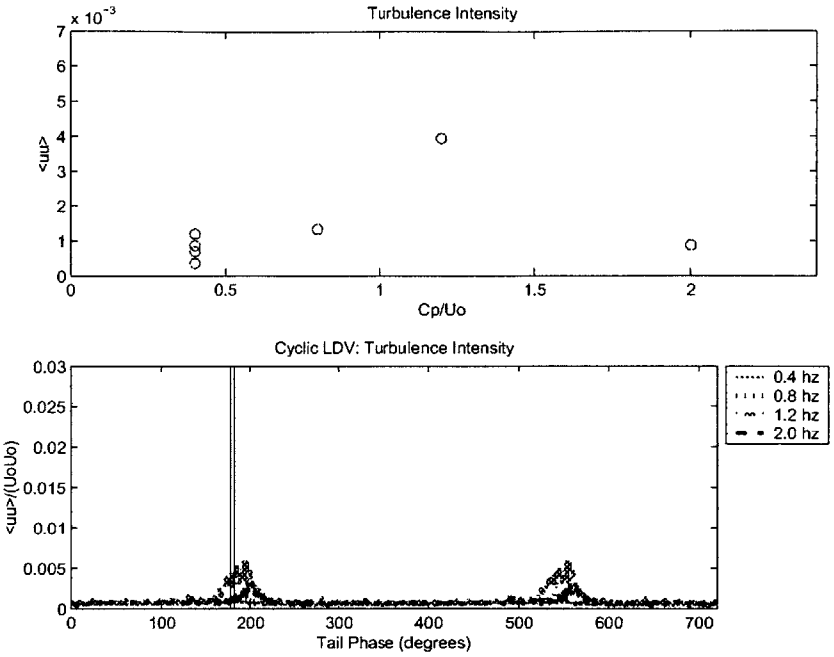

Figure A-27: Turbulence intensity for piston five crest position at a distance of 10 mm away from the snake body.

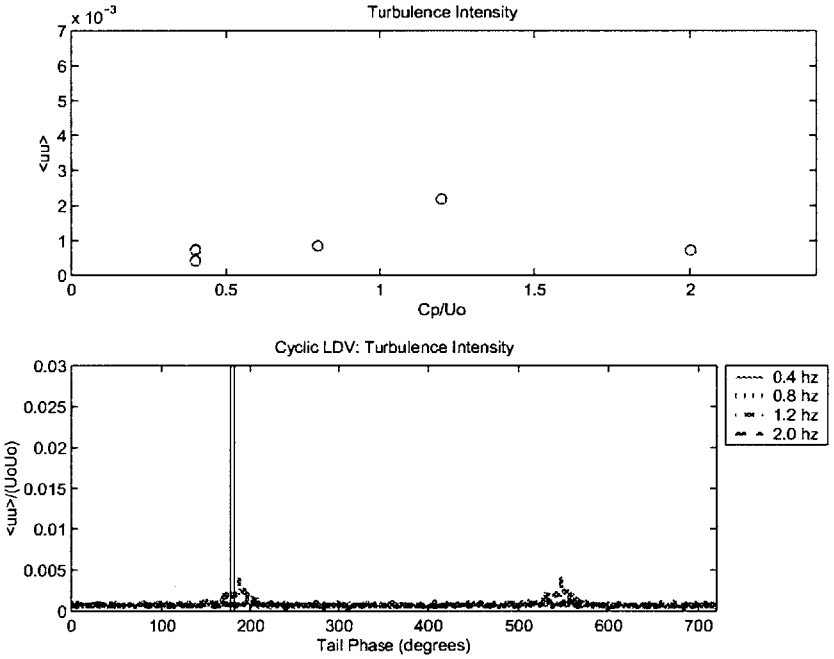

Figure A-28: Turbulence intensity for piston five crest position at a distance of 12 mm away from the snake body.

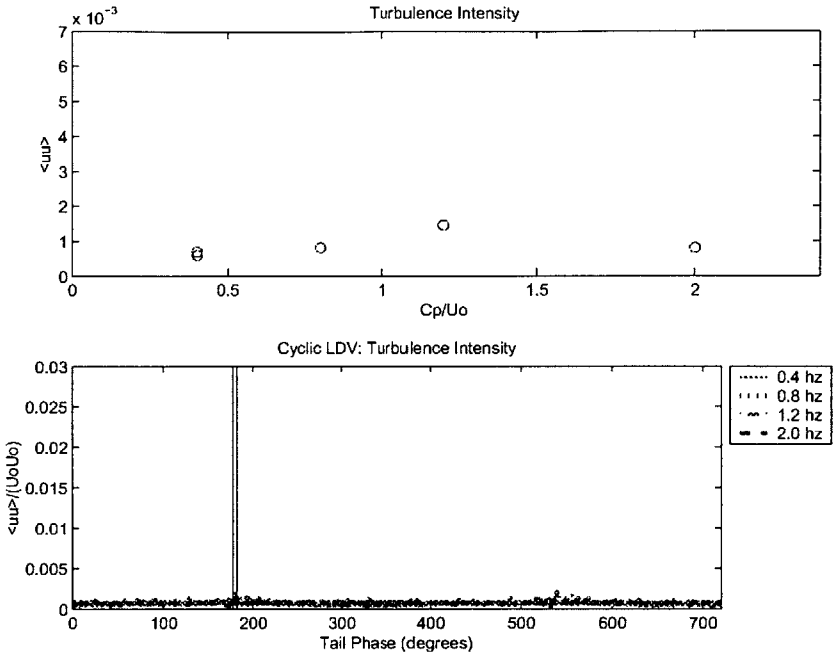

Figure A-29: Turbulence intensity for piston five crest position at a distance of 14 mm away from the snake body.

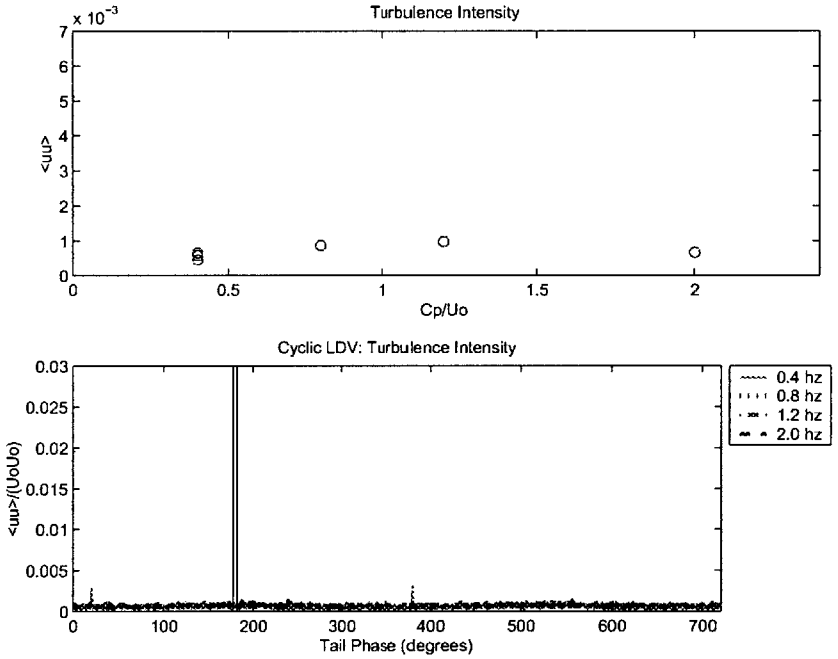

Figure A-30: Turbulence intensity for piston five crest position at a distance of 16 mm away from the snake body.

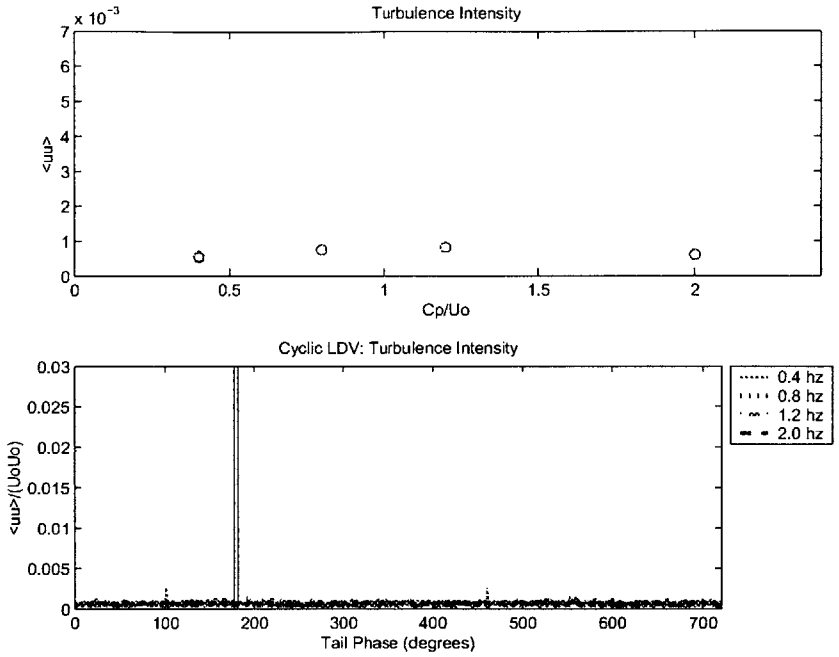

Figure A-31: Turbulence intensity for piston five crest position at a distance of 21 mm away from the snake body.

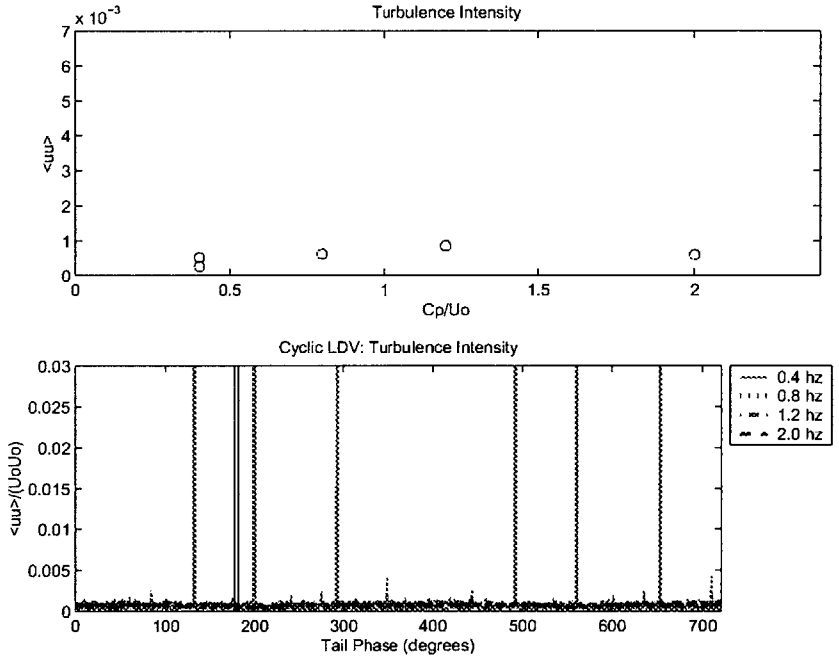

Figure A-32: Turbulence intensity for piston five crest position at a distance of 53 mm away from the snake body.

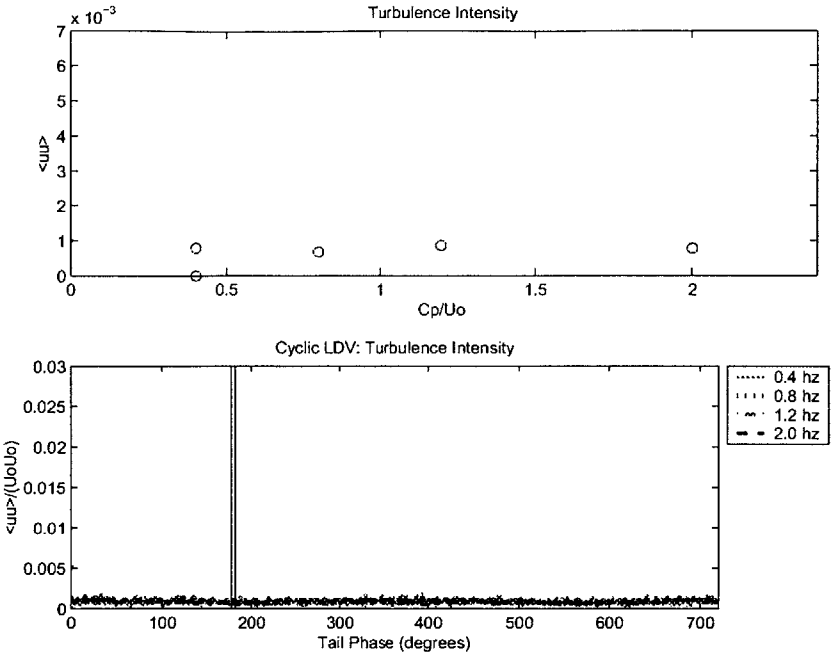

Figure A-33: Turbulence intensity for piston five crest position at a distance of 58 mm away from the snake body.

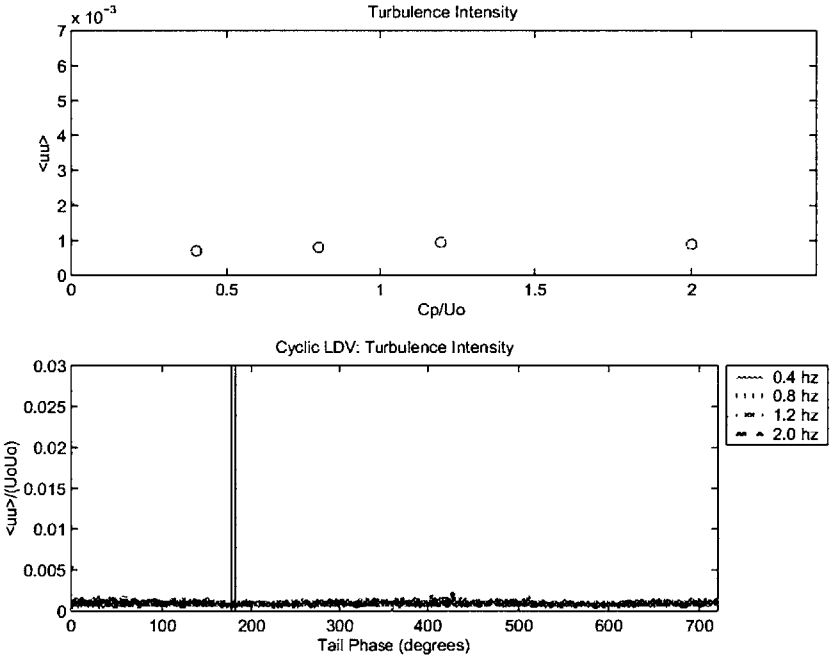

Figure A-34: Turbulence intensity for piston five crest position at a distance of 63 mm away from the snake body.

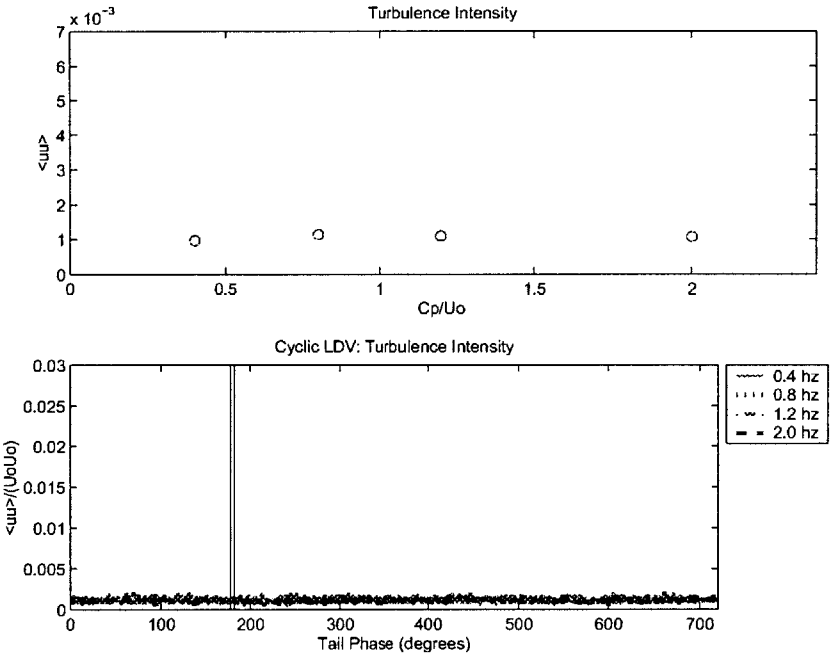

Figure A-35: Turbulence intensity for piston five crest position at a distance of 88 mm away from the snake body.

Appendix B

Turbulence Levels for Piston Six

This appendix includes the data for all of the distances where turbulence intensity was measured at the piston six location. For each $\frac{C_P}{U_o}$ value, two plots are shown. The top plot shows the average turbulence intensity at four values of $\frac{C_P}{U_o}$. The lower plot shows the turbulence intensity measured over 360 degrees, with two cycles being shown. Trough and crest data are shown in separate figures. The figures are organized first by position, trough and then crest, and then by distance from the snake body.

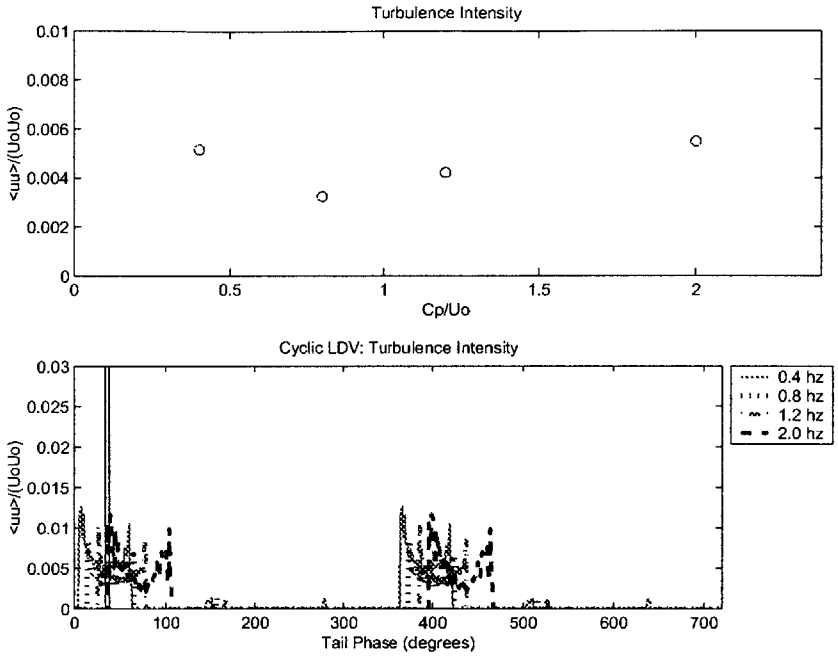

Figure B-1: Turbulence intensity for piston six trough position at a distance of 2 mm away from the snake body.

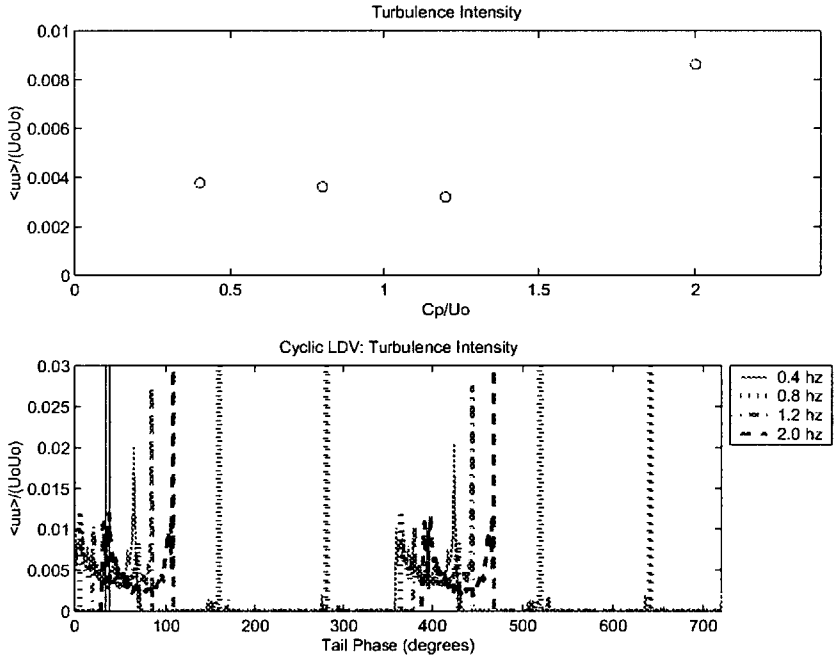

Figure B-2: Turbulence intensity for piston six trough position at a distance of 4 mm away from the snake body.

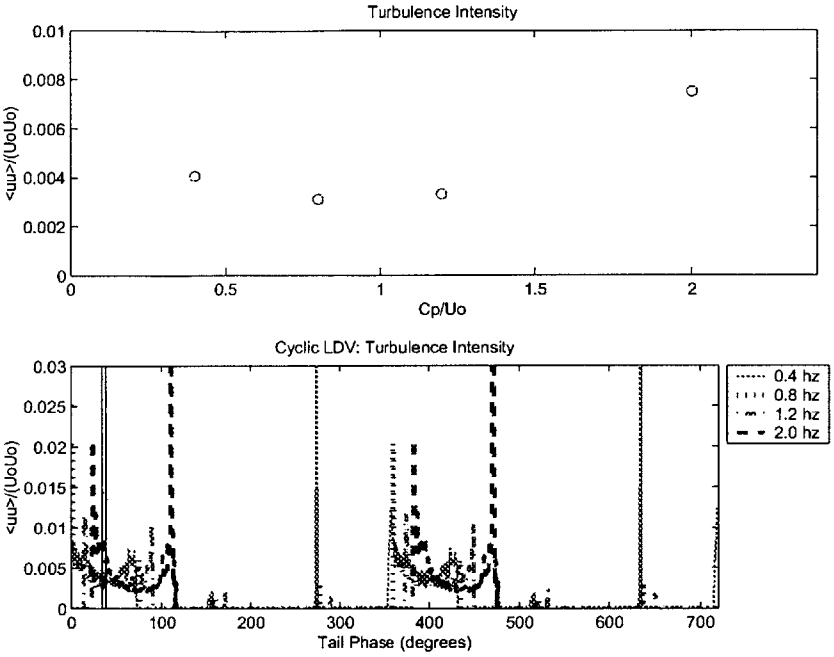

Figure B-3: Turbulence intensity for piston six trough position at a distance of 6 mm away from the snake body.

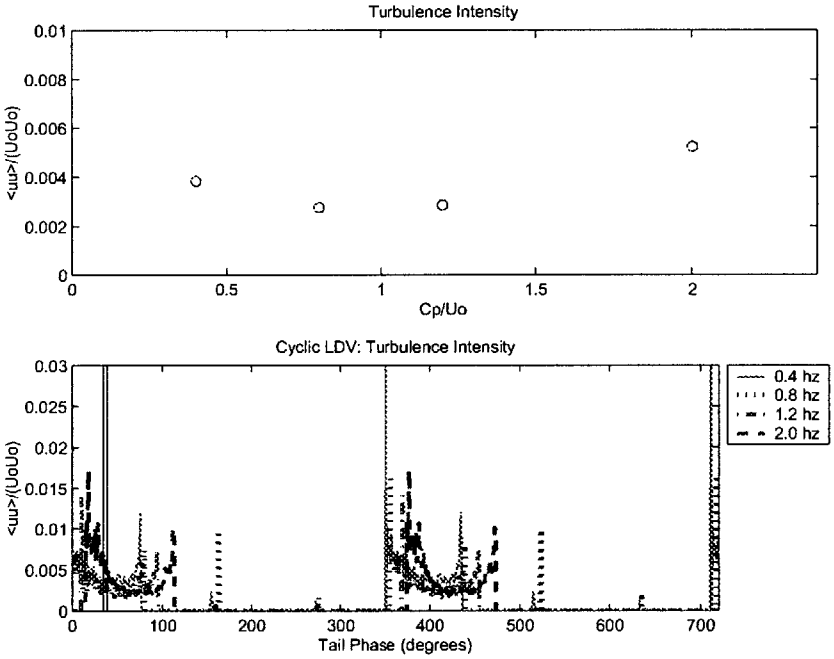

Figure B-4: Turbulence intensity for piston six trough position at a distance of 8 mm away from the snake body.

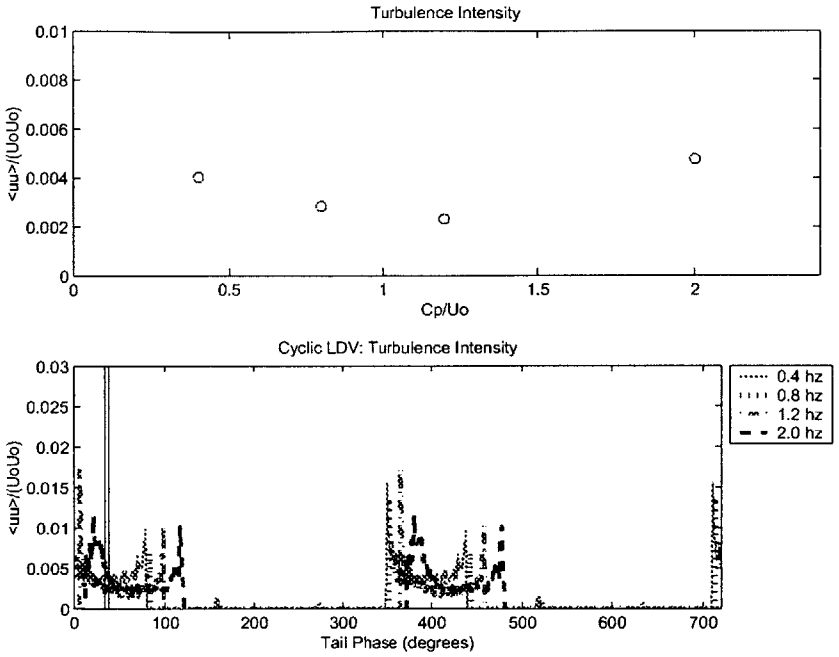

Figure B-5: Turbulence intensity for piston six trough position at a distance of 10 mm away from the snake body.

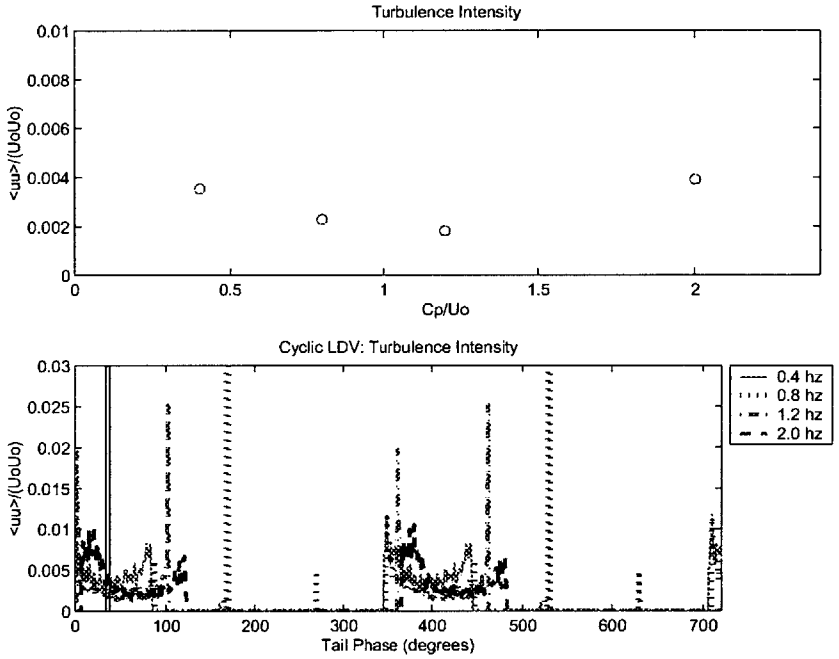

Figure B-6: Turbulence intensity for piston six trough position at a distance of 12 mm away from the snake body.

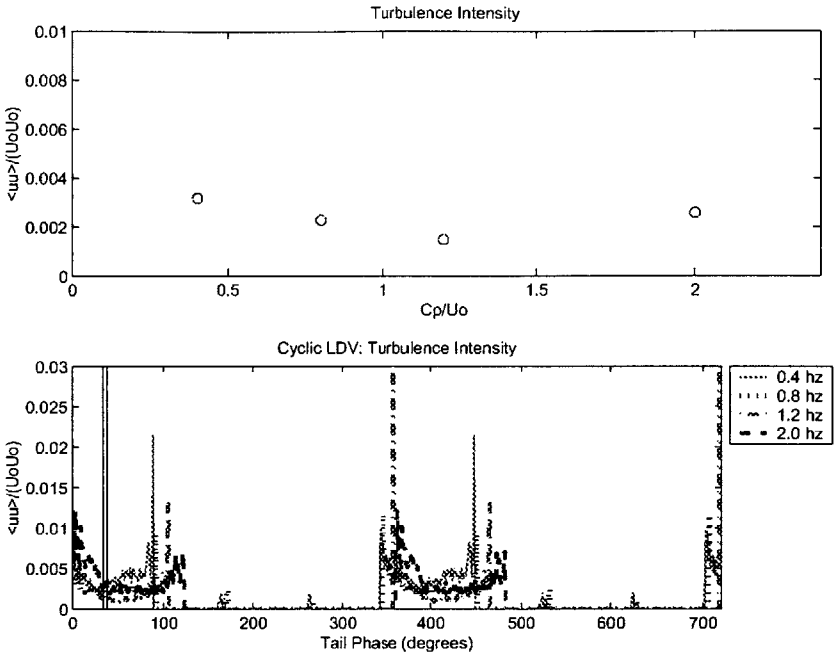

Figure B-7: Turbulence intensity for piston six trough position at a distance of 14 mm away from the snake body.

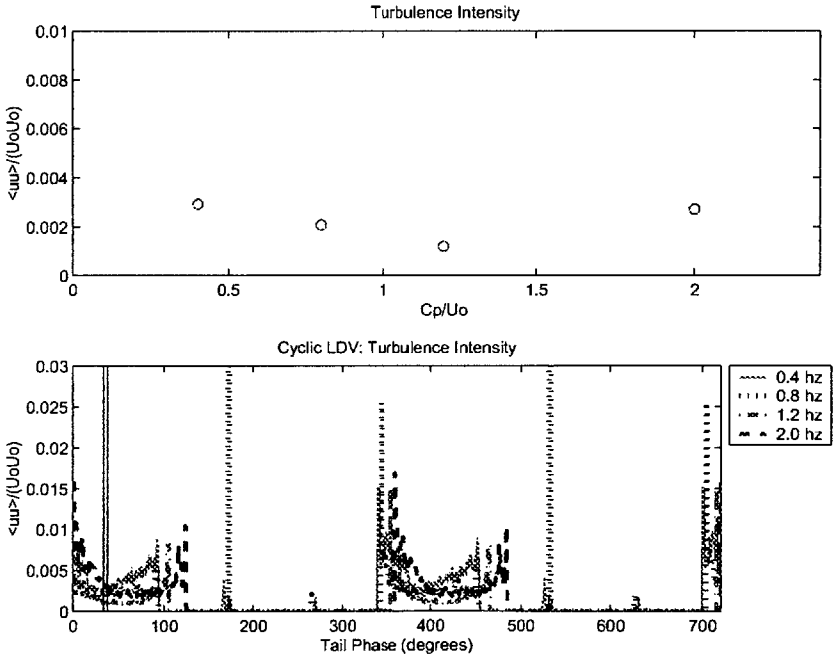

Figure B-8: Turbulence intensity for piston six trough position at a distance of 15 mm away from the snake body.

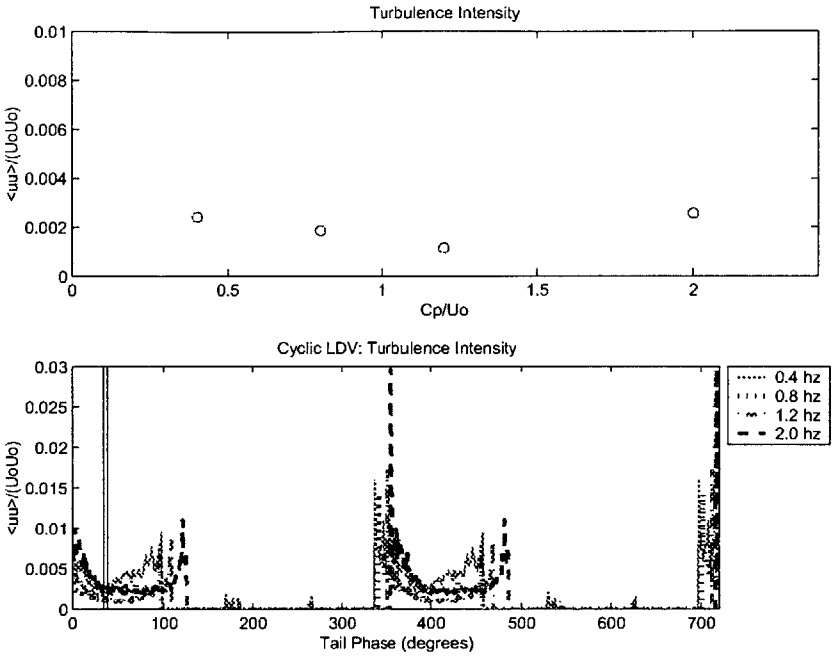

Figure B-9: Turbulence intensity for piston six trough position at a distance of 17 mm away from the snake body.

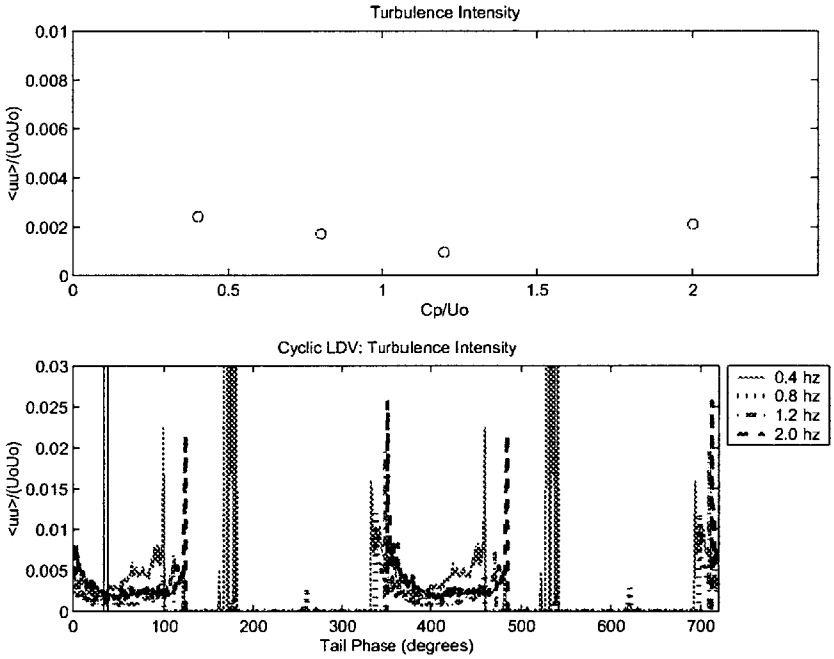

Figure B-10: Turbulence intensity for piston six trough position at a distance of 19 mm away from the snake body.

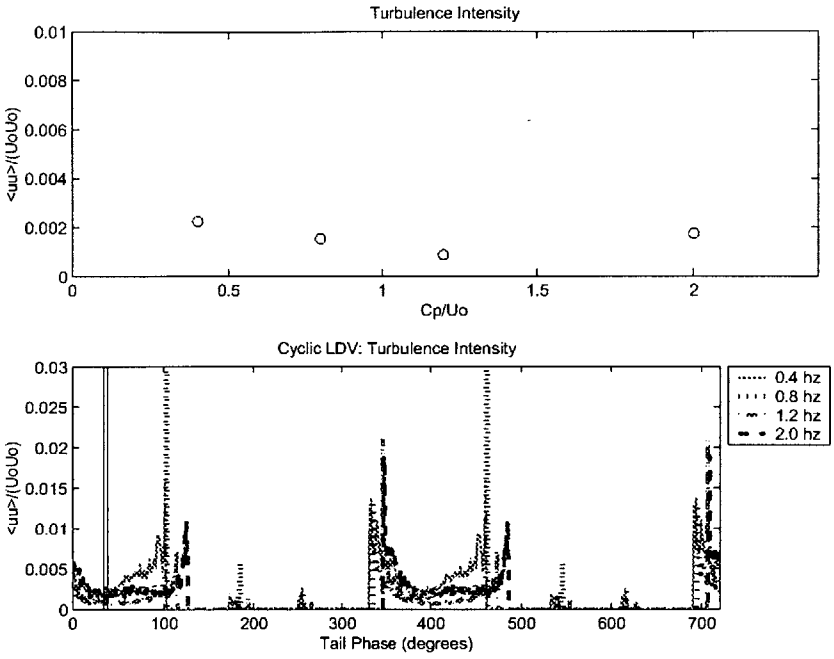

Figure B-11: Turbulence intensity for piston six trough position at a distance of 21 mm away from the snake body.

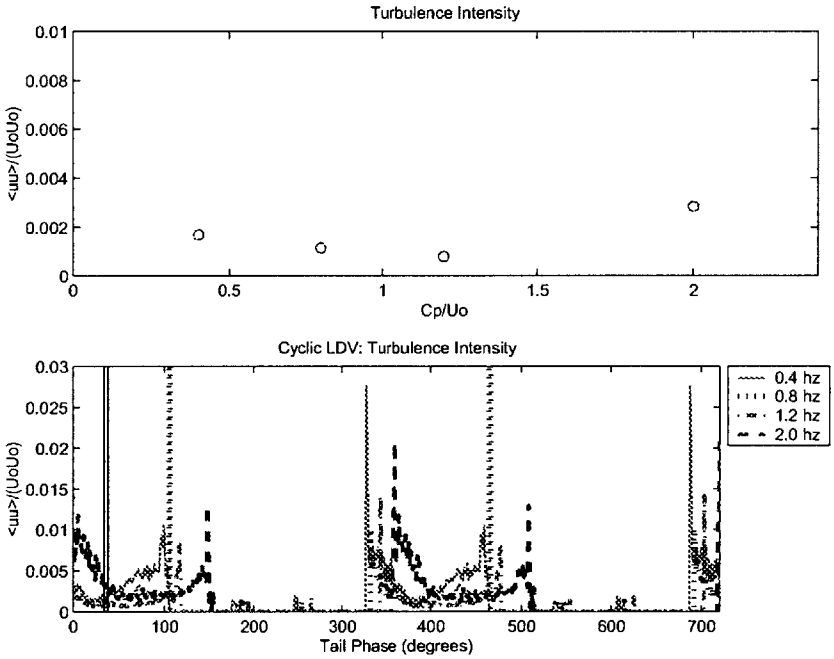

Figure B-12: Turbulence intensity for piston six trough position at a distance of 23 mm away from the snake body.

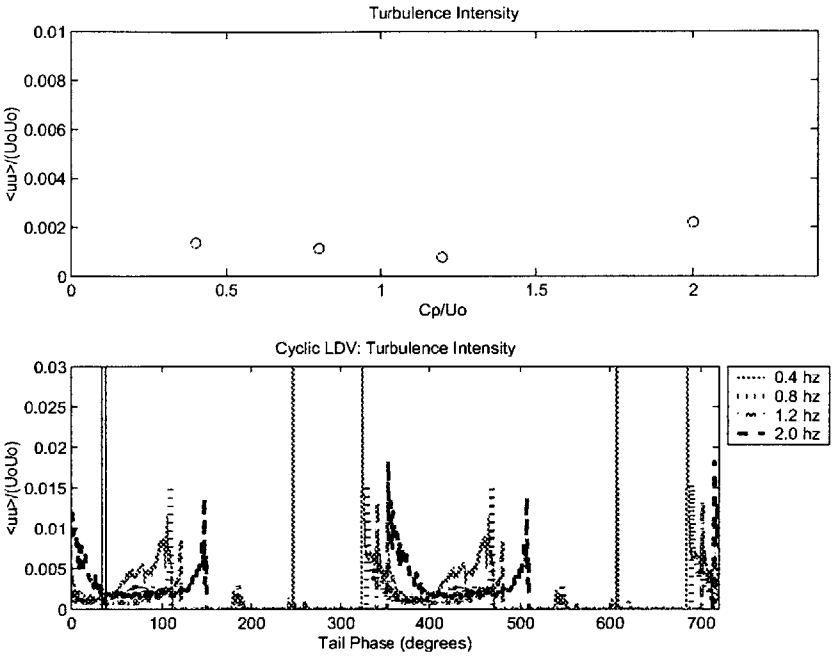

Figure B-13: Turbulence intensity for piston six trough position at a distance of 25 mm away from the snake body.

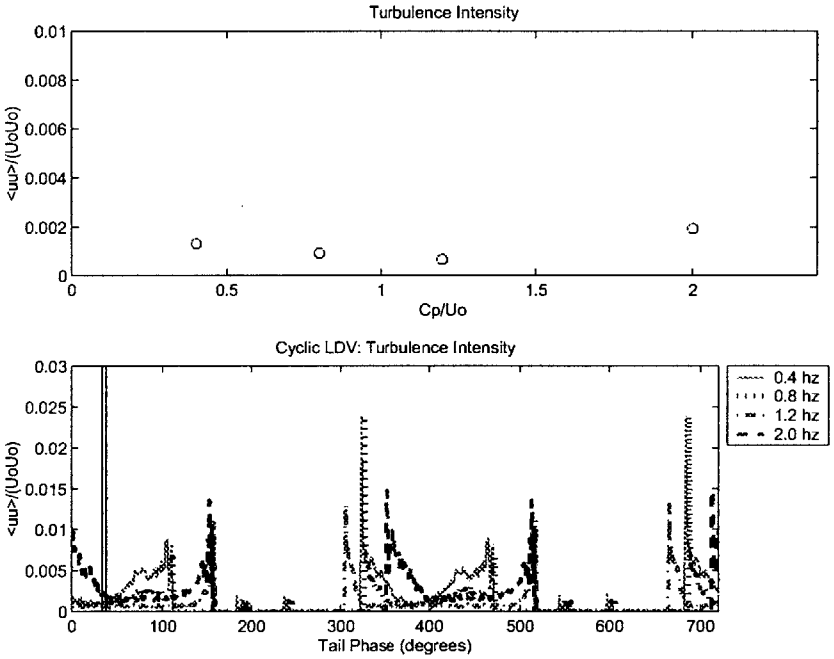

Figure B-14: Turbulence intensity for piston six trough position at a distance of 27 mm away from the snake body.

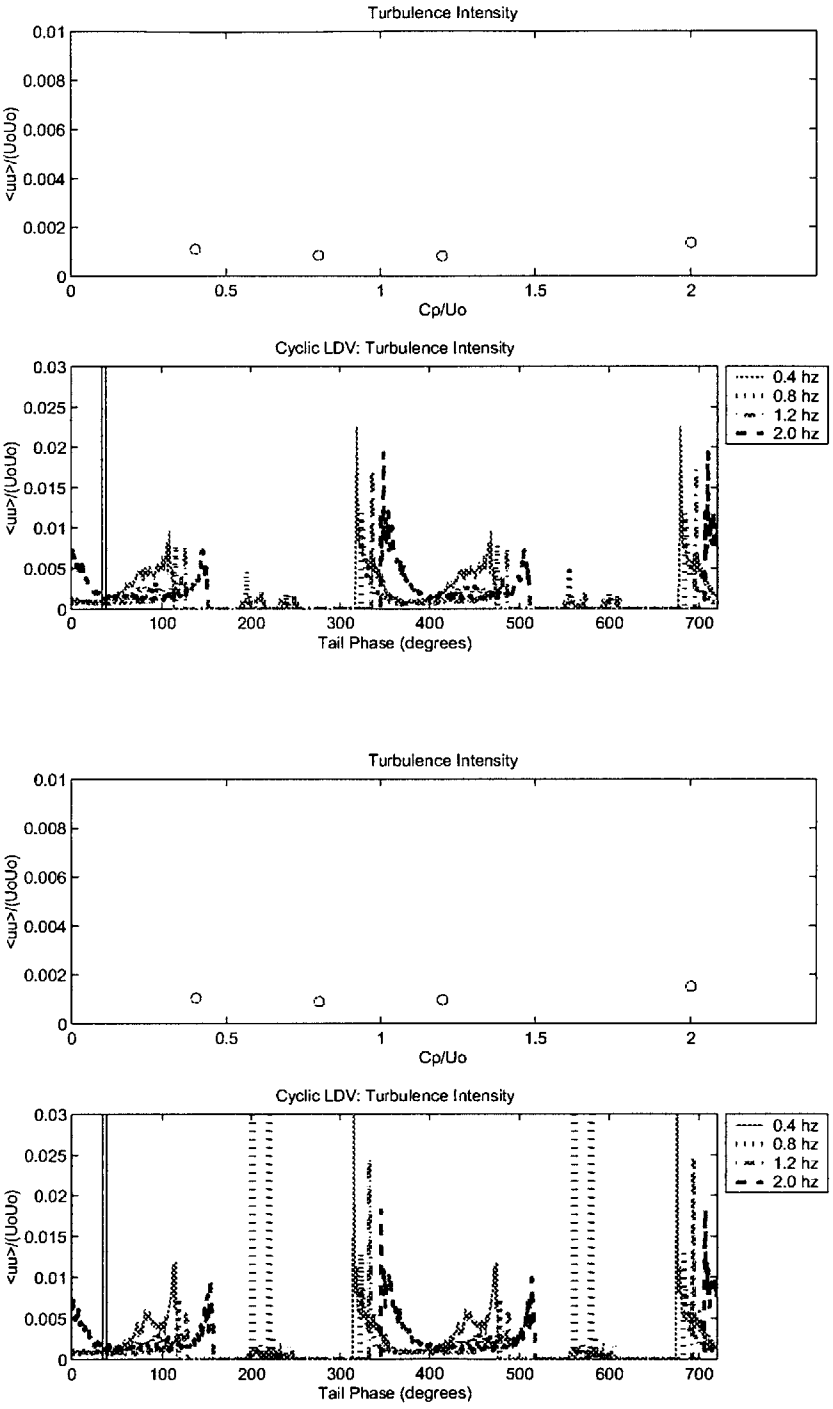

Figure B-15: Turbulence intensity for piston six trough position at a distance of 29 mm away from the snake body.

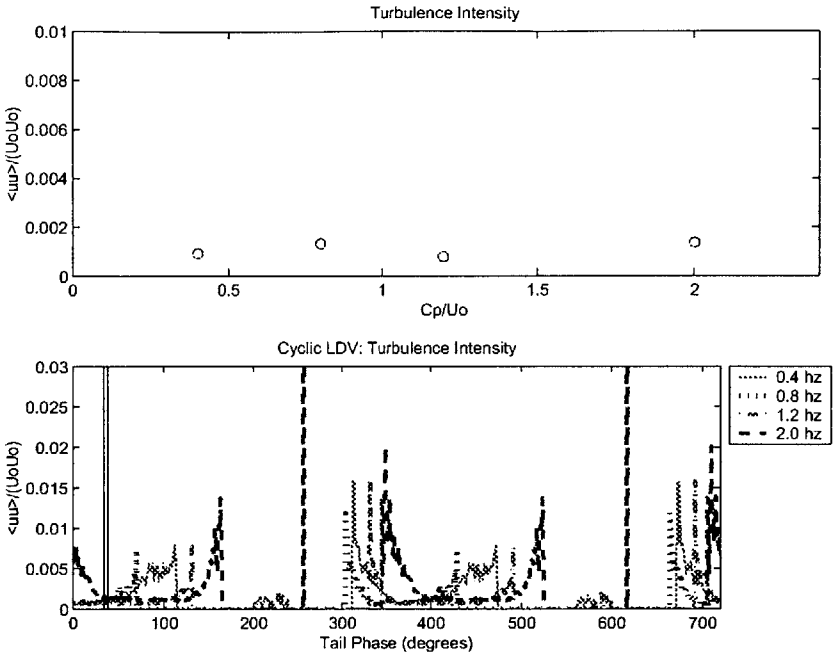

Figure B-16: Turbulence intensity for piston six trough position at a distance of 31 mm away from the snake body.

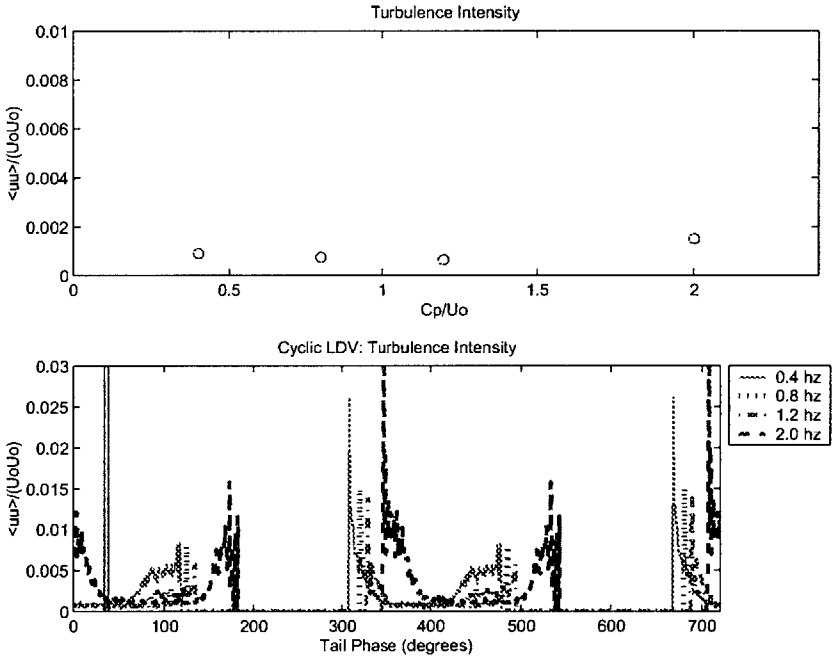

Figure B-17: Turbulence intensity for piston six trough position at a distance of 35 mm away from the snake body.

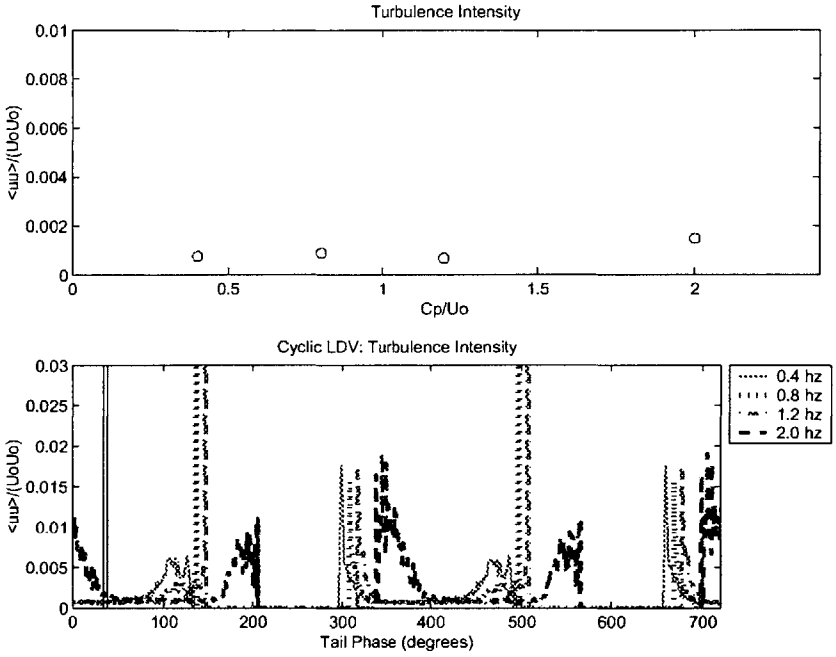

Figure B-18: Turbulence intensity for piston six trough position at a distance of 45 mm away from the snake body.

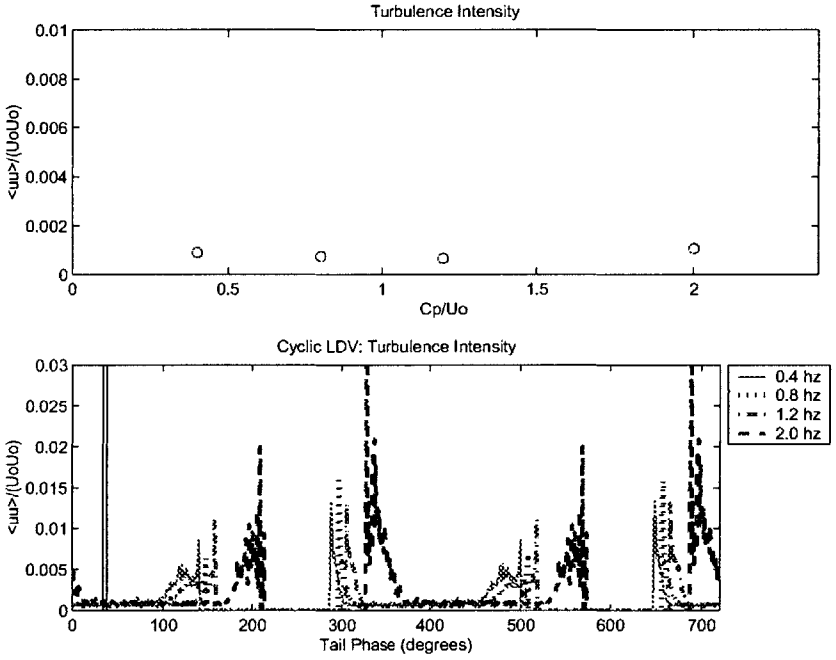

Figure B-19: Turbulence intensity for piston six trough position at a distance of 55 mm away from the snake body.

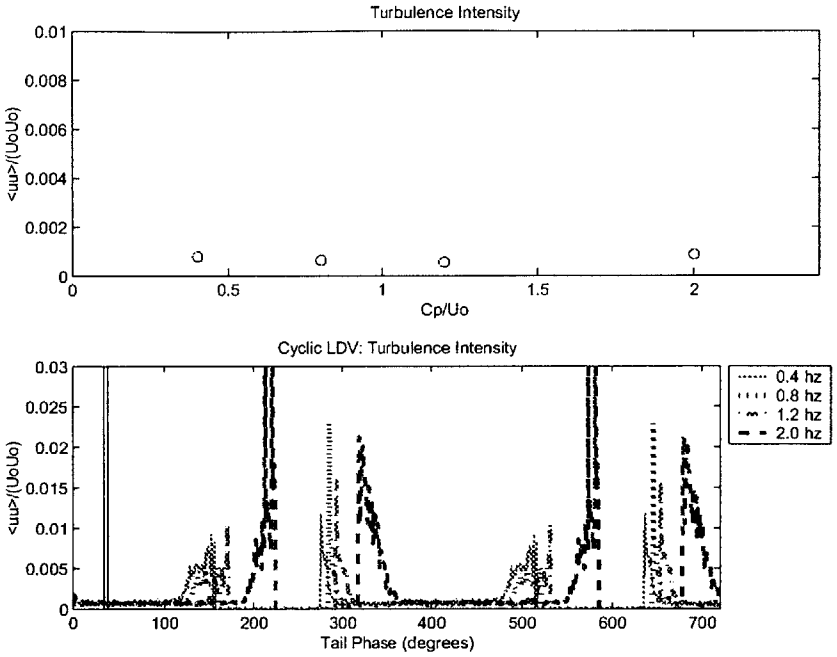

Figure B-20: Turbulence intensity for piston six trough position at a distance of 65 mm away from the snake body.

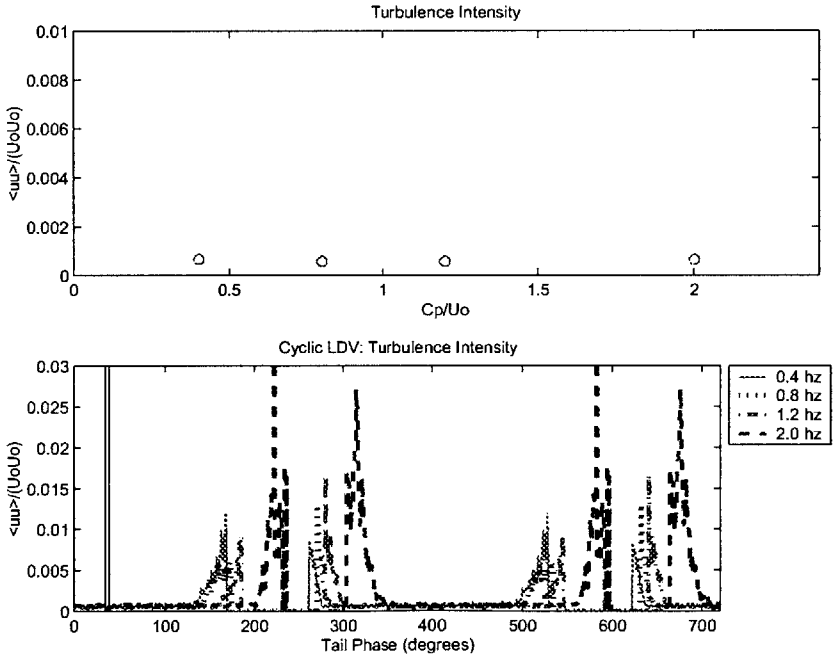

Figure B-21: Turbulence intensity for piston six trough position at a distance of 75 mm away from the snake body.

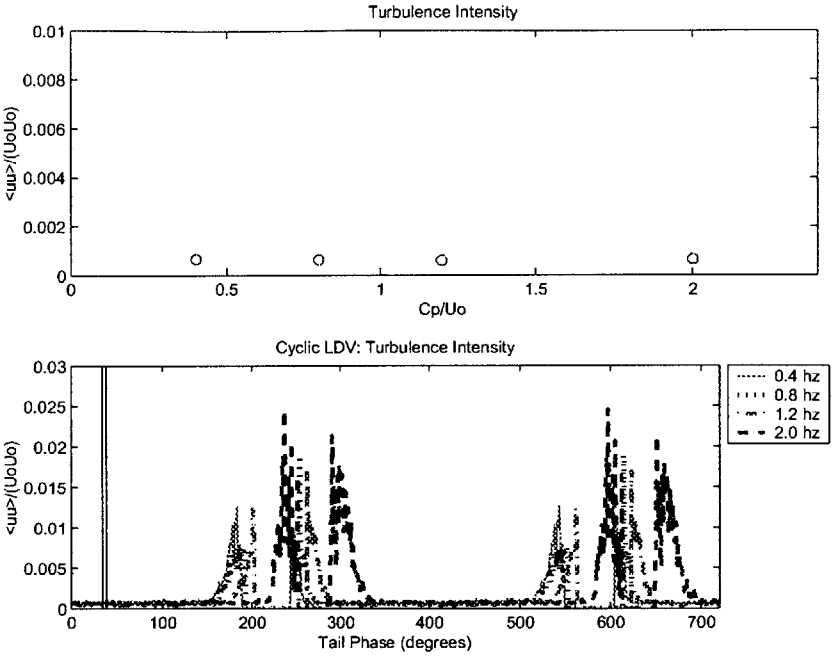

Figure B-22: Turbulence intensity for piston six trough position at a distance of 85 mm away from the snake body.

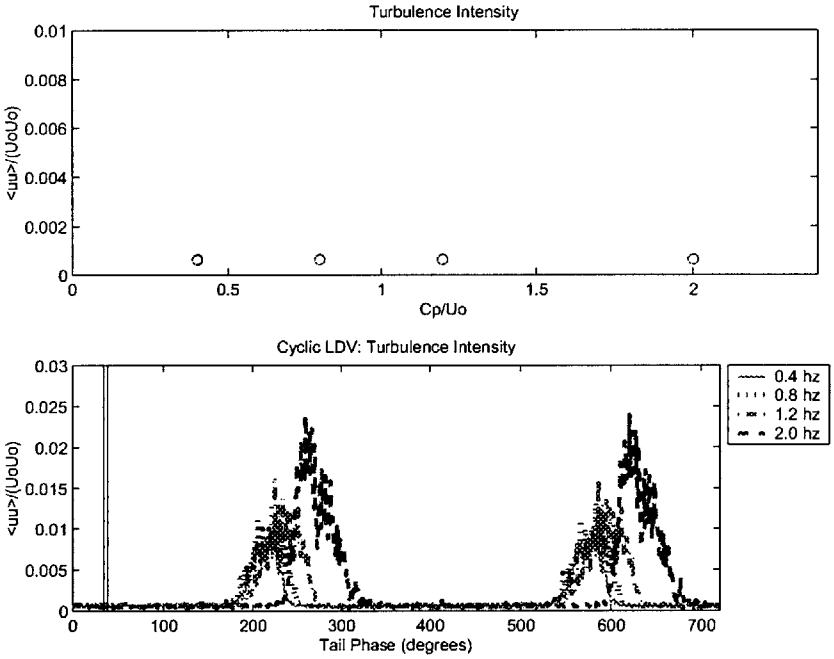

Figure B-23: Turbulence intensity for piston six trough position at a distance of 93 mm away from the snake body.

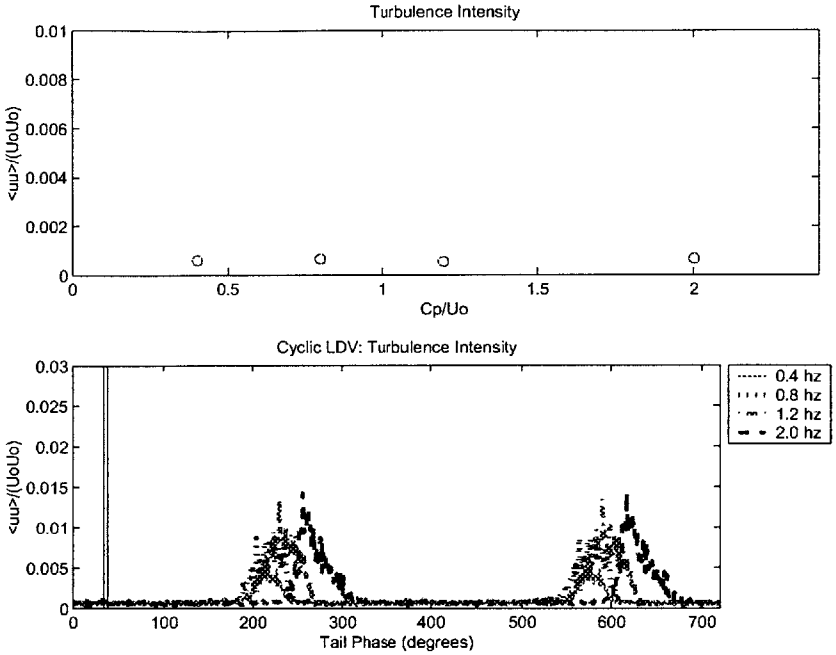

Figure B-24: Turbulence intensity for piston six trough position at a distance of 95 mm away from the snake body.

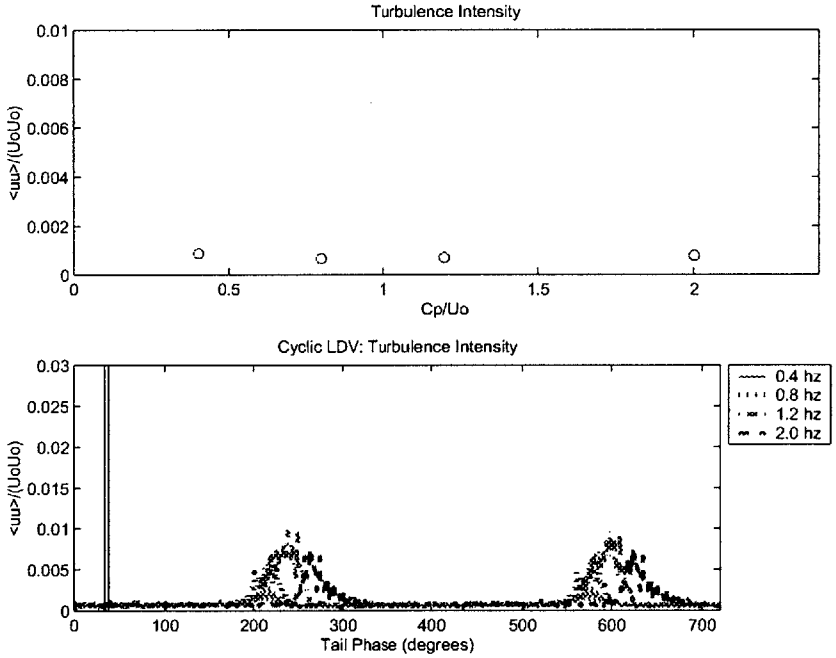

Figure B-25: Turbulence intensity for piston six trough position at a distance of 97 mm away from the snake body.

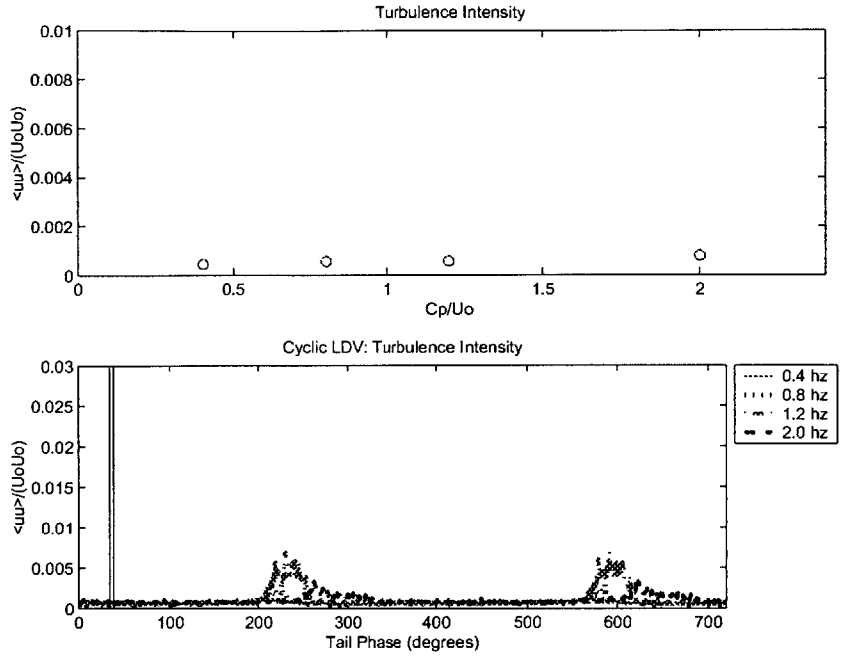

Figure B-26: Turbulence intensity for piston six trough position at a distance of 99 mm away from the snake body.

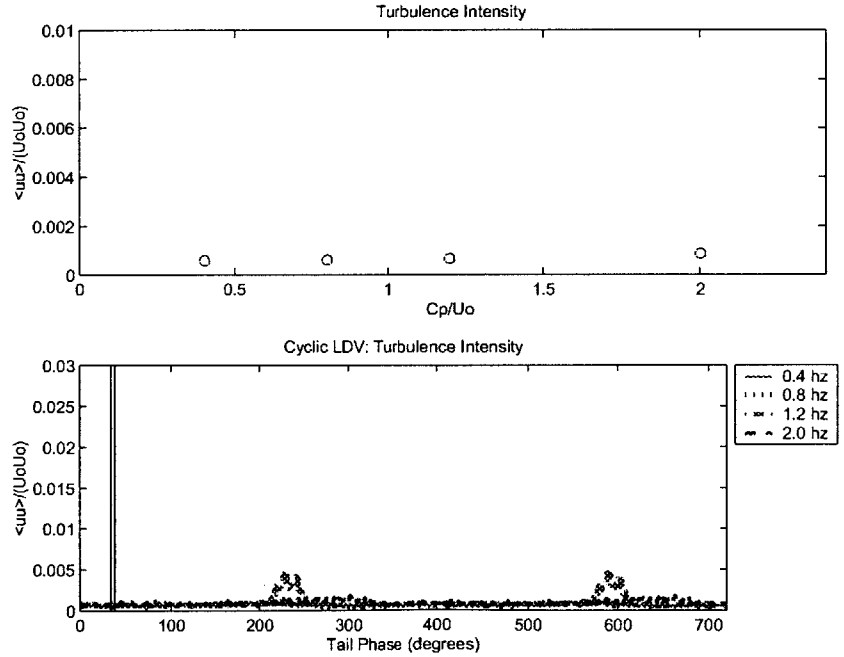

Figure B-27: Turbulence intensity for piston six trough position at a distance of 101 mm away from the snake body.

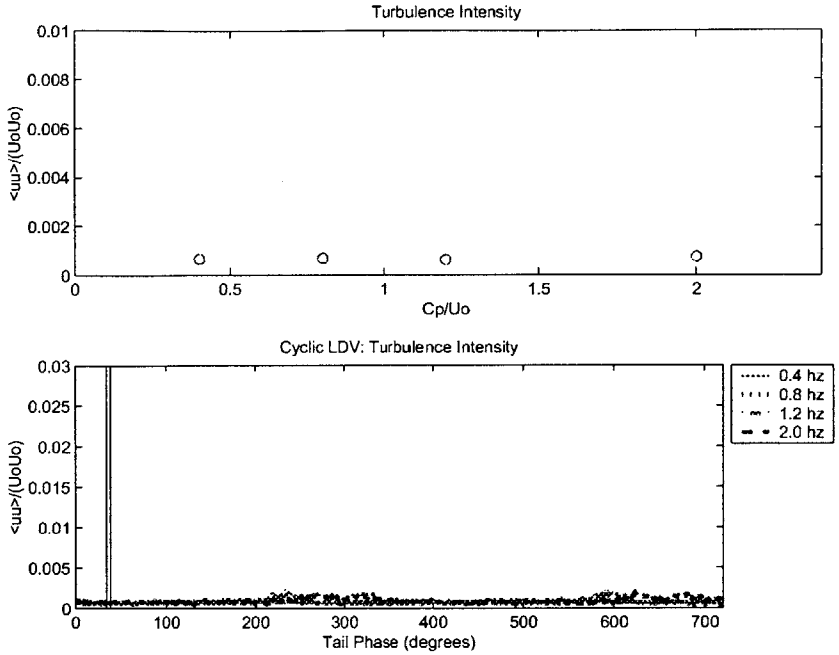

Figure B-28: Turbulence intensity for piston six trough position at a distance of 103 mm away from the snake body.

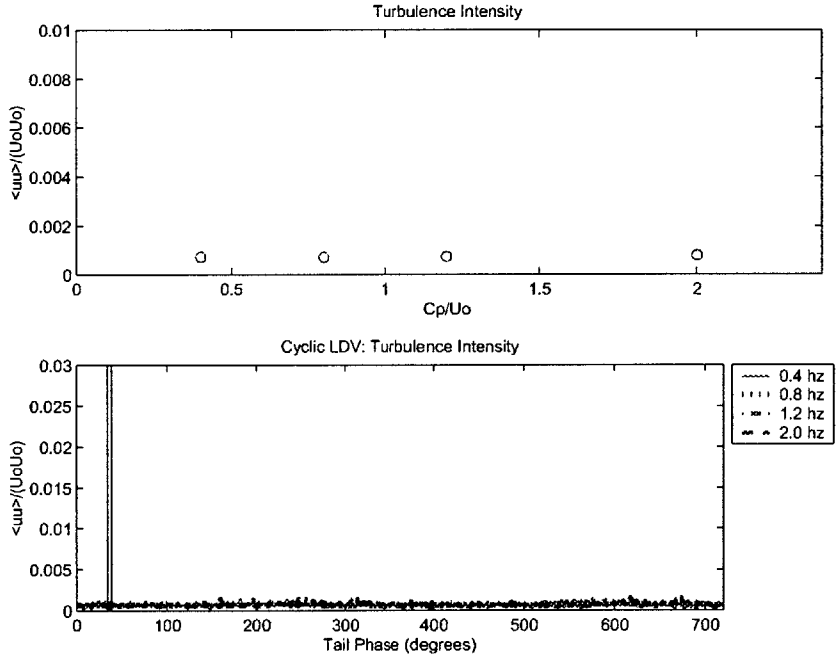

Figure B-29: Turbulence intensity for piston six trough position at a distance of 105 mm away from the snake body.

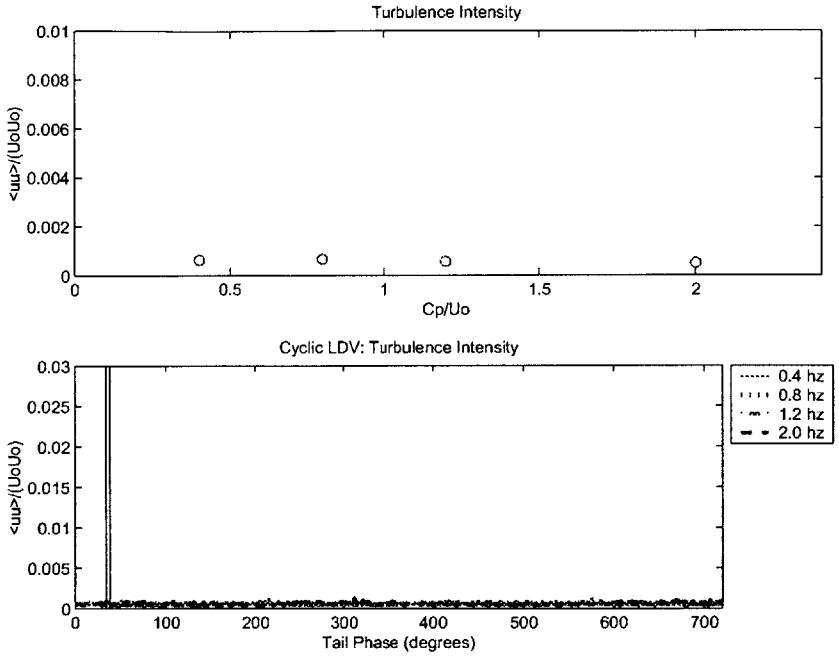

Figure B-30: Turbulence intensity for piston six trough position at a distance of 110 mm away from the snake body.

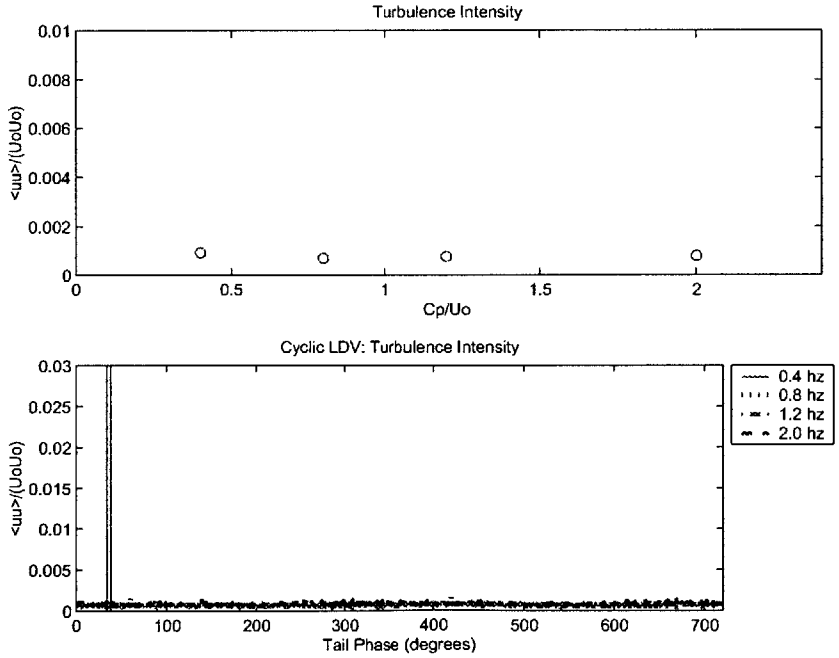

Figure B-31: Turbulence intensity for piston six trough position at a distance of 120 mm away from the snake body.

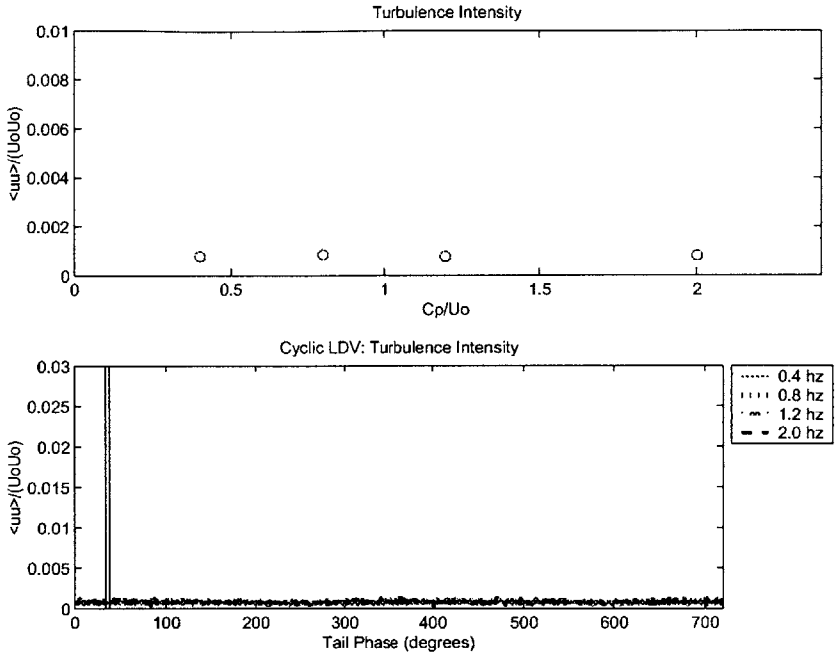

Figure B-32: Turbulence intensity for piston six trough position at a distance of 125 mm away from the snake body.

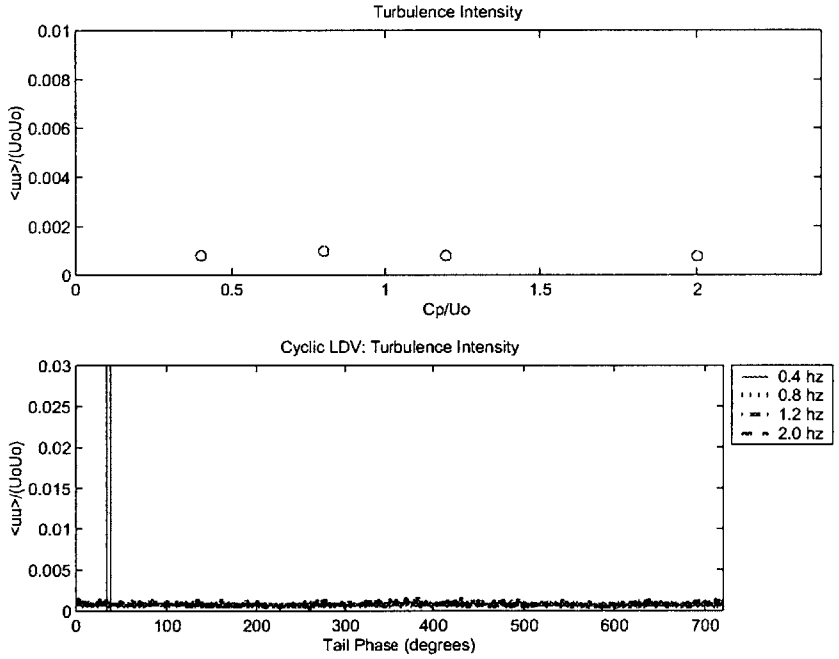

Figure B-33: Turbulence intensity for piston six trough position at a distance of 130 mm away from the snake body.

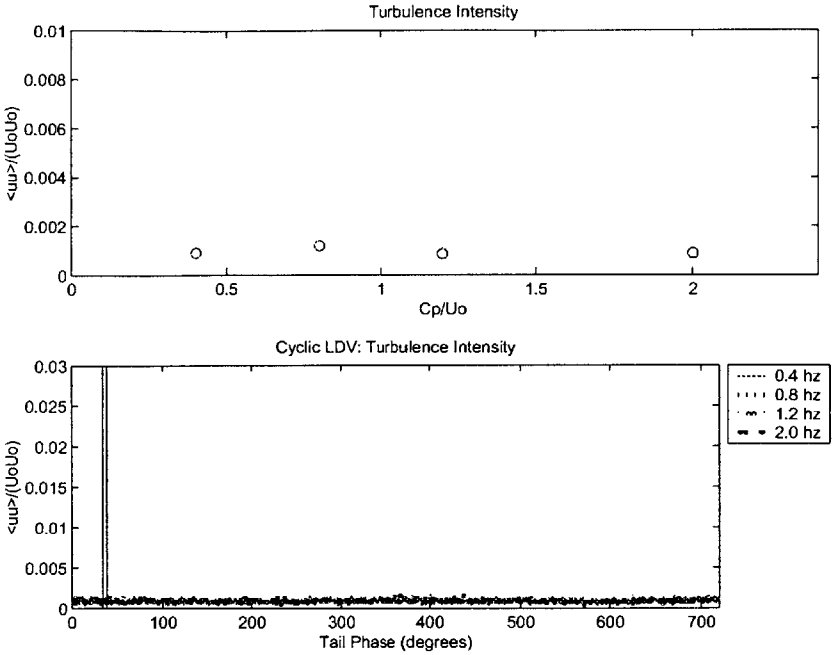

Figure B-34: Turbulence intensity for piston six trough position at a distance of 135 mm away from the snake body.

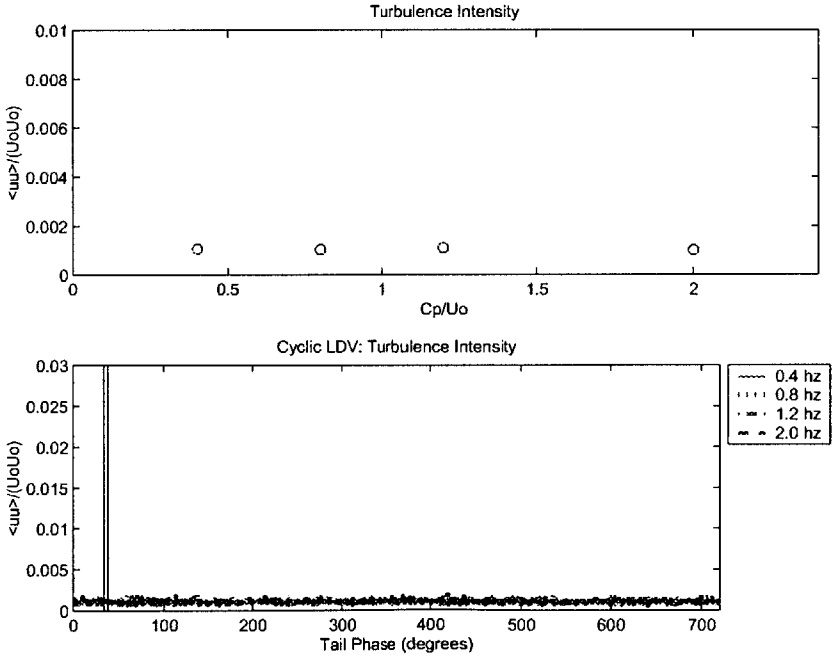

Figure B-35: Turbulence intensity for piston six trough position at a distance of 160 mm away from the snake body.

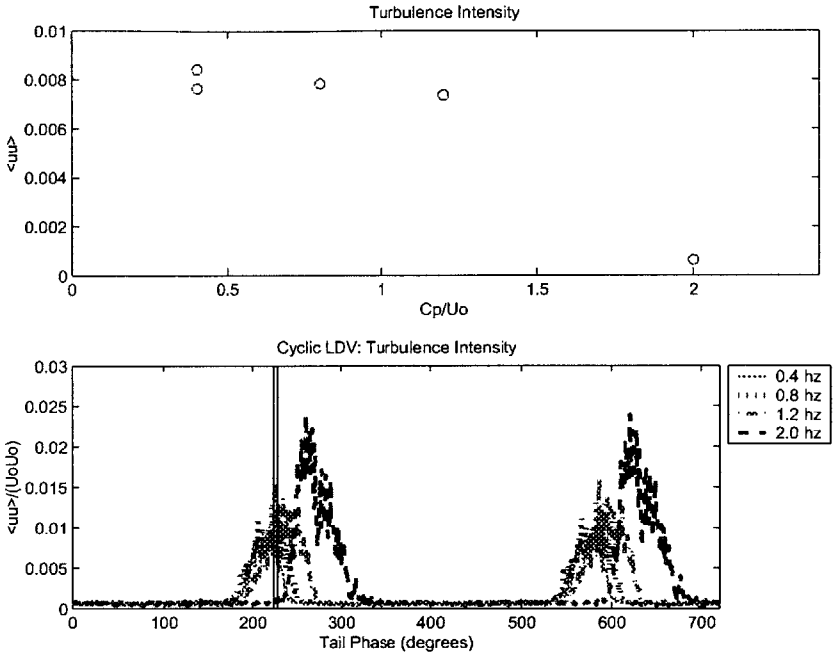

Figure B-36: Turbulence intensity for piston six crest position at a distance of 6 mm away from the snake body.

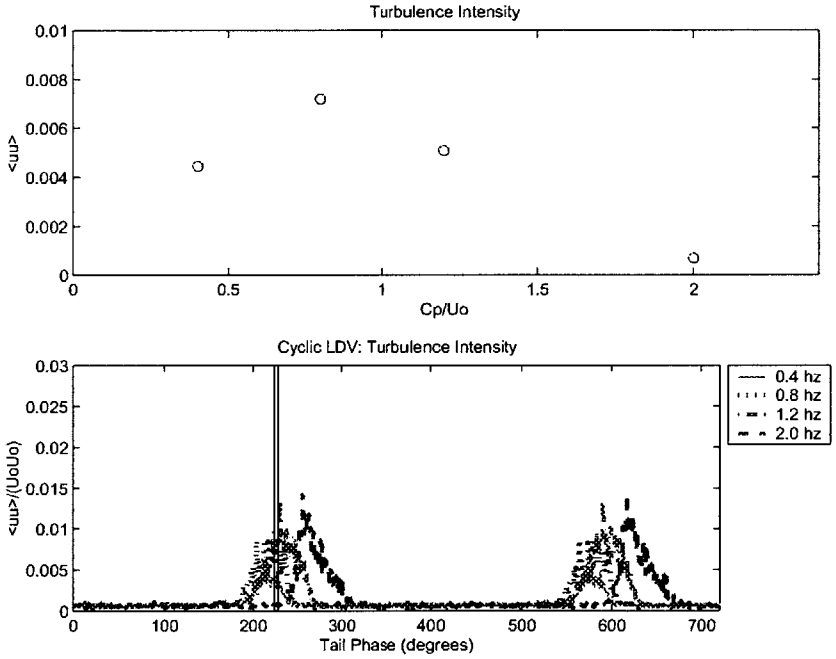

Figure B-37: Turbulence intensity for piston six crest position at a distance of 8 mm away from the snake body.

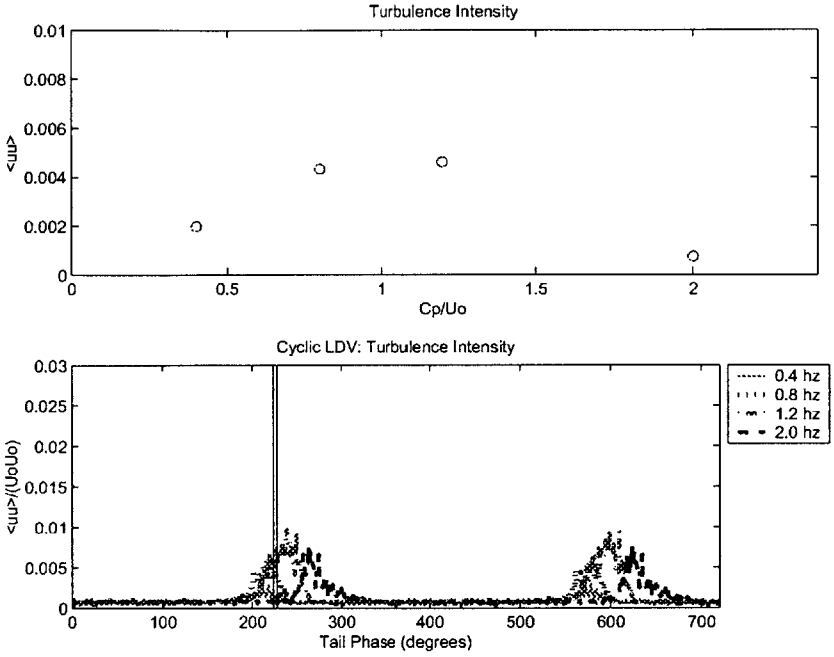

Figure B-38: Turbulence intensity for piston six crest position at a distance of 10 mm away from the snake body.

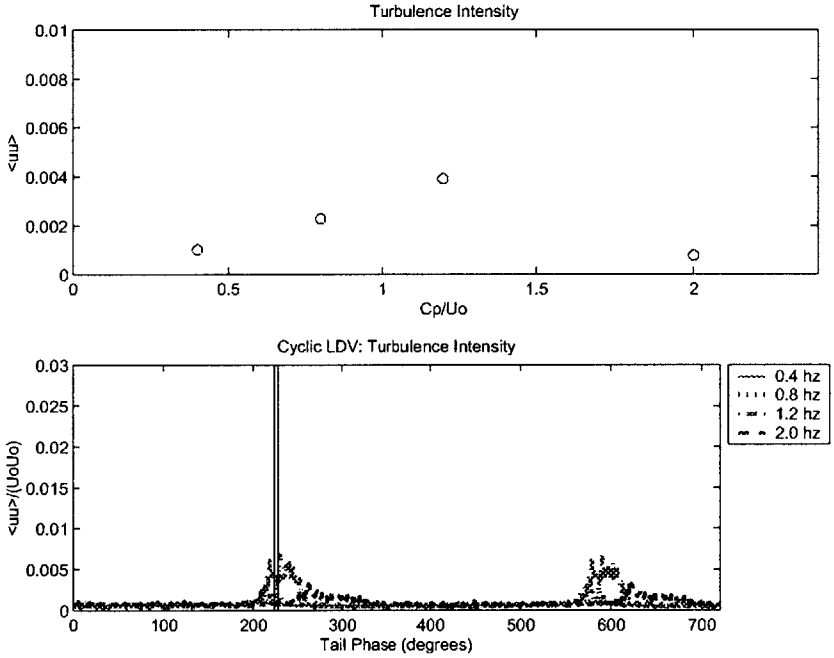

Figure B-39: Turbulence intensity for piston six crest position at a distance of 12 mm away from the snake body.

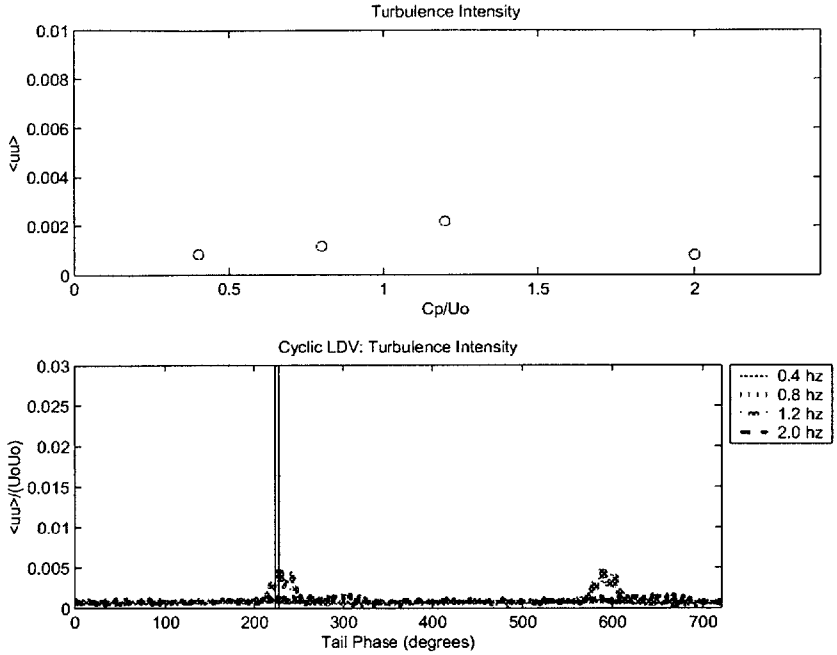

Figure B-40: Turbulence intensity for piston six crest position at a distance of 14 mm away from the snake body.

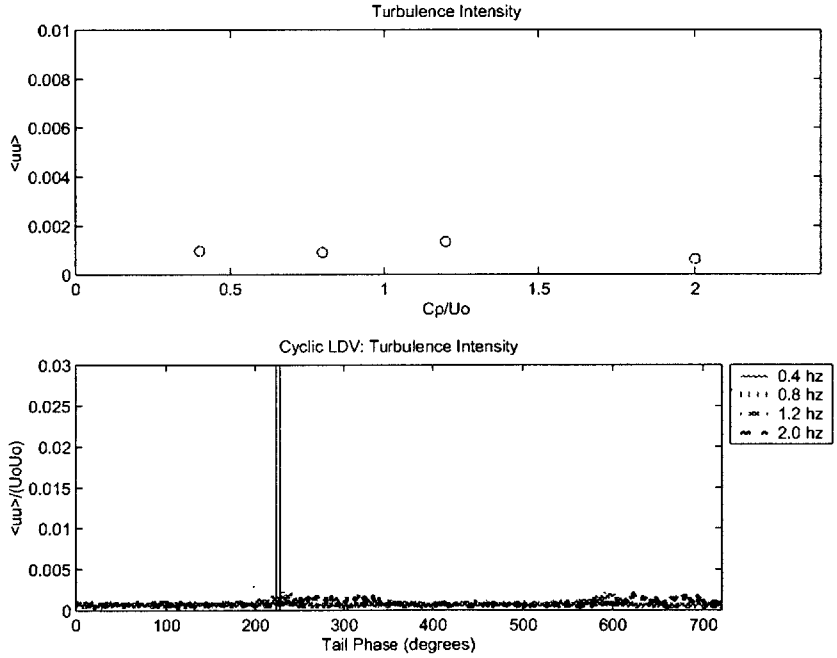

Figure B-41: Turbulence intensity for piston six crest position at a distance of 16 mm away from the snake body.

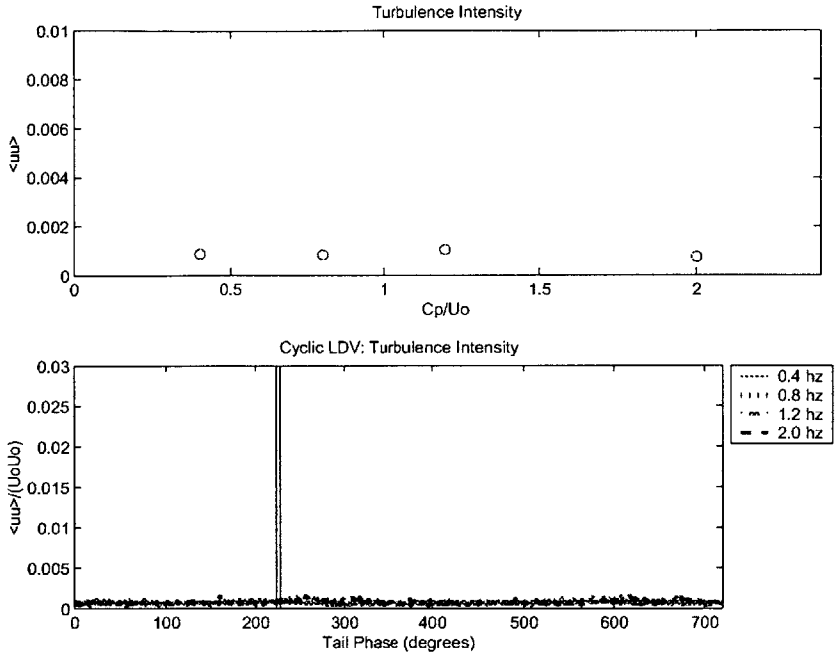

Figure B-42: Turbulence intensity for piston six crest position at a distance of 18 mm away from the snake body.

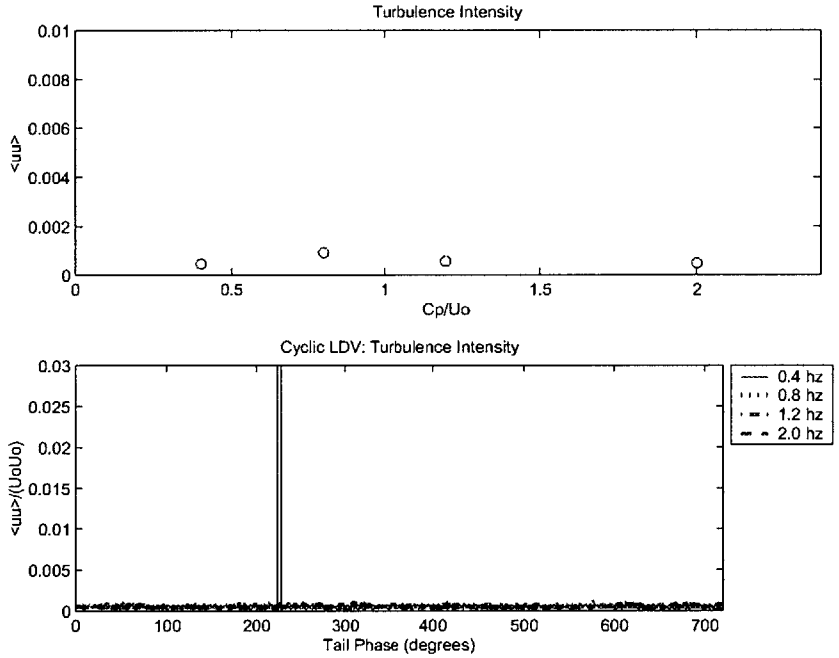

Figure B-43: Turbulence intensity for piston six crest position at a distance of 23 mm away from the snake body.

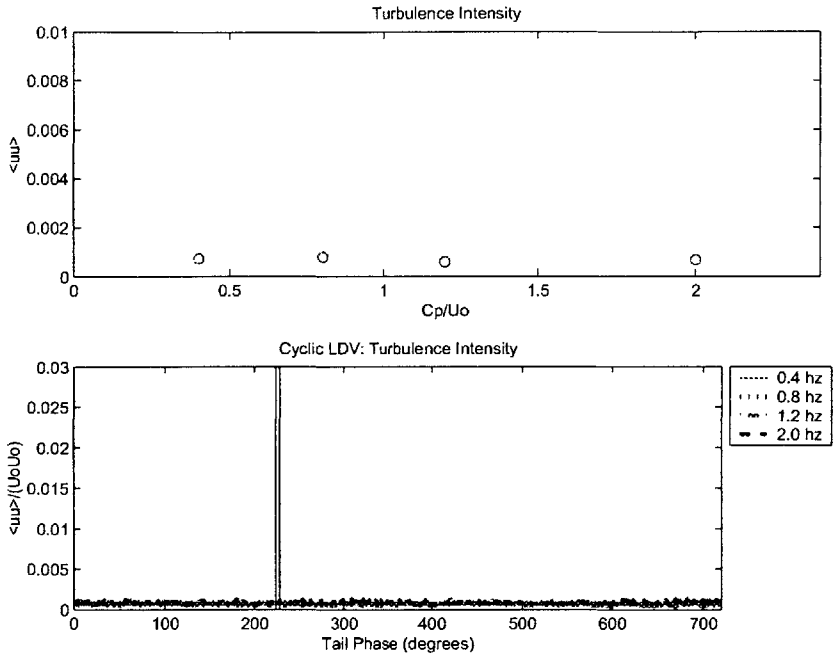

Figure B-44: Turbulence intensity for piston six crest position at a distance of 33 mm away from the snake body.

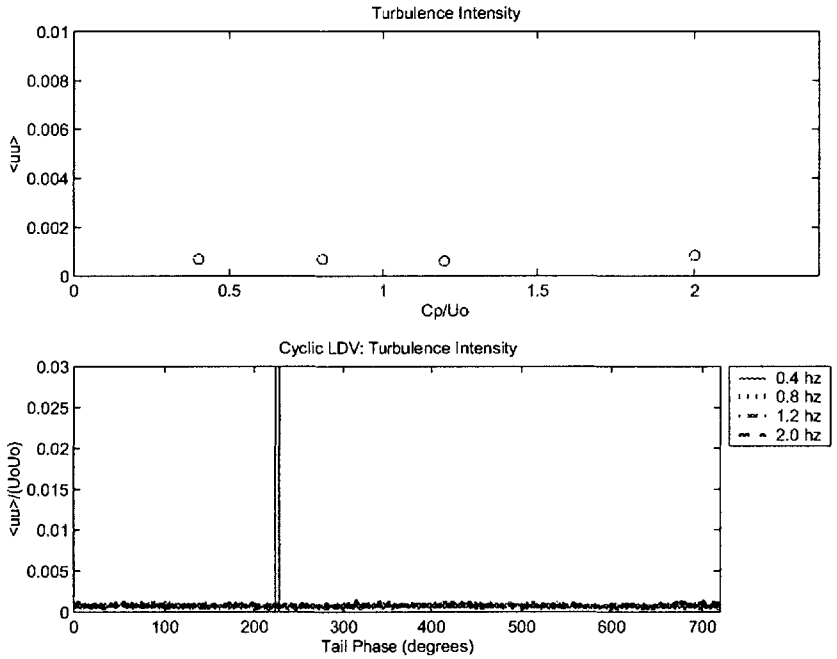

Figure B-45: Turbulence intensity for piston six crest position at a distance of 38 mm away from the snake body.

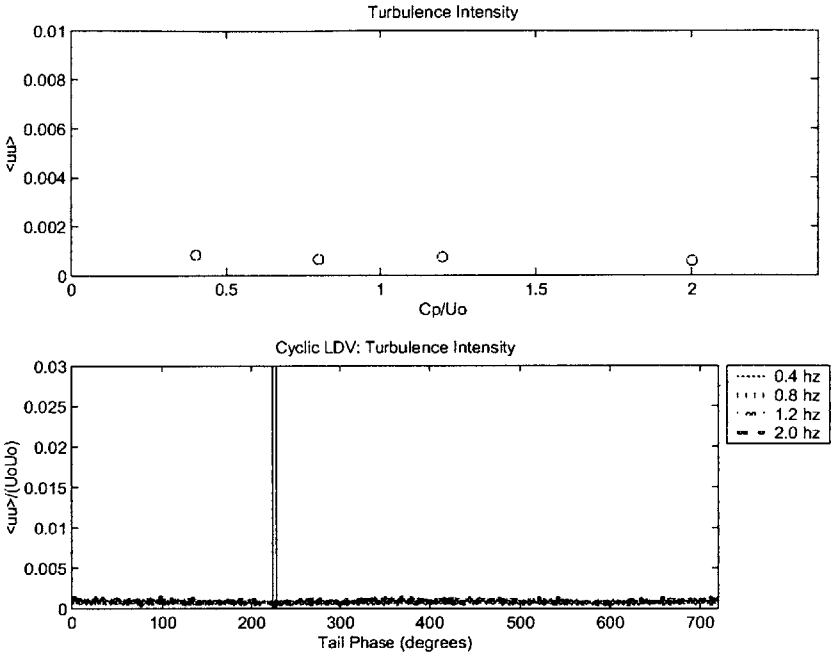

Figure B-46: Turbulence intensity for piston six crest position at a distance of 43 mm away from the snake body.

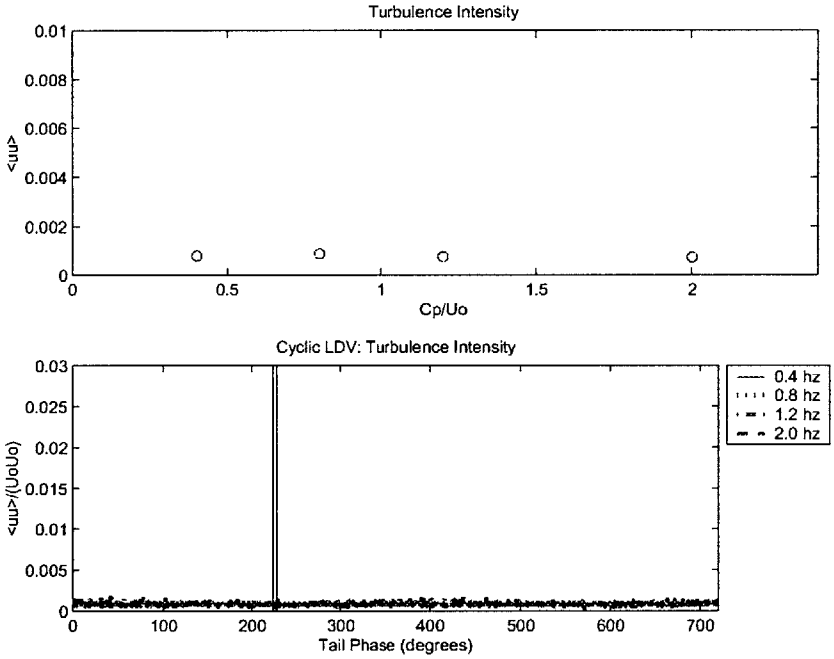

Figure B-47: Turbulence intensity for piston six crest position at a distance of 48 mm away from the snake body.

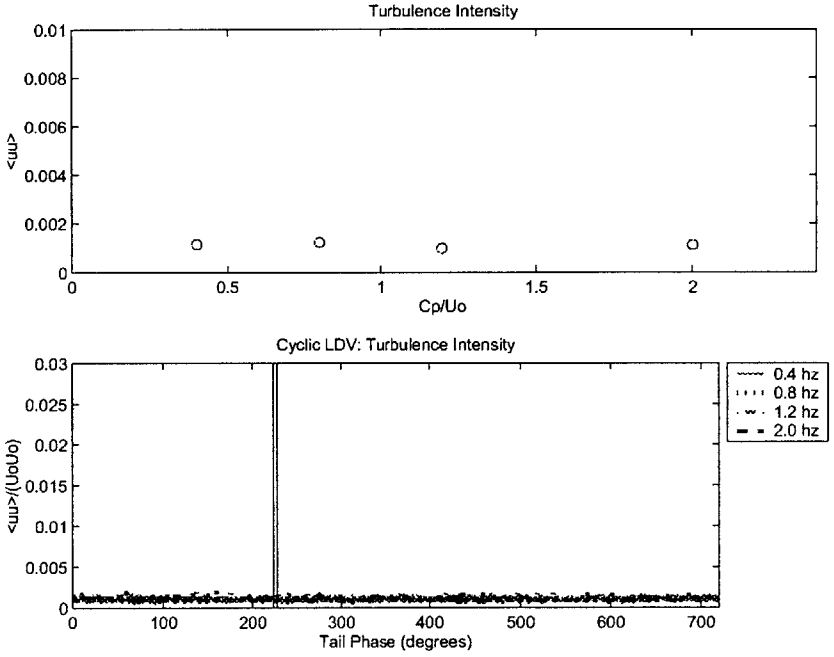

Figure B-48: Turbulence intensity for piston six crest position at a distance of 73 mm away from the snake body.

Bibliography

[1] Kiel probes. *United Sensor Corp. Technical Literature.*

[2] Smoothon. *Smoothon Technical Literature.*

[3] A. Azuma. *The Biokinetics of Flying and Swimming.* Springer-Verlag, New York, 1992.

[4] A.L. Batcheller and R.W. Kimball. *A procedure for the calibration of pressure transducers.* 1999.

[5] J. Cheng, L. Zhuang, and B. Tong. Analysis of swimming of three-dimensional waving plates. *J. Fluid Mech.*, 232:341–355, 1991.

[6] W.A. Dunson. *The Biology of Sea Snakes.* University Park Press, Baltimore, MD, 1975.

[7] G. Gillis. Undulatory locomotion in elongate aquatic vertebrates: anguilliform swimming since sir james gray. *American Zoologist*, 36:656–665, 1996.

[8] J.B. Graham and W.R. Lowell. Surface and subsurface swimming of the sea snake *Pelamis platurus*. *J. Expt. Bio.*, 127:27–44, 1987.

[9] H. Heatwole. *Sea Snakes.* Krieger Publishing Company, Malabar, FL, 1999.

[10] R.W. Kimball. *Experimental investigations and numerical modelling of a mixed flow marine waterjet.* PhD dissertation, Massachusetts Institute of Technology, Department of Ocean Engineering, 2001.

[11] J. Lighthill. Hydromechanics of aquatic animal propulsion–a survey. *Annual Review of Fluid Mechanics*, 1:413–446, 1969.

[12] J. Lighthill. Aquatic animal propulsion of high hydromechanical efficiency. *J. Fluid Mech.*, 44:265–301, 1970.

[13] D. K. P. Yue M. S. Triantafyllou, G. S. Triantafyllou. *Annual Rev. Fluid Mech.*, 2000.

[14] D.M. Lane M. Sfakiotakis and J.B.C. Davies. Review of fish swimming modes for aquatic locomotion. *IEEE Journal of Oceanic Engineering*, 24:237–252, 1999.

[15] M. Sommerfeld and C. Tropea. Single-point laser measurement. *Instrumentation for Fluid-Particle Flow*, pages 252–317, 1999.

[16] S. Taneda and Y. Tomonari. An experiment on the flow around a waving plate. *Journal of the Physical Society of Japan*, 36(6):1683–1689, 1974.

[17] A.H. Techet. *Experimental visualization of the near-boundary hydrodynamics about fish-like swimming bodies.* PhD dissertation, Massachusetts Institute of Technology and the Woods Hole Oceanographic Institution, Department of Ocean Engineering, 2001.

[18] P. Tokumaru and P. Dimotakis. Rotary oscillation control of a cylinder wake. *Journal of Fluid Mechanics*, 224:77–90, 1991.

[19] M. Triantafyllou and G. Triantafyllou. An efficient swimming machine. *Scientific American*, 272(3):64–70, 1995.

[20] J. Videler. *Fish Swimming.* Chapman and Hall, London, 1992.

[21] F. M. White. *Fluid Mechanics.* McGraw-Hill, Boston, MA, 1999.

[22] X. Zhang. *I. Surfactant effects on the interaction of a three-dimensional vortex pair with the free surface; II. Turbulent flow over a flexible body undergoing fish-like swimming motion.* PhD dissertation, Massachusetts Institute of Technology, Department of Ocean Engineering, 2000.